High-Efficiency Electrostatic Precipitators

Tsrong-Yi Wen

A dissertation
submitted in partial fulfillment of the
requirements for the degree of

Doctor of Philosophy

University of Washington

2015

Reading Committee:

Alexander Mamishev, Chair

John Kramlich

Igor Novosselov

Program Authorized to Offer Degree:
Department of Mechanical Engineering

University of Washington

Abstract

High-Efficiency Electrostatic Precipitators

Tsrong-Yi Wen

Chair of the Supervisory Committee:
Professor Alexander Mamishev
Department of Electrical Engineering

Indoor air pollution is a source of risk for diseases, such as stroke, ischemic heart disease, respiratory infections, and lung cancer. According to the World Health Organization, nearly 4.3 million people die each year due to exposure to household air pollution. Residential, commercial, and medical facilities use air filters to remove particles from the air stream to maintain indoor air quality. Electrostatic precipitators (ESPs), a common type of air filter, use the corona effect to charge particles, and collect the charged particles using a designed electrostatic field. Most of the components of ESPs are placed along the path of airflow so that there are very few obstacles that obstruct the airflow, making the pressure drop across ESPs low and allowing ESPs to operate in an energy efficient fashion. However, certain collected particles re-enter the environment due to external disturbances, such as strong airflow, vibrations, and spark discharge (sparkover). This act of particle re-entrainment lowers collection efficiency. Commercial ESPs attempt to mitigate particle re-entrainment by adding a fibrous post-filter. However, the implementation of a fibrous filter impedes

airflow, increasing the pressure drop across the ESP. Thus, one of the main design considerations for an ESP is determining the engineering trade-off, where the ESP is capable of capturing the required percentage of particles in the air, yet the pressure drop is not high enough to become economically prohibitive. This dissertation presents two particle-trapping mechanisms that are added to the collecting electrodes of two-stage ESPs to suppress particle re-entrainment without introducing additional pressure drop. The main idea behind particle-trapping mechanisms is to store the collected particles in secured spaces, where disturbances are less likely to cause particle re-entrainment. One promising particle-trapping mechanism involves covering the collecting electrodes with porous foam, allowing particles to attach to the surface inside the pores of the foam, instead of the flat surface of the bare collecting electrode. Another particle-trapping mechanism involves covering the collecting electrodes with perforated guidance plates. Gaps are intentionally left between the guidance plate and the collecting electrode to allow particles to enter through the holes, and remain inside the gaps. Particles collected by either particle-trapping mechanism have a lower chance of returning to the air stream, because there are fewer disturbances inside the pores or gaps than on the flat surfaces of the bare collecting electrodes. The inclusion of either mechanism improves collection efficiency, and therefore, a post-filter is no longer required. Foam-covered ESPs have been tested to have up to 99% collection efficiency. The energy analysis showed that when the fiber-based filters in Loew Hall at the University of Washington were replaced with foam-covered electrostatic precipitators, the operating cost

per airflow reduced by 26.5%. Guidance-plate-covered ESPs have been proven to have up to 22% higher collection efficiency than conventional ESPs that have no particle-trapping mechanism. This dissertation presents and discusses both foam-covered ESPs and guidance-plate-covered ESPs from various perspectives, attempting to move two-stage ESPs a step closer for non-industrial applications.

TABLE OF CONTENTS

LIST OF FIGURES

LIST OF TABLES

ACKNOWLEDGMENTS

I would like to express my deepest gratitude to my academic advisor, Professor Alexander V. Mamishev, for his valuable advice during my researching process, including advising the direction of my research project, providing research funding, and offering teaching opportunities. I would also like to express my appreciation to all committee members, Professor Alberto Aliseda, Professor John Kramlich, Professor Igor Novosselov, and Professor Edmund Seto for their great contributions of time, comments, and input to my research. I would like to specially thank Dr. Igor Krichtafovitch for leading me into the field of air filtration and inspiring me with critical thinking about electrostatic precipitators, and Dr. Hsiu-Che (Joseph) Wang for his invaluable support in my research. Furthermore, I would like to extend my thanks to all members, both current and past, of the Sensors, Energy, and Automation Laboratory (SEAL): Brandon Asheim, Stephen Bailey, Joshua Hutt, Daniel Cong-Huy Luu, Trung Luu, Sep Makhsous, and Tsan-Ting Shen for their support and help during my PhD career. I would like to specially thank Victoria Duan and Aaron Zielinski for their fabulous help in proof-reading works. Of course, I would like to thank all of my friends, wherever they are, especially PTT for his remarkable help in everything I need. Financial support has been provided by the Commercialization Gap Fund from the CoMotion (formerly the Center for

Commercialization) at the University of Washington, the American Public Power Association Demonstration of Energy and Efficiency Developments program, and the Department of Homeland Security. Finally, I would like to thank my family for always supporting me. I could not pursue my dream without their non-stop support and encouragement.

DEDICATION

to my dear family

Chao-Chu Wen

A-Yueh Chen

Shu-Hui Wen

Yi-Chan Wen

Chapter 1
INTRODUCTION

The work presented in this dissertation is motivated by the increasing need for high-efficiency air filters in non-industrial applications. For an air filter, "high-efficiency" is defined when the air filter has high (particle) collection efficiency and low pressure drop. This dissertation presents two two-stage electrostatic precipitators (ESPs) with novel particle-trapping mechanisms added onto the collecting electrodes to suppress particle re-entrainment and improve collection efficiency. These novel ESPs do not require pre- and/or post-filters, such that low pressure drop and high energy efficiency are expected. This dissertation is a study of the designs, assemblies, integrations, theories, numerical modeling, and the experiments of these novel ESPs. The work done in this dissertation is based on publications by the author [1-7].

1.1 Significance of Air Filters in an HVAC System

Figure 1.1 shows a schematic of a typical HVAC system (heating, ventilation, and air conditioning), demonstrating air filters, heating and cooling coils (heat exchangers), and pumps. Pumps bring air into and out of the system, air filters remove particles from the air stream, and heat exchangers condition the air.

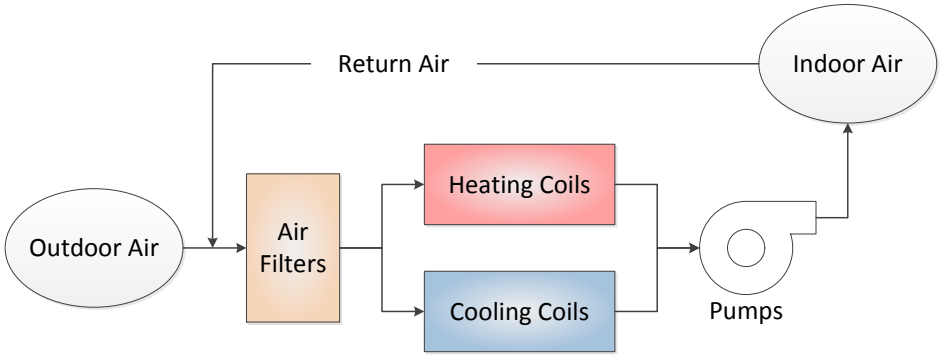

Figure 1.1: Schematic of a typical HVAC system.

From the collection efficiency standpoint, filtering particles out of the air stream to improve air quality has gained considerable attention for two reasons. First, fine pollutant particles (smaller than 2.5 µm in diameter, $PM_{2.5}$) are considered a source of risk for diseases [8-10], such as ischemic stroke, respiratory disease, and cardiovascular disease. Second, clean air protects downstream components in an HVAC system, such as the pumps and the heat exchangers, from soiling. From an energy efficiency standpoint, pumps consume a significant amount of energy, and using low pressure drop (resistance to the airflow) air filters can save an HVAC system a great amount of energy.

A modern high-efficiency air filter requires both high collection efficiency and low pressure drop. The collection efficiency of an air filter depends on several factors [11-23], such as the type and dimension of the filters (e.g., electrostatic stages and fibrous fibers), the properties of the particles (e.g., resistivity and diameter), the environmental conditions (e.g., particle concentration, humidity, and temperature), and the operating conditions (e.g., volumetric airflow rate). On the other hand, the energy consumption of an HVAC system depends

largely on the system pressure drop that is mainly contributed by the air filters. The higher the pressure drop across the air filters, the greater the amount of energy supplied to the pumps.

1.2 Introduction to Air Filters

1.2.1 Fiber-Based Filters

1.2.1.1 Overview

Fiber-based filters are usually made out of a dense mesh of fiberglass. Particles are unable to pass through fiberglass mesh because of three capturing mechanisms: impaction, interception, and diffusion [24], as illustrated in Figure 1.2. The impaction mechanism implies that large particles directly impact the mesh structures and are captured. The interception mechanism implies that large particles that cannot pass through the pores of the mesh structures, and consequently stick to the pores or the mesh structures instead. The diffusion mechanism refers to the Brownian motion, the interactive motions of moving particles and air molecules affect the moving trajectories of ultra-small particles (smaller than 0.1 μm). In other words, such ultra-small particles are captured by chance because the interactive motions between the particles and air molecules increase the probability for the particles to be captured by the mesh structures of the filters. In addition to the capturing mechanisms mentioned above, electret fibers are often used to enhance fibrous filter's collection efficiency. There are electric fields present between the electret fibers when an amount of charge is implanted in the electret fibers. A certain amount of particles can be collected by these electret fibers because

of the induced electrostatic forces.

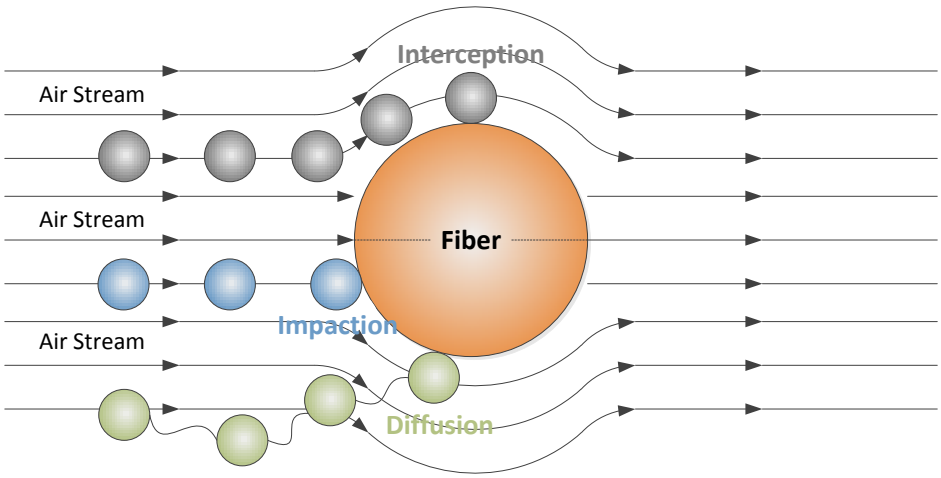

Figure 1.2: Particle capturing mechanisms of fiber-based filters.

The collection efficiency of fiber-based filters depends on several parameters, including the diameter of the fibers, the material of the fibers, mesh density, and filter thickness. Other external factors, such as particle size, particle mass, environment temperature, and the density of accumulated particles on the fibers, also have a considerable influence on the collection efficiency of fiber-based filters.

1.2.1.2 Classification

The American Society of Heating, Refrigerating and Air Conditioning Engineers (ASHRAE) rates the performance of fiber-based filters in terms of the minimum efficiency reporting value (MERV). The MERV has 16 official ratings (1 to 16) and four comparative ratings

(17 to 20), as shown in Table 1.1 [25]. Each rating has different collection efficiencies for three ranges of particle sizes. For residential applications, ASHRAE suggests a filter with a minimum rating of MERV 6 [26]. The American Society of Mechanical Engineers (ASME) requires a high-efficiency particulate air filter (HEPA) to be capable of removing at least 99.97% of dioctyl phthalate (DOP) particles larger than 0.3 µm in diameter [27]. According to the MERV ratings, a MERV 17 filter is equivalent to a HEPA filter.

Fiber-based filters are the most widely used filters because of their simple structures, easy installation, and low cost. However, fiber-based filters are not ideal for high temperature applications, such as coal plants [28, 29], metallurgical plants, and chemical factories [30], where high temperatures may lead to fire hazards and degradation of fiber materials. Fiber-based filters are also unsuitable for highly dusty environments, as these conditions result in frequent maintenance or replacement. One of the most significant concerns of using fiber-based filters in an HVAC system is that the pumps consume large amounts of energy in order to overcome the high pressure drop across the filters. Additionally, the pressure drop across fiber-based filters increases over time because of particle accumulation, causing the energy supplied to the pumps to increase accordingly, sometimes several fold, to maintain a specific airflow rate.

Table 1.1: MERV ratings, where η represents the filtration efficiency in percent [25].

MERV	0.3 µm to 1.0 µm	1.0 µm to 3.0 µm	3.0 µm to 10.0 µm
1	n/a	n/a	$\eta < 20$
2	n/a	n/a	$\eta < 20$
3	n/a	n/a	$\eta < 20$
4	n/a	n/a	$\eta < 20$
5	n/a	n/a	$20 \leq \eta < 35$
6	n/a	n/a	$35 \leq \eta < 50$
7	n/a	n/a	$50 \leq \eta < 70$
8	n/a	n/a	$70 \leq \eta$
9	n/a	$\eta < 20$	$85 \leq \eta$
10	n/a	$50 \leq \eta < 65$	$85 \leq \eta$
11	n/a	$65 \leq \eta < 80$	$85 \leq \eta$
12	n/a	$80 \leq \eta$	$90 \leq \eta$
13	$\eta < 75$	$90 \leq \eta$	$90 \leq \eta$
14	$75 \leq \eta < 85$	$90 \leq \eta$	$90 \leq \eta$
15	$85 \leq \eta < 95$	$90 \leq \eta$	$90 \leq \eta$
16	$95 \leq \eta$	$95 \leq \eta$	$95 \leq \eta$
17	$99.97 \leq \eta$, in 0.3 µm particle size		
18	$99.99 \leq \eta$, in 0.3 µm particle size		
19	$99.999 \leq \eta$, in 0.3 µm particle size		
20	$99.999 \leq \eta$, in 0.1 µm to 0.2 µm particle size		

1.2.2 Electrostatic Precipitators

1.2.2.1 Overview

While the principles of "ionic wind" purification have been known for decades, the commercial use has been mostly limited to industrial-sized ESPs, where the temperature is too high for fiber-based filters. These ESPs are normally used to clean the exhaust from coal [28, 29], metallurgical, and chemical plants [30]. High particle concentration and high pressure drop also make fiber-based filters non-realistic in such industrial applications, or frequent replacements, maintenances, and high energy consumption would be expected.

The total mass collection efficiency of an ESP is high. However, this measure can be misleading when coming to residential and commercial applications. One coarse particle may weigh as much as 100,000 fine particles, whereas fine particles are the primary concern for health issues. Many commercial filters have an ESP stage, augmented by a pre-filter and/or a post-filter, exactly for the reasons that the ESP stage does not remove particles across the desired range with sufficient efficiency.

Figure 1.3 shows a schematic of a traditional two-stage ESP. A pump draws air and particles into the system. Certain particles are filtered out by a pre-filter. The remaining particles are charged when they pass by the charger. As these charged particles pass through a set of electrode plates (collector), strong electrostatic forces drive the charged particles to move toward and settle on the collecting electrodes. A post-filter, if needed, captures the particles that are not captured by the collecting electrodes. As a result, most of particles in

the air stream are removed.

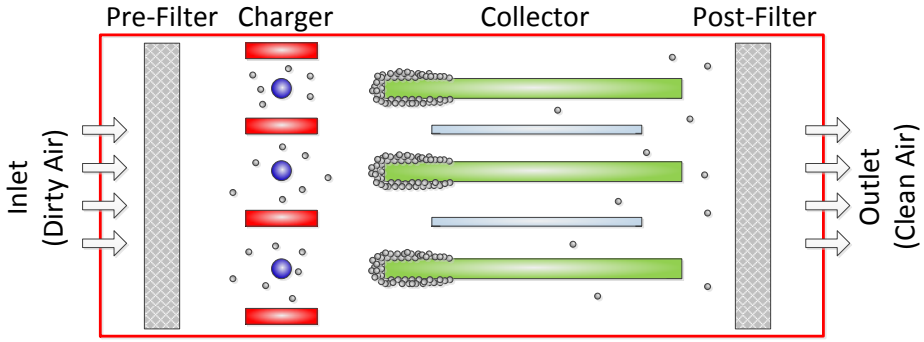

Figure 1.3: Schematic of a traditional two-stage ESP.

In recent years, the following technological developments have made "ionic wind cleaning" technology more competitive in the field of air filtration. First, the new collecting and repelling electrode geometries dramatically increase the resulting air cleanliness [15, 31-33]. At the same airflow rate, the performance of ESPs with new electrode geometries exceeds that of most HEPA filters, allowing for significant reductions in the size of the pumps. Substantial electricity savings can be made due to this change [5, 34, 35]. Second, innovative, high-voltage electronics with microprocessor control and smart control allow for operation at high collection efficiencies despite environmental changes [35-37]. Third, ozone generation can be reduced to background levels due to the use of new materials for the corona electrodes [14, 38-40].

1.2.2.2 Classification

Although ESPs have been used for decades, it is not easy to precisely classify ESPs into a few specific categories. This dissertation groups ESPs by configuration, number of stages, and type of collecting electrode.

Wire-Plate/Wire-Cylinder ESPs

From both theoretical and experimental points of view, wire-plate ESPs are the best understood ESPs. Wire-plate ESPs are composed of corona electrodes (wire), and collecting electrodes (plate). A wire-plate ESP has at least one corona wire in the airflow channel, or several corona wires in a row along the airflow direction. Charged particles are moved to the collecting electrodes by the electric field that exists between the corona wires and collecting electrodes, and settle on the collecting electrodes. Due to the simple geometry and low resistance to airflow, wire-plate ESPs are well suited for applications involving large amounts of airflow.

The "wire" of a wire-cylinder ESP refers to the corona electrodes, and the walls of the cylinder are the collecting electrodes. Wire-cylinder ESPs are less used, because their geometries are not as flexible as wire-plate ESPs, even though wire-cylinder ESPs are axially symmetric, providing researchers an easier way to derive and verify theoretical models.

Single-Stage/Two-Stage ESPs

Figure 1.4 shows the schematic of typical ESPs. ESPs that are known as single-stage ESPs charge and collect particles at the same time. Although single-stage ESPs are more successful in suppressing particle re-entrainment [12], single-stage ESPs may have issues of

back corona [41], when compared to two-stage ESPs.

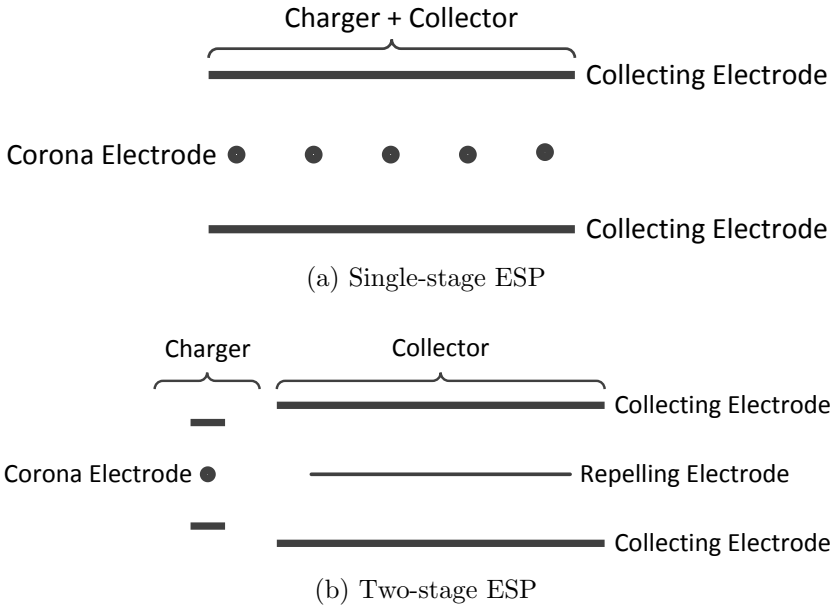

(a) Single-stage ESP

(b) Two-stage ESP

Figure 1.4: Schematic of typical ESPs.

Two-stage ESPs charge and collect particles in separate sections. Particles are charged when they pass the charger and are collected by the collector, which has both collecting and repelling electrodes. The repelling electrodes are placed between two adjacent collecting electrodes. The repelling electrodes are energized with high voltage and the collecting electrodes are grounded. The electric field strength between the repelling and collecting electrodes can be much stronger than that between the corona wires and the collecting electrodes in single-stage ESPs. This occurs because the surface area of the repelling electrodes is much larger than that of the corona wires. Two-stage ESPs handle smaller amounts of airflow than single-stage ESPs, but are more suitable for low resistivity (high conductivity)

particles, mists, and adhesive particles [12, 42, 43].

Wet/Dry ESPs

The resistivity of particles dramatically affects the performance of ESPs. Dry ESPs are able to deal with particles that have normal resistivity, whereas wet ESPs are capable of handling particles that have extremely high or low resistivity [12]. Wet ESPs remove moist particles, such as nitro compounds and sulfur compounds, by using a water film on the collecting electrodes. Because the adhesion of particle-water (wet ESPs) is stronger than that of particle-metal (dry ESPs), wet ESPs have fewer particle re-entrainment complications than dry ESPs [44-47].

1.3 Advantages and Disadvantages of Electrostatic Precipitators

1.3.1 Advantages of Electrostatic Precipitators

Energy Savings

The energy consumption of a filtration system depends greatly on the pressure drop of the filters. The higher the pressure drop across the filters, the higher the energy consumed by the system pumps. Figure 1.5 shows the schematic of a filtration system using a fiber-based filter and an electrostatic precipitator. A two-stage electrostatic precipitator consists of corona electrodes, repelling electrodes, and collecting electrodes, whereas a fiber-based filter consists of a dense fabric mesh. The electrodes of an electrostatic precipitator are placed along the direction of the airflow, while a fiber-based filter is placed directly in the path of the airflow. Therefore, the pressure drop across electrostatic precipitators is lower

than that across fiber-based filters. Additionally, the particles accumulating on the collecting electrodes of ESPs do not increase the pressure drop over time, because the surface areas of the collected particles are much smaller than the cross-sectional areas of the airflow channel.

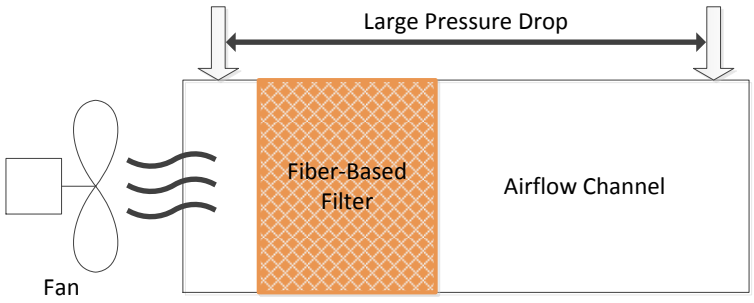

(a) With fiber-based filter

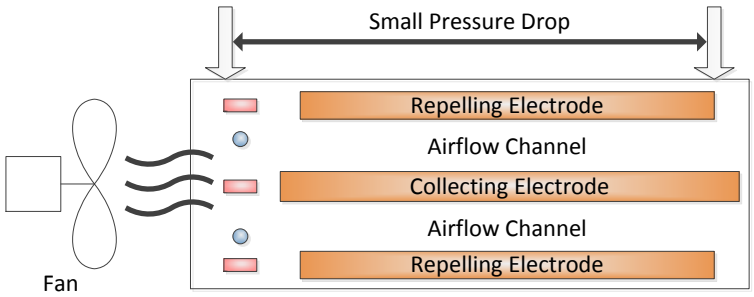

(b) With electrostatic precipitator

Figure 1.5: Schematic of filtration systems using a fiber-based filter and an electrostatic precipitator. The pressure drop across fiber-based filters is larger than that across electrostatic precipitators.

Low Acoustic Signatures

The acoustic noise of a filtration system comes mainly from the pump blades sweeping the air, leading to vortex shedding, the process of air separating from the blade surface and trailing edge of the pump blades [48]. Vibrations of the pump motor and the air turbulence

in the ducts are also responsible for acoustic problems. Because an electrostatic precipitator has a lower pressure drop than a fiber-based filter, an electrostatic-based filtration system is able to achieve the same airflow rate as a fiber-based filtration system with smaller pumps or lower rotational speeds. In other words, at the same airflow rate, an electrostatic-based filtration system operates more silently than a fiber-based filtration system.

High Scalability

ESPs can be built in any scale without sacrificing efficiency [49]. The dimensions of the plate and wire electrodes of ESPs are dependent on the application. Longer collecting electrodes capture particles more effectively. Alternatively, ESPs can be scaled down to the size of portable air cleaners. The ESPs presented in this dissertation are lab-scale prototypes that are smaller in size than an Xbox console, but still retain high ratings of collection efficiency and low pressure drop.

High Temperature Application

Because ESPs are highly scalable and are comprised of metal or non-flammable materials, they are suitable for industrial and high temperature applications. Figure 1.6 shows an example of ESPs that are used in a power plant, where the height of a single collecting electrode is over 16 meters.

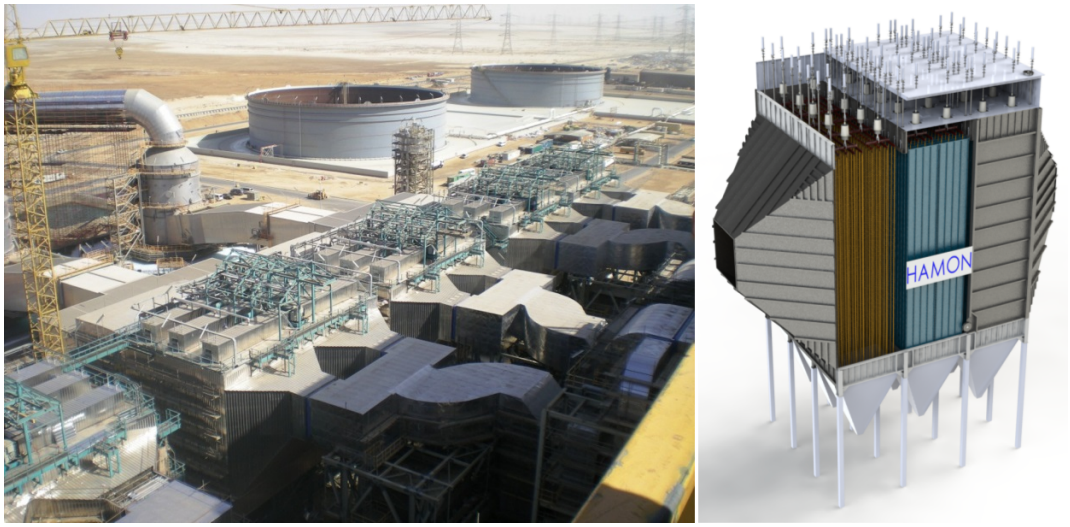

Figure 1.6: The application of ESPs in a power plant [50-52].

1.3.2 Disadvantages of Electrostatic Precipitators

High Voltage Operation

To initiate corona discharge and prevent spark discharge, the operating voltage of an ESP should lie between the corona onset voltage and the air breakdown voltage [53], which is usually in the range of thousands of volts. The electric current passing through the corona electrodes in a large-scale ESP could be lethal. To meet the safety standards, sophisticated high voltage electrical design precautions, such as the isolation of high voltage and high electric field shielding, for an ESP is extremely important and required.

Electrode Degradation

Erosion, corrosion, and contaminate adhesion usually occur within the plasma or ionization region because of the depositions of chemicals or pollutants on the corona electrodes. Reactions between the chemical substances in both the air and the corona electrodes degrade

the performance of the ionization processes [54-56], lowering the reliability and longevity of the system. Additionally, the metal plate electrodes (repelling and collecting electrodes) suffer oxidation over time due to the exposure to air. This can lead to poor particle-metal adhesion as well as the degradation of the electric field strength in the collector. The mechanisms of particle collection and the electrical characteristics of the system can be altered due to such degradations, eventually lowering the collection efficiency.

Ozone Emission

One potential environmental and health impact of applying ESPs in an HVAC system is the emission of ozone that is a byproduct of corona discharge. At high concentrations, ozone is irritable and damaging [57-59]. Ozone is one of the six principal pollutants of the national ambient air quality standards (NAAQS) set by the Environmental Protection Agency (EPA). Currently the EPA standard has set eight hours of ozone concentration as 75 ppb (parts per billion by volume). According to the staff technical report of the Air Resources Board (ARB) of the California Environmental Protection Agency, commercially available ESPs have low ozone emission rates [60], and do not exceed the California health-based standard of 70 ppb. The U.S. Food and Drug Administration (FDA), the Underwriters Laboratories (UL), and the Centers for Disease (CDC) have different regulations regarding ozone emissions. Table 1.2 summarizes the regulations of ozone emission set by different agencies.

Table 1.2: Regulations of ozone emission.

Organization	Concentration (ppb)	Method/Comment
EPA	75 [61]	Annual fourth-highest daily maximum 8 hours concentration, averaged over 3 years
ARB	70 [62]	8 hours average
FDA	50 [63]	
UL	50 [52]	At two inches from the face of the device after 24 hours of operation
CDC	100 [64]	

1.4 Engineering and Scientific Challenges

The research work presented in this dissertation addresses several engineering and scientific challenges, which can be discussed from various perspectives, as detailed below.

1.4.1 Improvement of Collection Efficiency

The collection efficiency of an ESP depends on numerous factors, such as the physical dimensions, particle charging, operating condition, particle properties, and collection mechanism, as addressed in the following list.

Physical dimensions. The electric field between repelling and collecting electrodes causes particles move toward and reside on the collecting electrodes. Shorter distances between the repelling and collecting electrodes (i.e., narrower airflow channel) results in higher electric field strengths and higher particle migration velocities, allowing collecting electrodes

to capture particles with greater ease. Longer collecting electrodes also increase collection efficiency because particles' resident time in the collector is longer.

Particle charging. The amount of charges a particle carries is critical to the collection efficiency of an ESP. The more charges carried by a particle, the higher the collection efficiency will be. The efficiency of corona discharge depends on the diameter of the corona wire, applied corona voltage, voltage polarity, the material of the corona electrode, and the properties of the particle [65, 66]. The charge limit of a particle further depends on the particle diameter, the surface field strength required for spontaneous emission of electrons, and the electrostatic constant of proportionality [67].

Operating condition. The corona and repelling voltages affect collection efficiency directly. Higher corona voltage results in a higher capability of corona discharge. Higher repelling voltages result in higher electric field strength in the collector. Free airflow velocity, generated by pumps, is also significant in determining collection efficiency. Higher free airflow velocity could blow particles out of the collector, while lower free airflow velocity could increase the chance of spark discharge in the charger [3].

Particle properties. The resistivity of particles determines how a particle is charged. Highly resistive particles cannot be easily charged, while conductive particles easily subject to fast discharging. For a highly resistive dust, the electrical breakdown of the dust layer could occur at very low current densities, resulting in a condition called back corona or reverse ionization [41]. On the other hand, smaller particles carry smaller amounts of charges than larger particles. The more the charge a particle carries, the higher the collection ef-

ficiency. Besides, some sticky particles could attach to corona electrodes, contaminating and/or lowering the durability of the corona electrodes.

Collection mechanism. ESPs capture particles on the collecting electrodes due to a combination of mechanical forces, electrostatic forces, and molecular forces. Collected particles have the possibility of dislodging from the collecting electrodes and returning to the environment (particle re-entrainment) due to disturbances such as strong airflow, vibrations, insufficient charge, and low adhesions to the collecting electrodes [12, 68-72]. These disturbances could lower the overall collection efficiency by up to 30% [73-75]. One way to reduce the chance of particle re-entrainment is to trap particles in secured spaces. Such a particle-trapping mechanism should be simple, economical, easy to install, easy to clean, and able to accommodate large amounts of particles.

1.4.2 Reduction of Energy Consumption

The energy consumption of a filtration system is in direct association with the system pressure drop that results from the frictional loss between the air and the contact walls, and is mainly contributed by the filters. The higher the pressure drop across the filters, the higher the energy supplied to the pumps, and the higher the energy cost.

Many commercially available ESPs use pre- and/or post-filters to capture particles that are unable to be collected by the ESP stage. Such filters, usually fibrous, also increase the pressure drop. An ideal ESP should have a high rate of collection efficiency without any fibrous filters. Any add-on mechanisms or geometry adjustments that are used to improve

the collection efficiency should not obviously increase the pressure drop. The collection efficiency and pressure drop must be skillfully balanced during the design stage.

1.4.3 Non-Industrial Applications

ESPs are suitable for high temperature applications and highly dusty environments, because these ESPs are composed mainly of metallic materials that are non-flammable and are not consumed during operation. To date, there are few successful applications of ESPs in residential areas and commercial buildings because of unsatisfactory energy efficiencies and collection efficiencies across the desired range of particle sizes. Other concerns, such as ozone emissions, reliability, durability, and high voltage operation also make ESPs unpopular in non-industrial applications.

Although ozone is a byproduct of corona discharge processes, well-designed and maintained ESPs do not generate ozone in amounts sufficient to be considered a hazard [76]. The amount of ozone emissions is determined by several factors, including temperature, humidity, particle properties, and corona electrode properties (e.g., material, dimension, and geometry) [14, 38, 77-79]. Catalysts are typically used to neutralize ozone emissions [80, 81]. High temperatures can also aid in ozone reduction, but require a sophisticated electrode design [39, 82, 83].

Reliability and durability are key issues that limit the use of ESPs in various applications. Corona electrode degradation, including chemical erosions and contaminated deposits on the electrode surface, may lead to non-uniform corona discharge and device failure [84].

Substances that cause erosions and contaminations arise from the air stream, or the decompositions of the ionization processes [51].

High voltage safety is also a key design consideration, and is especially critical in the case of non-industrial applications. High voltage and spark discharge are considered dangerous and may cause a psychological fear when operating the ESP, which might lead to other serious mistakes and hazards.

1.5 Scope of the Dissertation

Figure 1.7 depicts the scope of this dissertation. This dissertation focuses on the development of high-efficiency ESPs that have high collection efficiency and low pressure drop. The primary applications of these newly developed ESPs are non-industrial applications, such as residential areas, commercial buildings, and medical facilities.

Theory. The fundamentals behind ESPs are particle charging and particle kinetics. The theory of particle charging determines how many charges a particle carries, while particle kinetics studies how a charged particle moves along the flow field and the electric field in an ESP. Based on particle charging and particle kinetics, this dissertation discusses the Deutsch-Anderson equation [85], which provides the basis of collection efficiency by solving an ordinary differential equation with proper assumptions and boundary conditions. Since the Deutsch-Anderson equation assumes that the turbulent mixing diffusion is dominant and the particle concentration profile is uniform in the core flow [86], the predicted collection efficiencies are underestimated. Two additional theoretical equations of collection efficiency

are also discussed, including Cooperman's [87] and Zhang's [88] work. Cooperman's work encompasses particle diffusion in the direction transverse to the free airflow, while Zhang's work involves solving convective diffusion equation with zero flux boundary conditions.

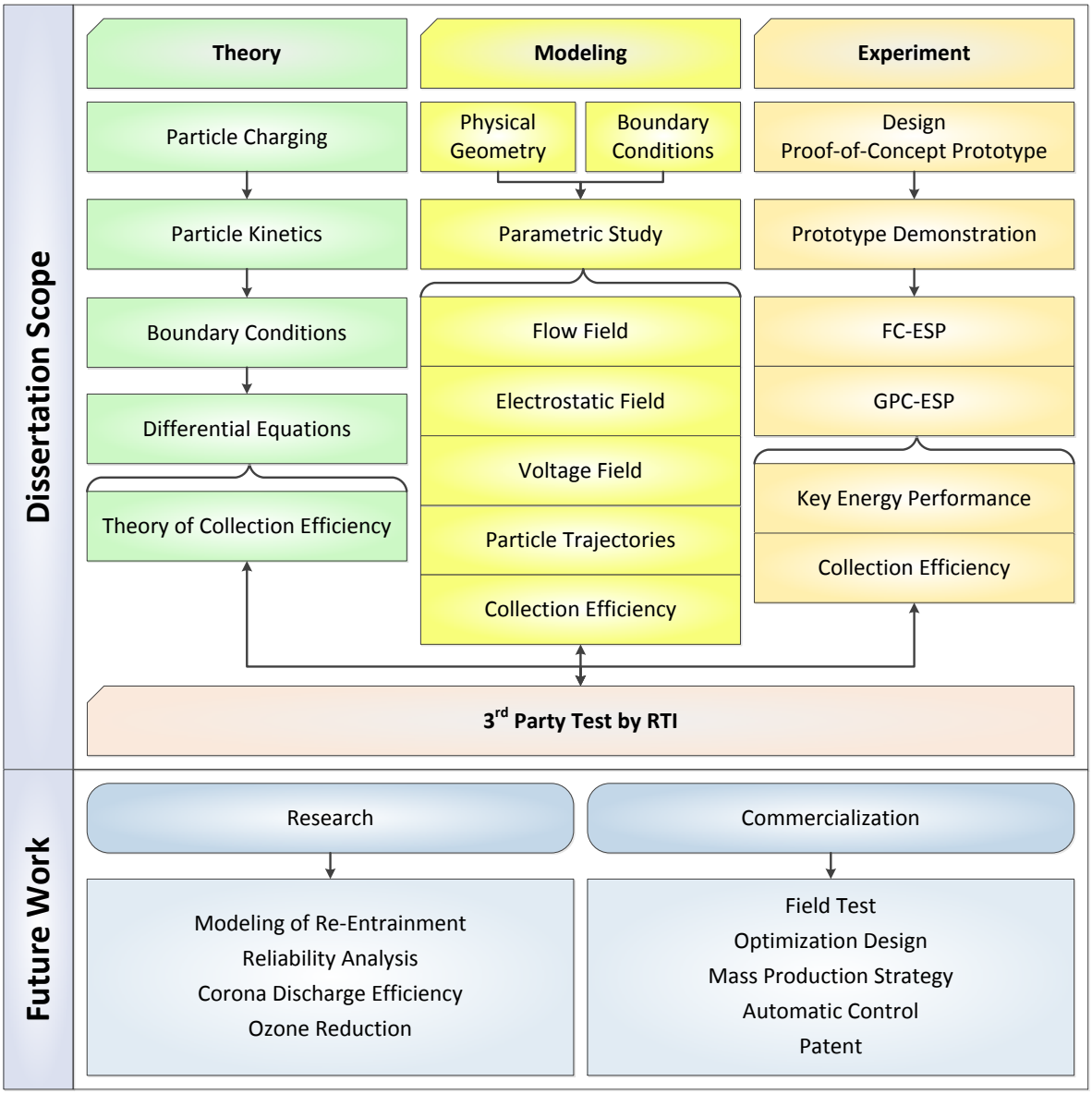

Figure 1.7: Scope of the dissertation and future work.

Modeling. The 2D numerical model is carried out by COMSOL Multiphysics, coupling the interactions between fluid mechanics, electrostatics, particle charging, and particle transport. The parametric studies are performed in accordance to the parameters set in the experiments. The results, covering flow and electric characteristics, are thoroughly discussed. This dissertation also presents particle trajectories and determines the corresponding collection efficiencies. The collection efficiencies measured from the experiments are compared with the numerical results. Furthermore, this dissertation demonstrates particle re-entrainment trajectories and re-entrainment rates by performing a set of simulations with simplified boundary conditions.

Experiment. Two novel particle-trapping mechanisms of ESPs are presented in this dissertation: foam-covered ESPs (FC-ESPs) and guidance-plate-covered ESPs (GPC-ESPs). The main idea behind the particle-trapping mechanisms is to store collected particles in secured spaces so that they have lower chances of re-entering the environment in the case of external disturbances. FC-ESPs use foam, which is porous and has a weak electrical conductivity, to attach to the collecting electrodes. Particles attach to the surface inside the pores of the foam instead of the flat surface of the bare collecting electrode. The weak electrical conductivity of the foam prevents significant degradation of the electric field strength in the collector. Additionally, the edges of the repelling electrodes are covered by the foam, such that the chance of spark discharge between the electrodes is minimized, and the conductive dust is kept from fast discharging. For GPC-ESPs, the collecting electrodes are covered by the perforated guidance plates, and gaps are intentionally left between the guidance plates

and the collecting electrodes using insulated spacers. Particles can go through the holes of the guidance plates and be stored in the gaps. Additionally, the gaps are capable of accommodating large amounts of particles. Because no consumable materials are used, GPC-ESPs are ideal for highly dusty applications, such as tunnels, railroads, and power plants.

The baseline prototypes of the FC-ESPs and GPC-ESPs are hand-made, using commercial off-the-shelf (COTS) materials and parts. Rigorous tests are conducted in-house and provide the base proof that the FC-ESPs and GPC-ESPs have high ratings of collection efficiencies without any pre- and/or post-filters. Parametric studies are performed to show the interactions between the collection efficiencies, key energy performance, and key design parameters of interest, including free airflow velocity, corona voltage, repelling voltage, and some geometric factors.

Third Party Test. Research Triangle Institute (RTI) International, a nonprofit third-party organization, conducts some tests for the FC-ESP. The test methodology follows ASHRAE 52.2 standard. The tested particle is dry and solid-phase potassium chloride (KCl), and each particle load is five grams. The tests are conducted to measure the collection efficiencies for different particle sizes, ranging from 0.3 µm to 10 µm. In addition to the collection efficiency, the pressure drop (as a function of airflow velocities) and ozone concentration are also measured and reported.

1.6 Contributions of the Dissertation

This dissertation makes three major contributions that attempt to move two-stage ESPs a step forward towards non-industrial applications.

First, this dissertation presents the first demonstration of foam-covered ESPs in the world. For FC-ESPs, porous foam is used to cover the collecting electrodes, storing particles inside the pores of foam and lowering their chances of re-entering the environment. FC-ESPs have high ratings of collection efficiencies, up to 99%, without the use of pre- and/or post-filters. Thus, FC-ESPs have a low pressure drop. Using FC-ESPs in an air filtration system does not significantly increase resistance to the airflow over time, and keeps a low pressure drop across the system. This dissertation also provides a comprehensive procedure to evaluate energy savings for a filtration system. An example, the filtration system in Loew Hall at the University of Washington, is demonstrated and the results show that the energy cost per unit airflow can be reduced by 26.5% when the fiber-based filters are replaced with the foam-covered electrostatic precipitators.

Second, this dissertation presents the first demonstration of guidance-plate-covered ESPs in the world. For GPC-ESPs, the collecting electrodes are covered by the perforated guidance plates, but gaps are intentionally left between the guidance plates and the collecting electrodes using spacers. The results show that GPC-ESPs have up to 22% higher collection efficiency than traditional ESPs that have bare collecting electrodes. Frequent maintenance and replacement is unnecessary because GPC-ESPs are completely comprised of metal parts.

Further, GPC-ESPs are able to store large amounts of particles inside the gaps between the guidance plates and the collecting electrodes. This feature makes GPC-ESPs highly suitable for heavy-duty and high temperature applications, such tunnels, railroads, and power plants.

Third, this dissertation demonstrates the energy performance of electrostatic precipitators using "key energy performance". For non-industrial applications, evaluating the performance of air filters by looking only at collection efficiency or pressure drop is misleading because these two factors are not necessarily dependent to each other. Using key energy performance to assess air filter performance is more ideal because key energy performance represents the collection efficiency per pressure drop. This dissertation compares the key energy performance of the fiber-based filters and electrostatic precipitators, and also shows how the parameters of interest affect the key energy performance of electrostatic precipitators.

1.7 Outline of the Dissertation

This dissertation is broken roughly into four parts.

Chapter 1 presents an introduction to air filters, including electrostatic precipitators and fiber-based filters. The advantages and disadvantages of using ESPs are also discussed. Scientific challenges, the scope of the dissertation, and the contributions of the dissertation are included in this chapter as well.

Chapter 2 reviews the fundamentals behind ESPs, including the particle charging mechanisms, the kinetics of particles, and the theory of collection efficiency. The history of electrohydrodynamics and the emerging applications of electrohydrodynamics, and the principles

of electrohydrodynamics are covered.

Chapter 3 presents foam-covered ESP in detail, covering the working concepts, the prototype demonstrations, the theoretical predictions of collection efficiencies, and the experiments of collection efficiencies and key energy performance. This chapter also discusses the results from the third party in various perspectives, including collection efficiency, pressure drop, and ozone emission. This chapter also demonstrates an example of energy savings in a real-life HVAC system when fiber-based filters are replaced with foam-covered electrostatic precipitators.

Chapter 4 presents guidance-plate-covered ESP in detail, covering the working concepts, the prototype demonstrations, the numerical modeling, and the experiments of collection efficiencies. Additionally, parametric studies of how the parameters of interest affect key energy performance are presented in this chapter.

Chapter 5 is the conclusions and future work. A table that thoroughly compares four air filters discussed through this dissertation from various standpoints is provided at the beginning of this chapter. This chapter also addresses several topics of future work from both research and commercialization points of view.

Chapter 2
REVIEWS OF FUNDAMENTAL CONCEPTS

This chapter discusses concepts on particle charging and particle kinetics that are helpful in fundamentally understanding the principles behind ESPs. A classic equation of collection efficiency, the Deutsch-Anderson equation, is discussed in detail. This chapter also presents the state of the art for ESPs, especially focusing on the innovations of the capturing mechanism on the collecting electrodes. Further, this chapter goes through electrohydrodynamics (EHD), covering history, EHD-based applications, and governing equations.

2.1 Fundamentals Behind Electrostatic Precipitators

2.1.1 Particle Charging

The fundamental process of an ESP is particle charging. Figure 2.1 shows the level of charges that are contributed by different charging mechanisms in terms of particle sizes [41].

Particles are charged by gaining additional ions from the collisions with other ions or charged particles. This usually refers to field charging, which is the dominant mechanism for particles larger than 0.5 μm (radius). For ultra-fine particles, smaller than 0.2 μm (radius), diffusion charging becomes important, which results from ionic collisions with the particles brought about by the random thermal motion of the ions. If these ions are retained by the

dust particles, the particles become electrically charged [41]. The experimental results had shown that the total particle charges are sufficiently reliable by adding field charging rate and diffusion charging rate [68, 89-91].

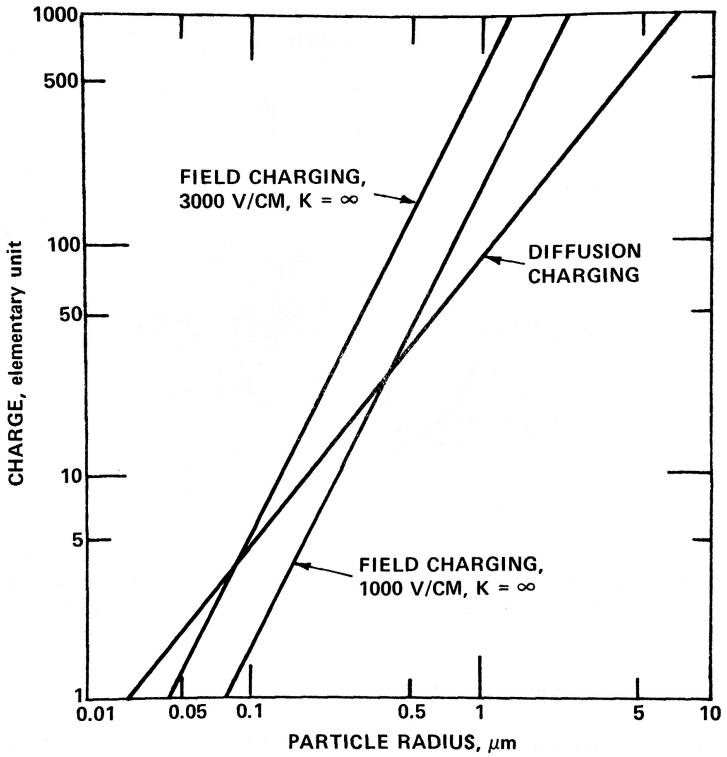

Figure 2.1: The contribution of field charging and diffusion charging to a particle [41].

2.1.1.1 Field Charging

The electric field near a charged particle results from two components, the electric field applied in the charger and the charges on the particle. When the charges continuously accumulate on the particle, the electric field intensity close to the particle also grows. Once

this electric field grows to a certain level, it begins repelling incoming charges. At this point, the amount of gained charges in a particle is saturated. If assumptions, such as spherical shape of the particles and the electric field of particles is independent to each other, are made, the rate of field charging can be expressed by [89],

$$\frac{dq_f}{dt} = \pi b N_0 d_p^2 E_{cr} G \left(1 - \frac{qe}{d_p^2 E_{cr} G}\right)^2 \tag{2.1}$$

$$G = 1 + 2\frac{\varepsilon_p - 1}{\varepsilon_p + 2} \tag{2.2}$$

where q_f is field charging as a function of time t, b is ion mobility, N_0 is ion concentration, d_p is particle diameter, E_{cr} is the electric field strength in the charger, e is elementary charge, and ε_p is the relative permittivity (dielectric constant) of particles.

2.1.1.2 Diffusion Charging

The thermal motions of ions obey the laws of kinetic theory, which causes ions to diffuse through the air and collide with particles. These ions adhere to the particles because of the attractive electrical-image forces. Diffusion charging hence provides a particle charging mechanism that does not depend on an externally applied electric field [49]. The diffusion charging rate can be presented as [89],

$$\frac{dq_d}{dt} = \pi v_{rms} N_0 d_p^2 exp\left(\frac{-qe^2}{d_p KT}\right) \tag{2.3}$$

where q_d is diffusion charging as a function of time, v_{rms} is the root-mean-square thermal velocity of ions, K is the Boltzmann constant, and T is temperature.

2.1.2 Particle Kinetics

According to the Newton's law, for a single charged particle in an ESP, the vector sum of the electrostatic force and drag force is the inertial force. The gravitational force is negligible here because its magnitude is relatively small when compared to others.

$$m_p \frac{d\mathbf{U_p}}{dt} = \frac{3\pi\mu d_p}{C_c}(\mathbf{U} - \mathbf{U_p}) + q_p\mathbf{E} \tag{2.4}$$

where m_p is particle mass ($\pi d_p^3 \rho_p/6$), ρ_p is particle density, $\mathbf{U}$ is the velocity field of fluid, $\mathbf{U_p}$ is the velocity field of particle, C_c is the Cunningham slip correction factor, and q_p is total particle charge. The first term of the right-hand side in (2.4) represents the drag force, whereas the second term represents the electrostatic force.

Note that for particle smaller than one μm, the Cunningham correction factor (also known as slip factor) should be taken into account for migration velocity, because the drag force of such small particles is reduced. The Cunningham correction factor is a function of mean free path of gas molecules, as shown in (2.5) [49].

$$C_c = 1 + \frac{c\overline{\lambda}}{r_p} \tag{2.5}$$

where c is a constant, $\overline{\lambda}$ is the mean free path of gas molecules, and r_p is particle radius. At

normal temperature and pressure, c is 0.86 and $\overline{\lambda}$ is 0.1 µm [49].

To rewrite (2.4) in a dimensionless form, a characteristic fluid velocity U_c, a characteristic length L_c, a characteristic particle charge q_c, and a characteristic electric field strength E_c are introduced, and together they yield,

$$t^* = tU_c/L_c \tag{2.6}$$

$$\mathbf{U}^* = \mathbf{U}/U_c \tag{2.7}$$

$$\mathbf{U}_\mathbf{p}^* = \mathbf{U}_\mathbf{p}/U_c \tag{2.8}$$

$$q_p^* = q_p/q_c \tag{2.9}$$

$$\mathbf{E}^* = \mathbf{E}/E_c \tag{2.10}$$

Equation (2.11) shows the dimensionless form of (2.4), where the superscript * denotes the dimensionless variables.

$$\frac{d\mathbf{U_p}^*}{dt^*} = \frac{1}{Stk}\left(\mathbf{U}^* - \mathbf{U_p}^*\right) + \frac{Es}{Stk} q_p{}^* \mathbf{E}^* \tag{2.11}$$

$$Stk = \frac{C_c {d_p}^2 \rho_p U_c}{18 \mu L_c} \tag{2.12}$$

$$Es = \frac{C_c q_c E_c}{3 \pi \mu d_p U_c} \tag{2.13}$$

where Stk is the Stoke number and Es is the electrostatic number. The Stoke number is the ratio of inertia force to viscous drag force, and the electrostatic number is the ratio of electrostatic force to viscous drag force. Note that the Stoke number is proportional to the characteristic fluid velocity and square of particle diameter, and the electrostatic number is proportional to the characteristic electric field strength in the collector, but is inversely proportional to the particle diameter and the characteristic fluid velocity.

2.1.3 Theory of Collection Efficiency

2.1.3.1 Particle Migration Velocity

Particle migration velocity is important in theoretically deriving the collection efficiency of an ESP. For a two-stage ESP, the particle migration velocity is defined as the particle velocity along the direction of the electric field in the collector. Figure 2.2 is a free body diagram of a charged particle suspending in air stream in a two-stage ESP, while (2.14) shows the simplified equation, from (2.4), for only the electric field direction.

$$m_p \frac{dw}{dt} = -\frac{6 \pi r_p \mu}{C_c} w + q_p E \tag{2.14}$$

where w is particle migration velocity, r_p is particle radius, and E is the electric field strength in the charger.

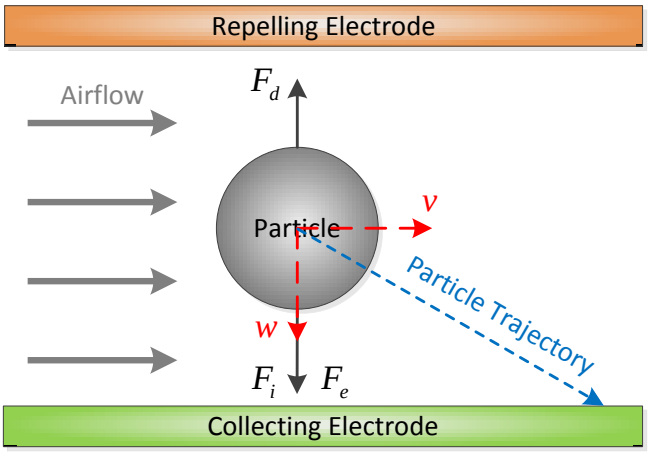

Figure 2.2: A model of a charged particle in a two-stage ESP. The particle subjects to the electrostatic force, the drag force, and the inertial force. The gravitational force is neglected because it is small.

Equation (2.14) is a first order linear differential equation, the analytic solution is shown in (2.15).

$$w = \frac{q_p E C_c}{6\pi r_p \mu}\left[1 - exp\left(-\frac{6\pi r_p \mu t}{C_c m_p}\right)\right] \tag{2.15}$$

The exponential term shown in (2.15) is usually neglected because particles are light-weight and typically have short acceleration times. Thus, the particle migration velocity can be simplified.

$$w = \frac{q_p E C_c}{6\pi r_p \mu} \tag{2.16}$$

2.1.3.2 Deutsch-Anderson Equation

In 1919, Evald Anderson experimentally developed an equation of collection efficiency, and later in 1922 Welther Deutsch theoretically derived the equation of collection efficiency [85]. Before introducing the Deutsch-Anderson equation, a few assumptions should be clarified. First, the particles are fully charged. Second, free airflow velocity does not affect particle migration velocity. Third, particles are distributed uniformly in any cross-section. Fourth, particles always move at electrical terminal velocity. Fifth, there are no particle re-entrainment and back corona. Sixth, the electric field is uniform throughout the collector.

Most of the airflow in an ESP is turbulent, where particle migration velocity is much smaller than free airflow velocity. However, within the airflow boundary layer, the airflow is laminar and the resultant velocity of a particle is the vector sum of free airflow velocity and particle migration velocity. Assuming all particles within the boundary layer are collected in a time interval, Δt. The air stream also moves forward in a distance, ΔL, as shown in Figure 2.3.

$$\Delta\delta = w\Delta t \tag{2.17}$$

$$\Delta L = v\Delta t \tag{2.18}$$

where $\Delta\delta$ is the thickness of boundary layer (in a specific time interval), w is particle migration velocity, and v is free airflow velocity.

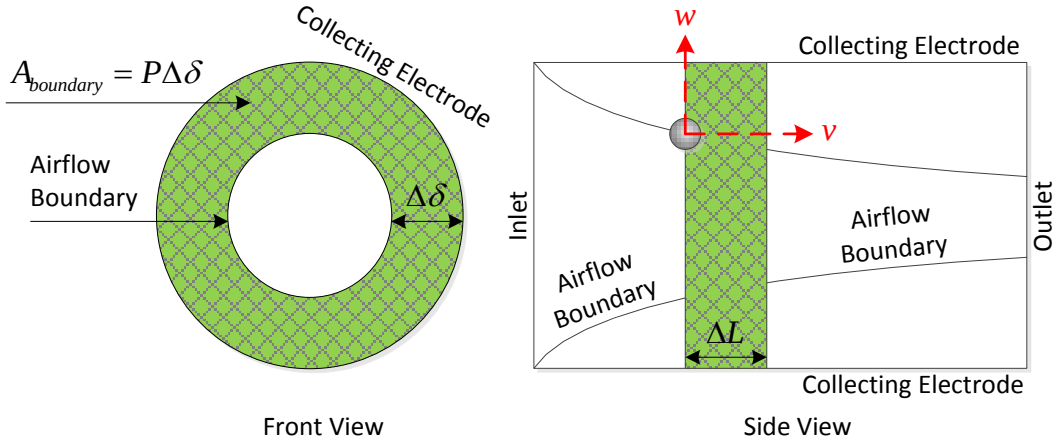

Figure 2.3: A model of particles within airflow boundary layer.

The ratio of the concentration of removed particles to the concentration of total particles in the air can be expressed by the ratio of the cross-sectional area of boundary layer to the cross-sectional area of airflow channel.

$$\frac{\Delta C}{C} = \frac{A_{boundary}}{A_{channel}} = \frac{P\Delta\delta}{A_{channel}} = -\frac{Pw\Delta t}{A_{channel}} = -\frac{Pw\Delta L}{A_{channel}v} = -\frac{w\Delta A_c}{A_{channel}v} \tag{2.19}$$

where ΔC is the concentration of removed particle, C is particle concentration, $A_{channel}$ is the cross sectional area of airflow channel, $A_{boundary}$ is the cross sectional area of airflow boundary layer, P is the circumference of airflow channel, and ΔA_c is the increment of collecting area. Rewriting and rearranging (2.19) yields,

$$\frac{1}{C}dC = -\frac{w}{Q}dA_c \tag{2.20}$$

where $Q = Av$ is volumetric airflow rate. Integrating (2.20) from inlet to outlet results in the particle concentration at outlet, C_{out},

$$C_{out} = C_{in}exp\left(-\frac{wA_c}{Q}\right) \tag{2.21}$$

where C_{in} is particle concentration at inlet and A_c is the surface area of collecting electrode. The collection efficiency, $\eta_{deutsch}$, can then be expressed by,

$$\eta_{deutsch} = \frac{C_{in} - C_{out}}{C_{in}} = 1 - exp\left(-\frac{wA_c}{Q}\right) \tag{2.22}$$

Equation (2.22) is the Deutsch equation, or the Deutsch-Anderson equation. The collection efficiency is exponentially saturated with respect to the particle migration velocity, the area of the collecting electrode, and the volumetric airflow rate. As the particle migration velocity and the area of the collecting electrode increases, the collection efficiency increases accordingly. The collection efficiency decreases when the free airflow velocity increases. Because the equation of particle migration velocity shown in (2.16) varies with particle size, the Deutsch-Anderson equation works only when the particle size is given.

2.2 State of the Art of Electrostatic Precipitators

There are many ESPs that have been proposed to improve the collection efficiency either for specific particles or for general improvement. As this dissertation focuses on the novelty of the collecting electrodes, several literatures are discussed in this section regarding the transformation and optimization of the collecting electrode to improve collection efficiency.

Bologa *et al.* [92, 93] proposed a novel wet ESP that uses tube bundles as collecting electrodes, as shown in Figure 2.4. A liquid film, formed by sedimentation of charged droplets on the tube surface, is used to wash the collected particles away. For fine oil mists and fly ash, the fractional collection efficiency is higher than 98% for particles larger than 1.0 µm and 95% to 98% for particles between 0.3 µm and 1.0 µm.

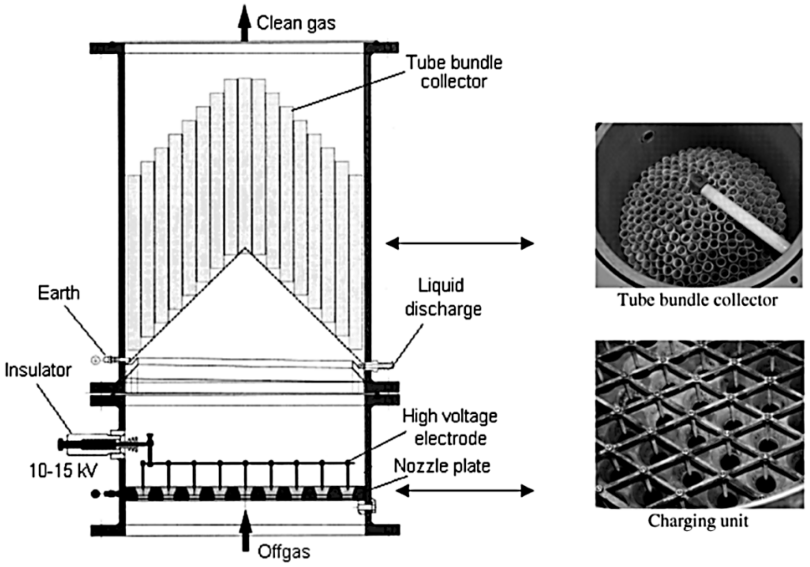

Figure 2.4: Schematic of a Corona Aerosol Abscheider (CAROLA).

Bayless *et al.* presented a membrane-based ESP that could be in dry [94] or wet [45, 95] style. The membrane-based collecting electrodes facilitate tension-based rapping, which shears the adhered particle layer from the surface of collecting electrodes more effectively than hammer-based rapping, and thus can also be used in dry ESPs. For wet application, membrane-based collecting electrodes reduce dry spots and prevent corrosion, further improving the collection efficiency.

Precipitator (Plate/Membrane)	Air Flow (acfm)	Voltage (kV)	Fields	Inlet Loading (mg/dscm)	Outlet Loading (mg/dscm)	Removal (%)
Plate	8394	45–47	1	67	14	79
Plate	8235	45–47	2	116	5	96
Plate	8410	45–47	2	113	11	90
Plate	8220	45–47	2	137	7	95
Plate	15,850	45–47	2	103	30	71
Plate	15,880	45–47	2	128	39	70
Membrane	8140	45–47	2	106	4	96
Membrane	15,330	45–47	2	115	22	81

Figure 2.5: Collection efficiency for membrane-based wet ESP.

Instead of using a hydrophilic membrane in a single-stage wet ESP, Lin *et al.* [44] used sand-blasted and TiO_2-coated copper plates as the collecting electrode to enhance hydrophobicity for the scrubbing water film. The experimental results showed that when this particular wet ESP was initially clean, the collection efficiency ranged from 96.9% to 99.7% for particles ranging from 16.8 nm to 615 nm in electrical mobility diameter at an aerosol flow rate of 5 L/min (residence time of 0.39 s) and an applied voltage of 4.3 kV. After heavy loading with TiO_2 nanopowder about 1.2 ± 0.06 g/plate, the collection efficiency for

corn oil particles was shown to reduce only slightly to 94.7% to 99.0% for the same particle-size range.

Misaka *et al.* [96-99] invented a moving-electrode ESP, as shown in Figure 2.6, that cleans the collecting electrodes using brushes, for the purpose of reducing particle re-entrainment. This type of ESPs is effective for high resistivity dusts (> 1012 ohm-cm), with a collection efficiency higher than 99%.

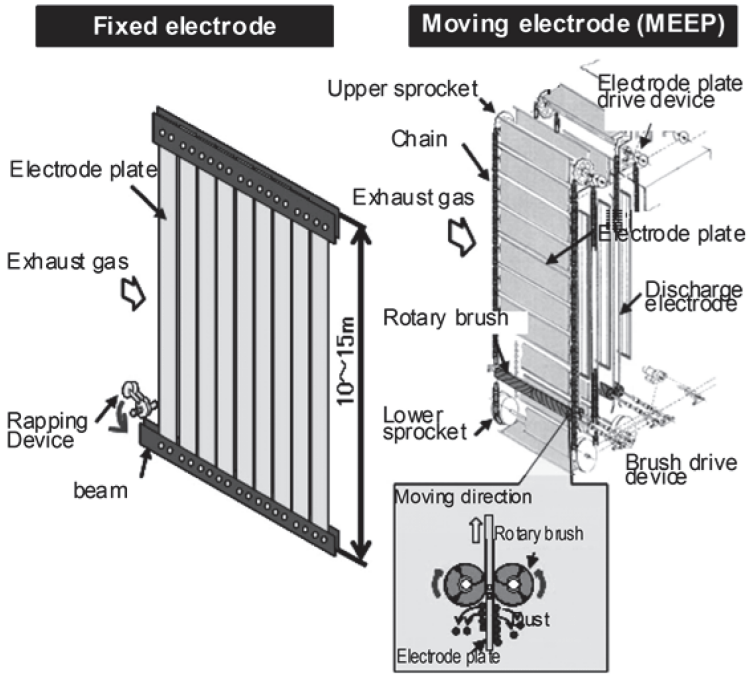

Figure 2.6: Structure of fixed electrode and moving electrode ESP.

Chen *et al.* [100, 101] developed a lentoid type ESP, which uses ionic wind to draw charged particles into the collecting chamber, as shown in Figure 2.7. This method increases the particle migration velocity and suppresses the particle re-entrainment. Particles in the

collecting chamber tend to agglomerate because of interactions between the electrostatic force and the turbulent effect.

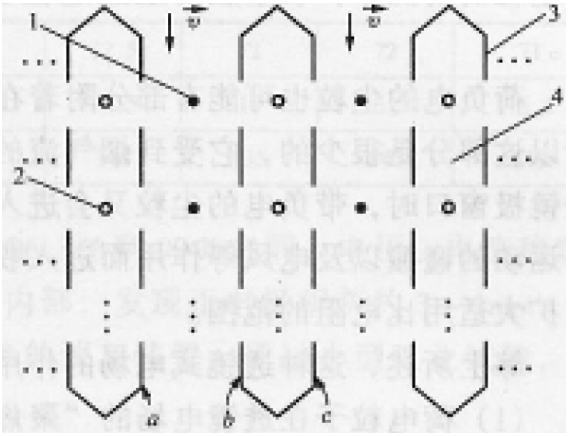

Figure 2.7: Lentoid ESP, where 1 is the negative electrode, 2 is the positive electrode, 3 is the lentoid electrode, and 4 is the collecting chamber.

Yamamoto *et al.* [102] utilized an ionic wind assisted structure to collect particles in a pocket zone where has no electric field, as shown in Figure 2.8, so particle re-entrainment is minimized. The collection efficiency is higher than 90% for a particle size of 20 nm to 200 nm. No particle re-entrainment was observed for particles smaller than 200 nm.

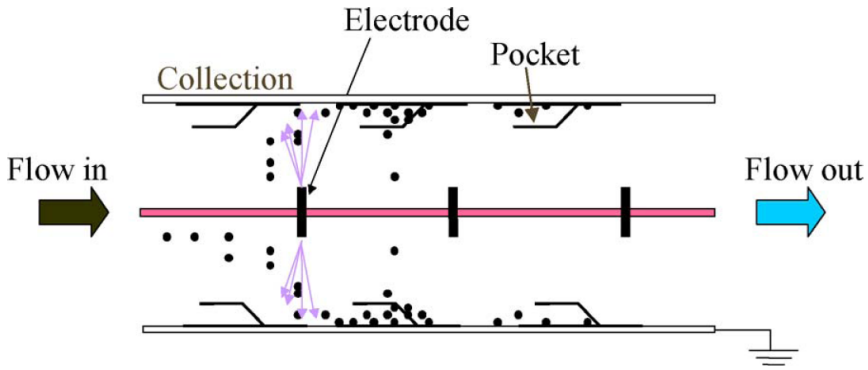

Figure 2.8: Ionic wind assisted ESP.

2.3 Introduction to Electrohydrodynamics

2.3.1 History of Electrohydrodynamics

Electrohydrodynamics is a phenomenon that refers to both electrical and mechanical energy transportation from ions to ions. When a positive electric field is applied between two wire electrodes that have significant curvature difference, the electric field strength near the high curvature electrode (corona electrode) is much stronger than that near the low curvature electrode (collecting electrode). When this electric field strength is stronger enough, free electrons passing by the corona electrode will be accelerated to a high velocity. When these high velocity electrons collide with other neutral molecules, the electrons originally reside in the neutral molecules are ejected. In other words, the charging status of these molecules is now positive. These charged substances then move forward along the electric field between the corona and collecting electrodes, resulting in a bulk air movement, also known as ionic wind.

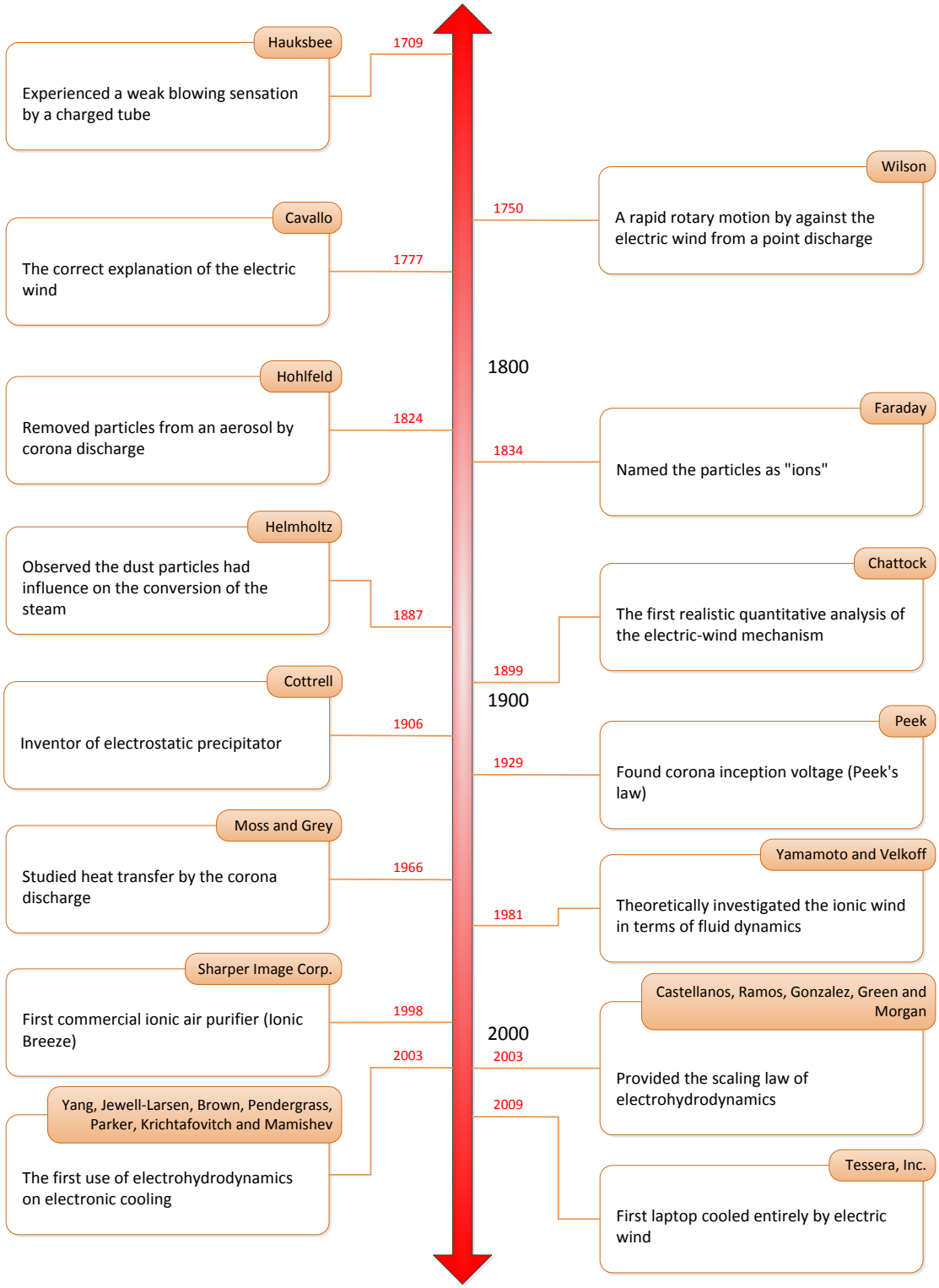

Figure 2.9: Chronology of important discoveries of electrohydrodynamics.

Though the applications of ionic wind have been developed for decades, the history of ionic wind can be traced back to 18th century. In 1709, Francis Hauksbee, the curator of instruments for the Royal Society of London, stated that he sensed a weak blowing to his face when holding a charged tube [103]. This acted as the foundation for the topic of ionic wind to both theoretical and experimental scientists during the time period. In 1750, Wilson developed the first electrostatic driving mechanism [104]. He succeeded in producing rapid rotary motion of a pinwheel by directing against it the ionic wind from a point discharging. Not until 1777, Cavallo proposed the explanation to ionic wind [105]. He wrote "the motion of fly depended upon the repulsion existing between bodies possessed of the same electricity; for whether the fly is electrified positively or negatively, the air opposite to the points of the wires (on account of the points easily transmitting electricity) acquireth a strong electricity analogous to that of the points; and therefore the air and the points must repell each other. This explanation is confirmed by observing that the above fly not only does not move in vacuo, but even if placed under a close receiver it will turn for a little while and then stop; for the quantity of air contained in the receiver may become readily and equally electrified." Cavallo's explanation to ionic wind has been generally accepted since then.

During the 19th and 20th centuries, the ionic wind became popular and well developed. In 1834, Michael Faraday reported two laws based on his studies on electrolysis, which became Faraday's first and second laws of electrolysis. Faraday also gave charged atoms and molecules the name "ion". According to the Philosophical Transactions of the Royal Society, Faraday said, "Finally, I require a term to express those bodies which can pass to

the electrodes, or, as they are usually called, the poles...I propose to distinguish such bodies by calling those anions which go to the anode of the decomposing body; and those passing to the cathode, cations; and when I have occasion to speak of these together, I shall call them ions" [106]. In Greek, "ion" means "going". Later in 1899, Chattock provided a quantitative analysis of ionic wind and implied ionic wind as a pressure generating source [107]. In 1929, Peek described the necessary voltage that makes corona discharge visible between two wires, also known as corona inception voltage (CIV) [53] or Peek's law. In 1981, Yamamoto and Velkoff proposed a model to describe the ionic wind in terms of fluid dynamics, which is widely known today as electrohydrodynamics [19]. Yamamoto and Velkoff attempted to explain why the ionic wind (also known as secondary flow) generated by corona discharge cannot be ignored, and demonstrated the strong interactions take place owing to the induced circulatory cells. In 2003, Castellanos *et al.* discussed the movement of liquid, and the behavior of particles in aqueous solutions subjected to AC electric fields and determined a general understanding of the scaling laws governing such EHD-based systems [108].

2.3.2 Electrohydrodynamics-based Applications

2.3.2.1 Gas-Particle Separation

The "ionic wind" filtration, also known as electrostatic precipitator or electric air cleaner (EAC), has been known since 1824 when Hohlfeld used corona discharge to clean smoke contained in a bottle [17]. Helmholtz in 1887 observed the dust particles had influence on the direction of a jet steam, and this provided the basic belief that air molecules can be

charged [109, 110].

The first ESP was built by Dr. Cottrell in 1907 [111]. The commercial feasibility of ESPs was first demonstrated at a sulphuric acid plant of E.I. DuPont de Nemours Powder Works in Pinole, California, where arsenic vapors were impacting the operation of their catalytic converters [112]. In 1912, Western Precipitation designed and constructed the first large ESP, which was installed at the Riverside Portland Cement Company in Crestmore, California, for the recapture of cement kiln dust. This plant handled a gas flow of 470 m/s at the temperature of 400 to 500 degree C, and this ESP unit remained in service for 54 years [113, 114].

2.3.2.2 Thermal Management

For the past 40 years, the semiconductor industry has been following the Moore's Law, stating that the number of transistors on integrated circuits doubles every 24 months [115, 116]. This implies that the challenges in dissipating heat also double in importance as well. The traditional cooling strategy is to use a rotary fan to create airflow in order to increase the convective heat transfer coefficient. All due to the moving parts, rotary fans do, however, introduce problems. First, the performance of rotary fans decreases over time due to the accumulation of the dust on their blades. Second, rotary fans create noise because of the interaction between the blade's tip and air. Third, rotary fans are usually physically big. Thus, emerging technologies that generate airflow without any moving parts, such as ionic wind, are attractive to the semiconductor and computer industries.

The pioneers, Moss and Grey, in 1966, started studying the heat transfer behavior in pipe flow by the application of a DC electric field [117]. In 2003, Yang *et al.* used corona air propulsion to improve airflow patterns in narrow channels for cooling high density electronic devices [118]. For further realistic practice in electronic cooling, in 2009, Jewell-Larsen *et al.*, applied the ionic wind pump to replace the blower in a laptop [119]. Their results show that the EHD-based cooling system has promising performance with reduced hardware volume and improved acoustics.

2.3.2.3 Propulsion

The main concept of EHD propulsion is to convert electrical energy into mechanical energy. The concept of EHD propulsion was first proposed in 1928 [120], and has developed since the 1960s [121-124]. The applications of so called "ionic aircraft" are still limited because the propulsive forces are relatively low. However, "ionic aircraft" is still attractive to certain applications such as unmanned surveillance [125, 126] and spacecraft [6, 121, 127] because of its ultra-silent, vibration-free, fuel-free, scalable, and simple structure.

2.3.3 Technical Insight of Electrohydrodynamics

The principles behind EHD involve fluid dynamics, electrostatics, and charge transport. Figure 2.10 shows a model of positive discharge. The corona electrode operates at a high positive voltage while the collecting electrode is grounded, creating an ionization region and a unipolar region between them. The ionization region is near the corona electrode. In

this region, the electric field intensity is extremely high because there is a huge curvature difference between the corona electrode and the collecting electrode. Once free electrons have passed through the ionization region, they accelerate to a certain high velocity (i.e., they have high kinetic energy). When these moving electrons collide with neutral air molecules and particles, the electrons originally in these air molecules and particles are ejected. In other words, the charging state of such air molecules and particles are positive. Positive ions move toward the collecting electrode along the electric field in the unipolar drift region, and settle on the collecting electrode.

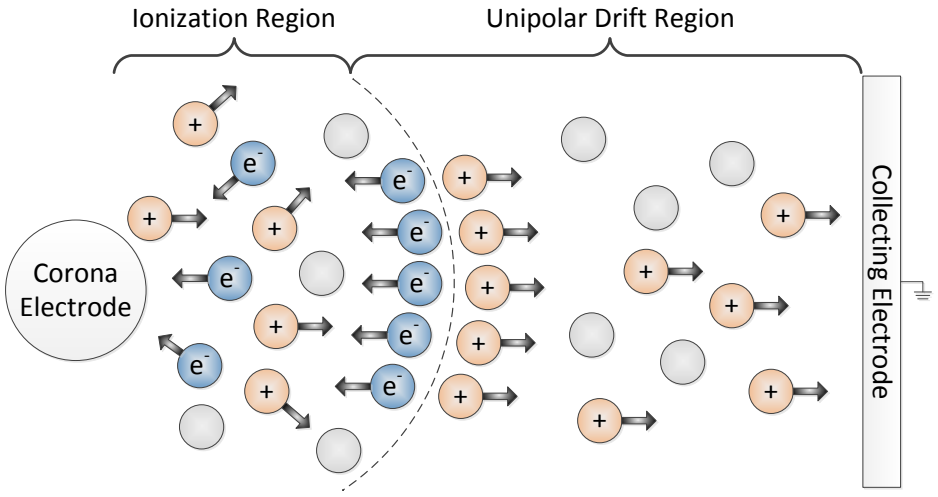

Figure 2.10: A model of positive discharge. There are two regions between the corona and collecting electrodes. The ionization region, or corona plasma region, surrounds the corona electrode. The unipolar drift region is the region between the ionization boundary and the collecting electrode.

Figure 2.10 is also a two-region model of positive discharge. The first region is the ionization region, which exists close to the corona electrode. Within this region, there are

both positive and negative ions. Under positive discharge, negative ions are attracted to the corona electrode while positive ions are repelled. Because the radius of corona wire is much smaller than the distance between the corona and collecting electrodes, the electric field strength at the corona wire surface E_w (at room temperature, normal pressure, and smooth wire surface) can be estimated by Peek's law [53],

$$E_w = E_0 \left(1 + \frac{2.62 \times 10^{-2}}{\sqrt{R_w}}\right) \tag{2.23}$$

where $E_0 = 3.23 \times 10^6$ (V/m) is the breakdown electric strength of air, and R_w is wire radius. Thus, the radius of the ionization region R_i can be obtained by applying Kaptsov's assumption [128] that at $R = R_0$, $E = E_0$,

$$E_0 = E_w \frac{R_w}{R_i} \tag{2.24}$$

$$E_0 = E_0 \left(1 + \frac{2.62 \times 10^{-2}}{\sqrt{R_w}}\right) \frac{R_w}{R_i} \tag{2.25}$$

$$R_i = R_w \left(1 + \frac{2.62 \times 10^{-2}}{\sqrt{R_w}}\right) \tag{2.26}$$

Also, the electric potential drop over the ionization region can be obtained by integrating the electric field strength,

$$E = E_w \frac{R_w}{r} \tag{2.27}$$

$$V_i - V_w = \int_{R_w}^{R_i} E dr \tag{2.28}$$

$$V_i = V_w - E_w R_w \ln \frac{E_0}{E_w} \tag{2.29}$$

where V_i is the electric potential at ionization boundary, V_w is the electric potential at corona wire surface, and r is the radial distance from the curvature center of corona wire.

The second region is the unipolar drift region where the unipolar ions are guided along the electric field toward the collecting electrode. In a numerical point of view, the behavior in this region can be solved by coupling the Navier-Stoke's equation with the charge transport equation. The Navier-Stoke's equation describes the motion of fluid with the influence of body forces. These body forces come from the Coulomb force which is the result of electrostatic interactions between charged ions. In a steady-state assumption, the continuity equation of electric charge should be satisfied. Therefore, with knowledge of the current density, space charge density, and fluid velocity field, the equation of charge transport equation and space charge density can be derived and solved.

In order to make corona discharge take place and to prevent point discharging, the applied voltage should lie between the corona onset voltage and the air breakdown voltage [53]. The operating polarity can be either positive or negative. The corona current generated by

the negative corona is typically higher than that generated by the positive corona because there are additional electrons released from the corona electrode under the negative corona. However, the current of the negative corona is also higher because of these additional electrons, and the energy efficiency of a negative corona is hence lower compared to that of a positive corona.

2.3.4 Governing Equations of Electrohydrodynamics

The underlying principles of EHD are electrostatics and fluid mechanics. The governing equations for these two physics are the Poisson's equation, the charge transport equation, the Navier-Stoke's equations, and the continuity equation.

2.3.4.1 Poisson's Equation

The Poisson's equation states the relationship between the electric field and the charge density, combined with the Gauss's law,

$$\nabla \cdot \mathbf{E} = \frac{q}{\varepsilon_0} \tag{2.30}$$

$$\mathbf{E} = -\nabla V \tag{2.31}$$

$$\nabla^2 V = -\frac{q}{\varepsilon_0} \tag{2.32}$$

where $\mathbf{E}$ is electric field, q is charge density, V is electric potential, and ε_0 is the permittivity of free space.

2.3.4.2 Charge Transport Equation

The charge transport equation is derived from the continuity equation of current density, assuming the system is conservative in this case.

$$\nabla \cdot \mathbf{J} = 0 \tag{2.33}$$

$$\mathbf{J} = \mu_E \mathbf{E} q + \mathbf{U} q - D \nabla q \tag{2.34}$$

$$-\nabla \cdot (\mu_E \nabla V q + D \nabla q) + \mathbf{U} \cdot \nabla q = 0 \tag{2.35}$$

where $\mathbf{J}$ is current density, μ_E is ion mobility, $\mathbf{U}$ is the velocity field of fluid, and D is the diffusivity coefficient of ions.

2.3.4.3 Navier-Stoke's Equation

The Navier-Stoke's equations describe fluid behavior, including velocity and pressure fields. With the incompressible assumption, the fluid density is a constant. If the fluid behavior is assumed to be steady-state, the time dependent terms can be dropped out. On the other hand, the body force can be stated by the product of charge density and electric potential,

coming from the charge transport equation and the Poisson's equation.

$$\rho \mathbf{U} \cdot \nabla \mathbf{U} = -\nabla p + \mu \nabla^2 \mathbf{U} + \mathbf{f} \tag{2.36}$$

$$\mathbf{f} = -q \nabla V \tag{2.37}$$

$$\rho \mathbf{U} \cdot \nabla \mathbf{U} = -\nabla p + \mu \nabla^2 \mathbf{U} - q \nabla V \tag{2.38}$$

where ρ is fluid density, p is fluid pressure, μ is dynamic viscosity, and $\mathbf{f}$ is body force.

2.3.4.4 Continuity Equation of Flow

Regardless of any assumptions made for the fluid, such as steady or unsteady, viscous or inviscous, and compressible or incompressible, the equation of continuity should be satisfied to meet the requirement of mass conservation,

$$\frac{\partial \rho}{\partial t} + \nabla \cdot (\rho \mathbf{U}) = 0 \tag{2.39}$$

Since the fluid is in steady-state in this case, the time dependent term is dropped out, and the density in (2.39) is can be removed using the assumption of incompressible flow,

$$\nabla \cdot \mathbf{U} = 0 \tag{2.40}$$

2.3.4.5 Turbulence Modeling

For a two dimensional and incompressible steady flow, the standard linear $k-\varepsilon$ Reynolds-averaged Navier-Stokes (RANS) model can be described by the equations of momentum and continuity,

$$\frac{\partial \rho u_j u_i}{\partial x_j} = -\frac{\partial p}{\partial x_i} + \frac{\partial}{\partial x_j}\left[\mu\left(\frac{\partial u_i}{\partial x_j} + \frac{\partial u_j}{\partial x_i}\right)\right] - \frac{\partial}{\partial x_j}\left(\rho\overline{u_i' u_j'}\right) \tag{2.41}$$

$$\frac{\partial u_i}{\partial x_i} = 0 \tag{2.42}$$

where ρ is fluid density, u_i is fluid velocity, p is fluid pressure, μ is fluid dynamic viscosity, and $\overline{u_i'}$ is fluid fluctuation velocity. The last term of right-hand side in (2.41) is the Reynolds stress tensor, and its Boussinesque eddy viscosity model is,

$$-\rho\overline{u_i' u_j'} = \mu_t\left(\frac{\partial u_i}{\partial x_j} + \frac{\partial u_j}{\partial x_i}\right) - \frac{2}{3}\rho k \delta_{ij} \tag{2.43}$$

$$\mu_t = \frac{C_\mu \rho k^2}{\varepsilon} \tag{2.44}$$

$$k = \frac{1}{2}\overline{u_i' u_i'} \tag{2.45}$$

$$\varepsilon = \nu \frac{\partial^2 \overline{u_i'}}{\partial x_j \partial x_j} \tag{2.46}$$

where μ_t is eddy viscosity, k is turbulent kinetic energy, δ_{ij} is the Kronecker delta, C_μ is a constant, ε is dissipation rate, and ν is kinematic viscosity.

2.4 Summary

This chapter reviews the most fundamental principles behind electrostatic precipitators, including particle charging, particle kinetics, and particle collection efficiency. Moreover, this chapter discusses Deutsch-Anderson equation that is used to theoretically predict the collection efficiency of ESPs. Several important innovations on ESPs in the past decades are presented as well, especially focusing on the innovations of the collecting electrodes. This chapter also introduces the history and emerging applications of electrohydrodynamics such as gas-particle separation, thermal management, and propulsion. The demonstrations of the governing equations behind electrohydrodynamics are covered as well, including the Poisson's equation for electric field and the Navier-Stoke's equations for flow field. The linear $k - \varepsilon$ RANS model for turbulent flow model is also presented at the end of this chapter.

Chapter 3

FOAM-COVERED ELECTROSTATIC PRECIPITATORS

When the adhesion between the collected particles and the collecting electrodes is not strong enough, the collected particles could re-enter the environment due to external disturbances such as strong airflow or vibrations [12, 68-70]. Such particle dislodging, also known as particle re-entrainment, lowers the collection efficiency. By covering the collecting electrodes with a porous material, the particle re-entrainment and several drawbacks that exist in traditional ESPs can be reduced and improved.

3.1 Proof-of-Concept Prototype

3.1.1 Design Concept

To reduce the chance of particle re-entrainment of an ESP, the key idea of the particle-trapping mechanism is to securely store the particles in some spaces that have relatively low disturbances. To achieve this goal, the collecting electrodes are covered with porous and electrically conductive foam, so that particles fall into the pores of foam rather than attach to the flat surfaces of collecting electrodes. Because of the irregularities of the pores and low disturbances inside the pores, the particles collected inside the pores therefore have a lower chance of returning to the environment. In addition to the reduction of particle

re-entrainment, the weak electrical conductivity of the foam has several features. First, it ensures the electric field strength between the repelling electrodes and the collecting electrodes not decrease significantly. Second, it prevents spark discharge (short circuit) between the electrodes. When spark discharge occurs between the electrodes, there is no electric field between the electrodes, which means the ESP is not working properly at that moment. Third, it prevents the conductive particles from fast discharging. Fourth, the foam is flame-retardant, so there is little risk of causing a fire.

Beyond the collection efficiency, the energy efficiency is also a key factor in evaluating the performance of an ESP. The system energy efficiency of a filtration system greatly depends on the system pressure drop that mainly comes from air filters. Because the collection efficiency is improved by attaching the foam to the collecting electrodes, the pre- and/or post-filters that are used to improve the collection efficiency of traditional ESPs are not necessary anymore. The energy efficiency of foam-covered ESPs is therefore higher than that of traditional ESPs that have pre- and/or post-filters.

For two-stage, non-industrial foam-covered ESPs, there are no significant corona currents flowing into the collecting electrodes and the particle concentration is much lower than in industrial environments; thus, the chance of a back corona is low. The fact is that no back corona effects were observed during any measurements presented in this dissertation.

3.1.2 Prototype Assembly

Figure 3.1 shows a schematic of a foam-covered ESP. The cross-sectional area of the foam-covered ESP prototype under test is 250 mm by 250 mm, and the depth is 130 mm, including the enclosure. The main components of this prototype are:

1) 1 rigid plastic made enclosure

2) foam (sheet)

3) 15 tungsten made corona electrodes (wire)

4) 16 aluminum made exciting electrodes (rod)

5) 5 aluminum made collecting electrodes (plate)

6) 6 aluminum made repelling electrodes (plate)

7) 2 metal connectors (strip)

Figure 3.2 shows a CAD drawing and Figure 3.3 is the zoom-in CAD drawing of the top side of the prototype. Figure 3.4, Figure 3.5, and Figure 3.6 are pictures that show a working prototype. The collecting and repelling electrodes are arranged alternatively, and they are inserted into pre-cut slots for convenient installation and removal. A metal strip connects all of the collecting electrodes, and a separate metal strip connects all of the repelling electrodes. A spring is used to make sure the corona electrodes have proper tensile strength. Both sides of the collecting electrodes are covered with foam, whereas only the edges of the repelling electrodes are covered with foam in order to minimize spark discharge at the sharp edges. The length of the collecting electrodes is slightly longer than the repelling electrodes, thus further reducing the chance of spark discharge between the electrodes and improving the

pattern of electric field to have better collection efficiency. The charger is made of exciting and corona electrodes. The exciting electrodes are arranged in parallel with and adjacent next to the corona electrodes, so that corona currents flow between the corona and exciting electrodes.

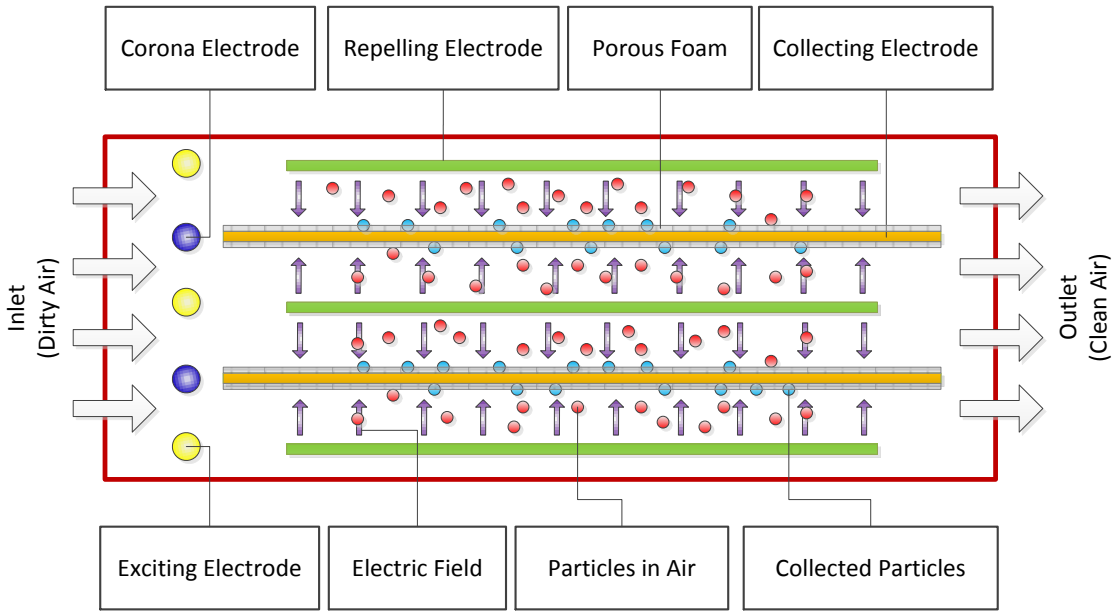

Figure 3.1: A schematic of the foam-covered ESP, with porous foam attached to the collecting electrodes. Not drawn to scale.

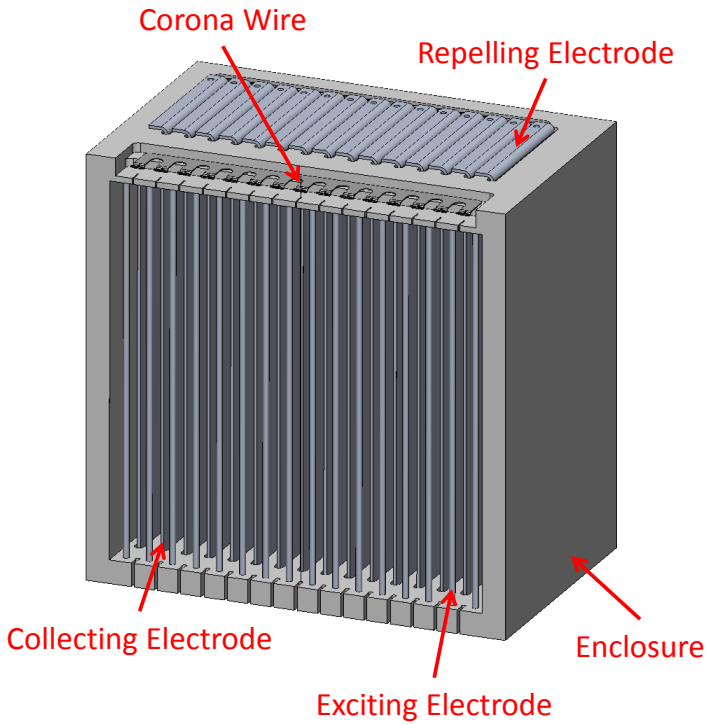

Figure 3.2: CAD drawing of the foam-covered ESP.

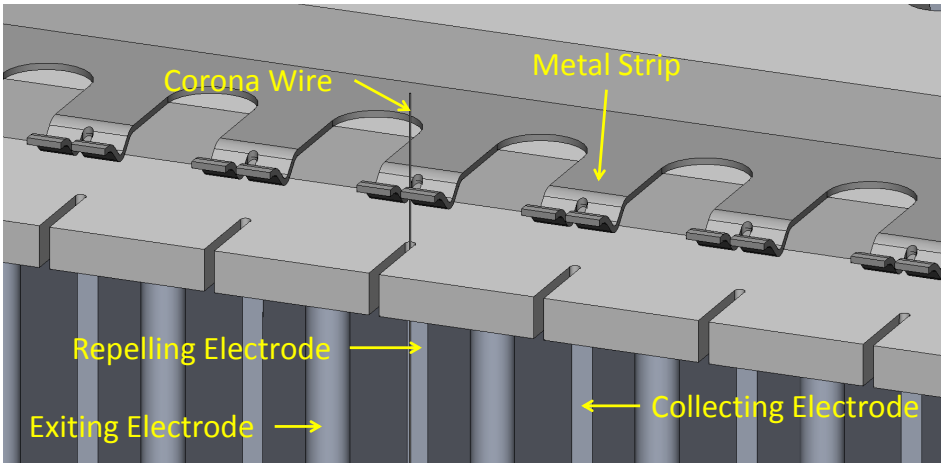

Figure 3.3: Zoomed-in of the CAD drawing of the foam-covered ESP.

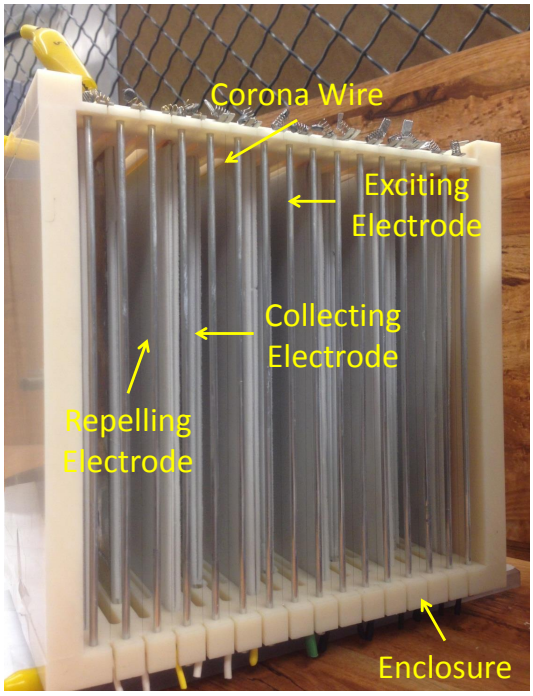

Figure 3.4: Front-view of the foam-covered ESP prototype.

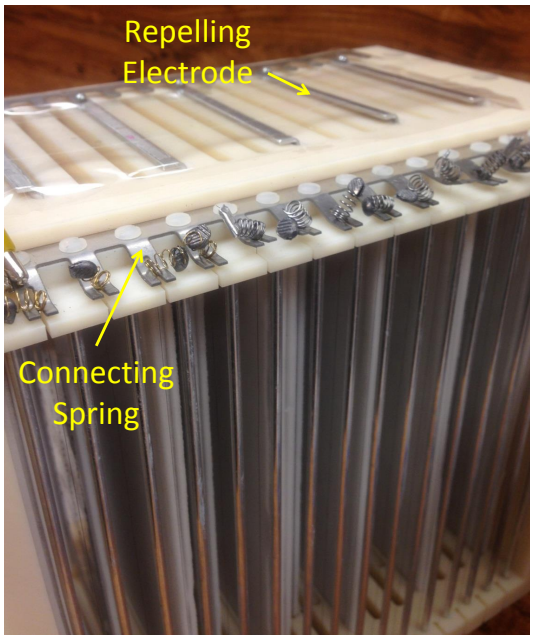

Figure 3.5: Top-view of the foam-covered ESP prototype.

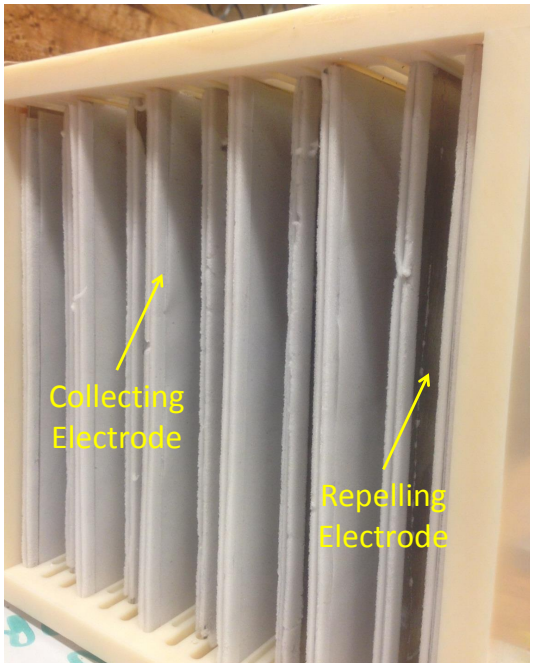

Figure 3.6: Back-view of the foam-covered ESP prototype. The edge of the repelling electrodes is covered by foam, whereas all sides of the collecting electrodes are covered with foam.

3.2 Experimental Setup

Figure 3.7 shows the schematic of the experimental setup, and Figure 3.8 shows the actual experimental setup. Air is drawn into the system using traditional fans, and then flows through a flow straightener (stabilizer) to ensure uniform airflow. The airflow velocity, from 0.5 m/s to 2.5 m/s, is varied through adjustments to the input power of the fans. The stabilized air then flows through the foam-covered ESP prototype. The particle counter (Haltech HPC600) is placed right after the ESP to measure the number of particles in the air stream in terms of particle sizes. The minimum measurable particle size is 0.3 µm, and the particle counting efficiency is 100 ± 10% at 0.45 µm. A voltage DC power supply

(Hipotronics) provides positive high voltage to the corona electrodes, and another power supply (Spellman SL150) supplies positive high voltage to the repelling electrodes. Both collecting and exciting electrodes are grounded. The positive corona is used in this setup, for non-industrial applications, because positive corona produces less ozone [12, 129], operates quieter [40], and has lower corona power than negative corona.

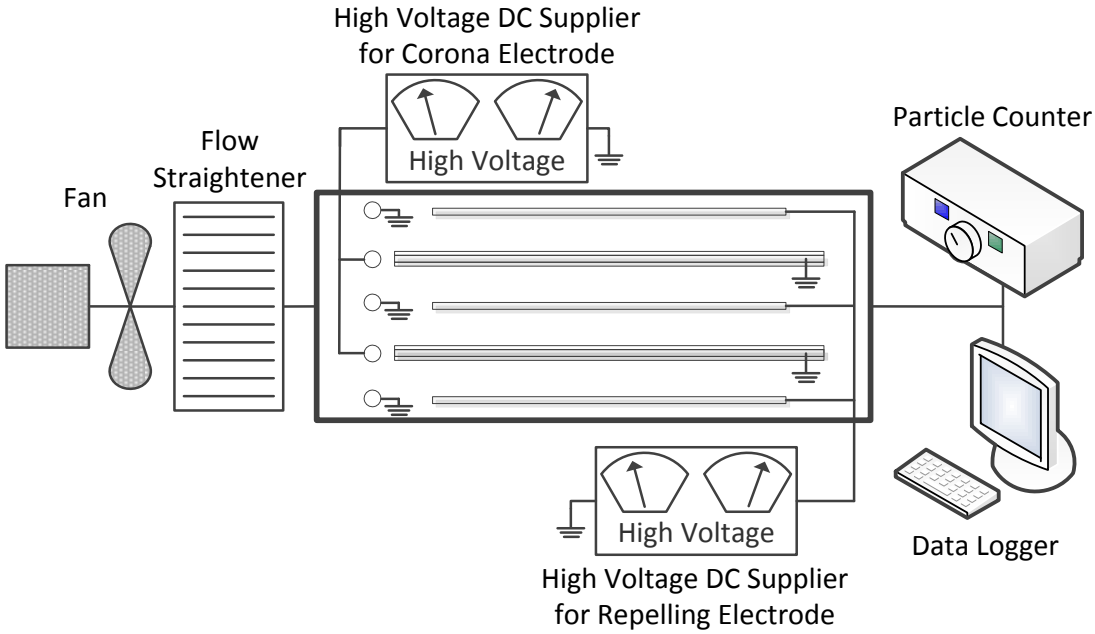

Figure 3.7: The schematic of the experimental setup of the foam-covered ESP under test.

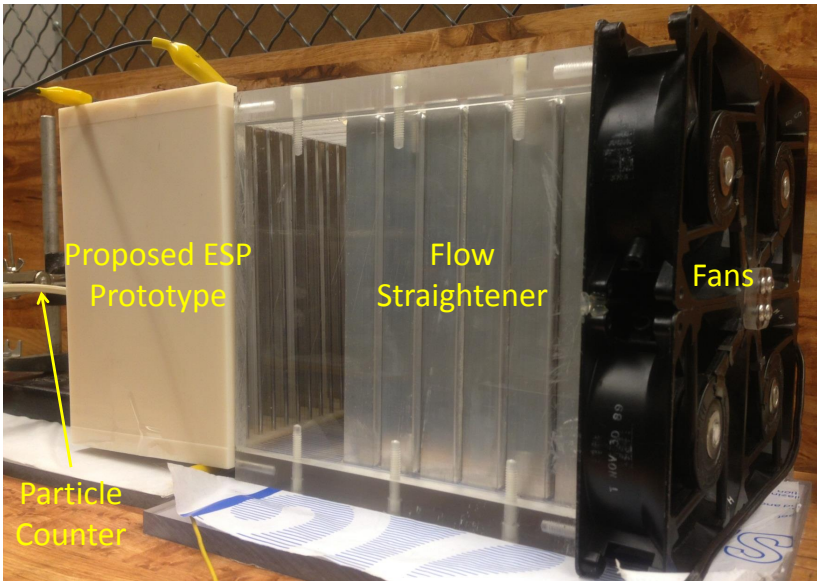

Figure 3.8: Experimental setup of the foam-covered ESP under test.

3.3 Results and Discussion

3.3.1 Current-Voltage Characteristic

Figure 3.9 shows the current-voltage and power-voltage characteristic curves of the foam-covered ESP under test, which was measured at stationary conditions (no free airflow and no repelling voltage). The corona onset voltage is 4.07 kV. Spark discharge was observed when the corona voltage increased higher than 5.2 kV. Corona power grows with corona voltage nonlinearly, which follows the Townsend law [130].

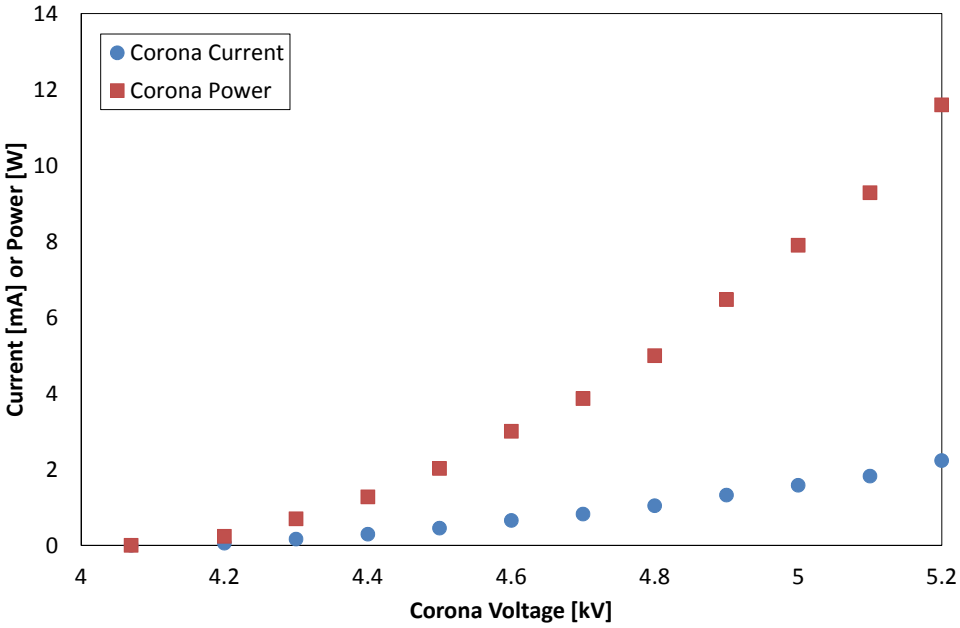

Figure 3.9: The current-voltage and power-voltage characteristic curves of the foam-covered ESP under test.

3.3.2 Particle Collection Efficiency

Particle collection efficiency, or, simply, collection efficiency, is one of the critical metrics to evaluate the performance of ESPs. In addition to the collection efficiencies that are obtained from the experiments, this section also compares the experimental results with theoretical results.

In the experiments, the number of background particles is measured when the ESP is turned off. The collection efficiency, η, is defined as,

$$\eta = \left(1 - \frac{N_{outlet}}{N_{background}}\right) \times 100\% \tag{3.1}$$

where N_{outlet} is the number of particles at outlet, and $N_{background}$ is the number of background particles. Alternatively, the number of particles shown in (3.1) can be substituted by particle concentration.

The Deutsch-Anderson equation of collection efficiency [85] is presented and discussed in Chapter 2. Nonetheless, the Deutsch-Anderson equation neglects turbulent diffusion and assumes that particle concentration is uniformly distributed across any cross-section of the airflow channel. In other words, particle concentration is well-mixed by the flow. These assumptions could have significant influence on the collection efficiencies in certain cases. Cooperman [87] and Zhang [88] proposed equations that are used to evaluate the collection efficiency of ESPs, but taking turbulent diffusion into account. This section uses these three pioneers' work to predict the collection efficiencies of the FC-ESPs under various operating conditions such as corona voltage, repelling voltage, and particle sizes. The results are verified and compared with the experimental data.

3.3.2.1 Cooperman's Equation of Collection Efficiency

Cooperman's idea was that particle migration velocity, as shown in (2.16), should be lower than the natural velocity, because particle diffusion has to be taken into account in the direction transverse to the free airflow [87]. Additionally, the convective transport of particles decreases, while diffusive transport of particles increase when airflow velocity decreases [87]. Cooperman solved the steady-state convective diffusion equation, derived from the particle continuity equation, as shown in Figure 3.10 and (3.4). Two boundary conditions were

applied in Cooperman's work, as shown in (3.5). The first boundary condition is that constant particle concentration across y-direction at the inlet. The second boundary condition states that the particle concentration at x-infinity is zero, and it can be justified by an ideal situation that all particles are collected when the collecting electrode is infinite long.

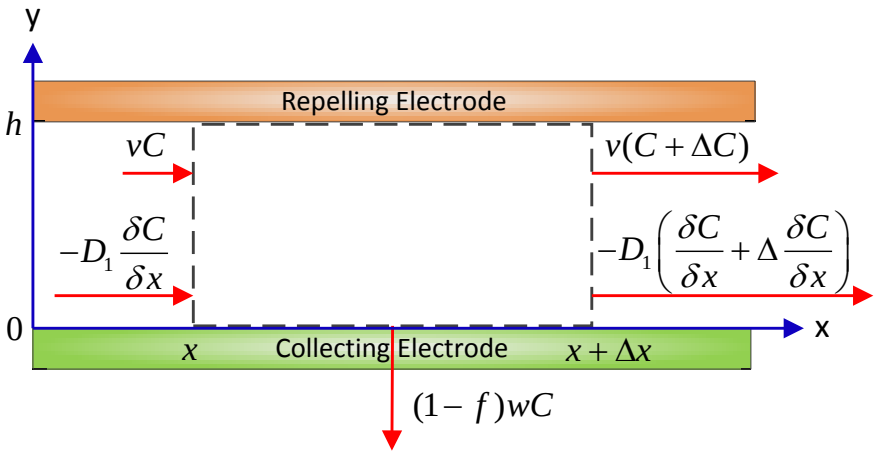

Figure 3.10: Particle transport in a control volume in the collector of an ESP.

$$h\left(vC - D_1\frac{dC}{dx}\right) = h\left[v\left(C+\Delta C\right) - D_1\left(\frac{dC}{dx} + \Delta\frac{dC}{dx}\right)\right] + \left(1-f\right)wC\Delta x \tag{3.2}$$

$$\begin{cases} \Delta C = \dfrac{dC}{dx}\Delta x \\ \Delta\dfrac{dC}{dx} = \dfrac{d^2C}{dx^2}\Delta x \end{cases} \tag{3.3}$$

$$\frac{d^2C}{dx^2} - \frac{v}{D_1}\frac{dC}{dx} - (1-f)\frac{w}{hD_1}C = 0 \tag{3.4}$$

$$BCs \begin{cases} C(0,y) = C_{in} \\ C(\infty,y) = 0 \end{cases} \tag{3.5}$$

where h is the width of the airflow channel, D_1 is the particle diffusion coefficient in direction of airflow (longitudinal), and f is friction factor or the ratio of particle transport by turbulence away from an electrode to the rate of electrostatic particle transport towards the electrode [131]. Equation (3.4) is a linear first order differential equation, with the boundary conditions shown in (3.5), the solution of the particle concentration, C, can be expressed by (3.6).

$$C = C_{in} exp(-kx) \tag{3.6}$$

$$k = -\frac{v}{2D_1} + \sqrt{\frac{v^2}{4D_1^2} + (1-f)\frac{w}{hD_1}} \tag{3.7}$$

Therefore, at the outlet, $x = L$, the particle collection efficiency can be obtained using (3.1).

$$\eta_{cooperman} = 1 - \frac{C(L)}{C_{in}} \tag{3.8}$$

$$\eta_{cooperman} = 1 - exp\left(\frac{vL}{2D_1} - L\sqrt{\frac{v^2}{4D_1^2} + (1-f)\frac{w}{hD_1}}\right) \tag{3.9}$$

The friction factor can be expressed by the Reynold's number, and the longitudinal particle diffusion coefficient is a function of the friction factor.

$$\frac{1}{f^{0.5}} = -1.8log_{10}\left(\frac{6.9}{Re}\right) \tag{3.10}$$

$$U_\tau = \sqrt{\frac{fv^2}{8}} \tag{3.11}$$

$$D_t = 0.12U_\tau h \tag{3.12}$$

where Re is the Reynold's number, U_τ is friction velocity, D_t is turbulent diffusivity. Note that the turbulence in an ESP is dominated by the free airflow, and hence in this case, the particle diffusion coefficient D_1 equals to the turbulent diffusivity D_t. The friction factor and the particle diffusion coefficient vary with the free airflow velocity.

3.3.2.2 Zhang's Equation of Collection Efficiency

Zhang *et al.* proposed another equation of collection efficiency by casting and solving the convective diffusion equation with zero flux boundary conditions at the center plane between two adjacent collecting electrodes [88], which is the repelling electrode in a two-stage ESP.

The justification is that the particle concentration decays exponentially from the collecting electrode to the repelling electrode, as experimentally demonstrated by Leonard *et al.* [132], as shown in Figure 3.11. Besides, both longitudinal and transverse diffusion are taken into account in Zhang's model.

$$D_1\frac{\partial^2 C}{\partial x^2}+D_2\frac{\partial^2 C}{\partial y^2}-v\frac{\partial C}{\partial x}-w\frac{\partial C}{\partial y}=0 \tag{3.13}$$

$$BCs\begin{cases} C\left(0,y\right)=C_{in} \\ C\left(\infty,y\right)=0 \\ D_2\dfrac{\partial C\left(x,0\right)}{\partial y}-vh\dfrac{\partial C\left(x,0\right)}{\partial x}-wC\left(x,0\right)=0 \\ \dfrac{\partial C\left(x,h\right)}{\partial y}=0 \end{cases} \tag{3.14}$$

$$\eta_{zhang}=1-exp\left(-F\frac{wL}{vb}\right) \tag{3.15}$$

$$F=\frac{v^2b}{2wD_1}\left[\sqrt{1+\frac{w^2}{v^2}\frac{D_1}{D_2}\left(1+\frac{4\theta^2D_2^2}{w^2b^2}\right)}-1\right] \tag{3.16}$$

$$D_2=D_t+D_B \tag{3.17}$$

$$D_B=\frac{KTC_c}{6\pi\mu r_p} \tag{3.18}$$

where D_2 is the particle diffusion coefficient transverse to the free airflow, θ is a constant, and D_B is the Brownian diffusivity [86].

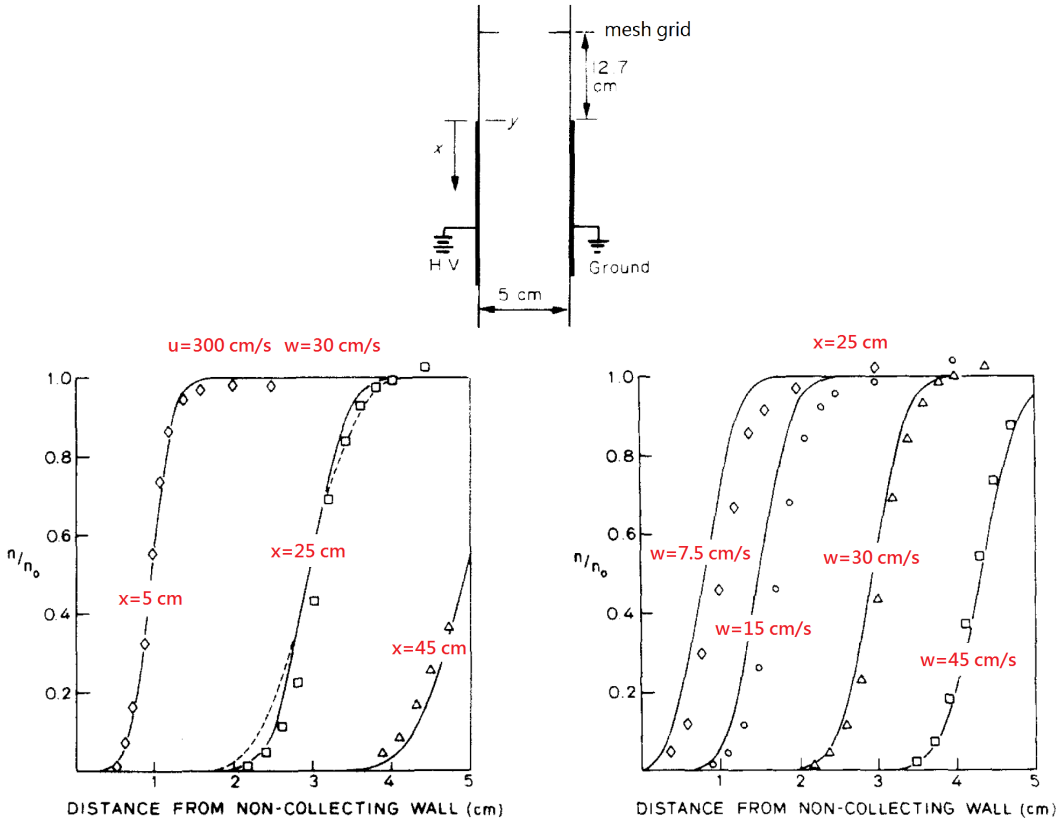

Figure 3.11: Particle concentration profiles [132].

3.3.2.3 Experimental Results - Collection Efficiencies versus Corona Voltages

To study the collection efficiencies at various corona voltages, several measurements are conducted. The repelling voltage is maintained at 15 kV, and the collecting electrodes are grounded. The airflow velocity is maintained at 2.5 m/s. The particle counter is used to measure the cumulative number of particles of 0.3 µm. Table 3.1 shows the values used

in predicting the collection efficiencies of FC-ESPs by using Deutsch's, Cooperman's, and Zhang's equations of collection efficiency. Figure 3.12 shows both experimental and predicted collection efficiencies and the corresponding corona power at different corona voltages.

Table 3.1: Values for all parameters used in predicting collection efficiencies of FC-ESPs.

Parameter	Value
Particle diameter, d_p	0.3 µm
Cunningham slip correction factor, C_c	1.78
Ion mobility, b	1.33×10^{-4} $m^2s^{-1}V^{-1}$
Time constant of ion concentration, N_0t	10^{13} $\#^1m^{-3}s^1$
Relative permittivity, ε_p	1.6
Boltzmann constant, K	1.38×10^{-23} $m^2kg^1s^{-2}K^{-1}$
Temperature, T	303 K
Root-mean-square thermal velocity of ions, v_{rms}	240 m^1s^{-1}
Air viscosity, μ	1.827×10^{-5} $kg^1m^{-1}s^{-1}$
Element charge, e	1.6×10^{-19} C
Depth of the collecting electrode	8 mm
Height of the collecting electrode	200 mm
Airflow channel width (include 2 mm foam)	20 mm

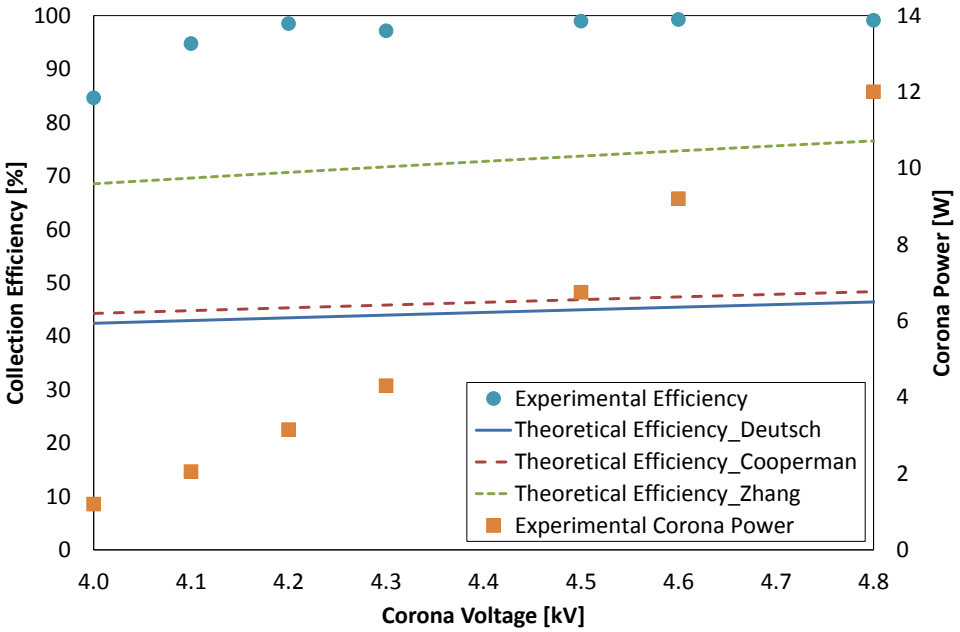

Figure 3.12: The collection efficiencies of the foam-covered ESP at different corona voltages. The particle diameter is 0.3 µm. The airflow velocity is 2.5 m/s. The repelling voltage is 15 kV.

Looking at the predictions, the collection efficiency is monotonically proportional to the corona voltage. The collection efficiencies predicted by Deutsch's and Cooperman's work are considerably lower than those predicted by Zhang's work, because Deutsch's and Cooperman's work considered the particle concentration along the transverse to airflow direction as a constant [86]. In Zhang's work, the particle flux to the wall is greater than that with constant particle concentration. Thus, Zhang's results are better fit with the experimental results.

Looking at the experimental data, the collection efficiency increases significantly from 84% to more than 99% when the corona voltage increases from 4.0 kV to 4.2 kV. At 4.0

kV corona voltage, a large number of particles are not sufficiently charged, resulting in a low collection efficiency. This is also the reason that the predicted collection efficiencies are linearly proportional to the corona voltage, i.e., particles are always assumed to be fully charged in the theoretical derivation. A large number of particles are well charged when the corona voltage is higher than 4.2 kV, resulting in a nearly 99% collection efficiency, which is very competitive to that of HEPA filters and existing commercial ESPs that have pre- and/or post-filters.

Although the experimental collection efficiencies exhibit a good agreement with the theoretical results in trend, the sources of the absolute errors might be resulted from 1) non-ideal conditions in the experiments such as particle charging, and 2) the foam suppresses the particle re-entrainment and theories used do not take it into account.

The foam-covered ESP under test achieves a nearly 99% collection efficiency at a corona voltage of 4.2 kV, with a corresponding corona power of 3.2 W. Further increases in the corona voltage do not improve the collection efficiency, but results in a significant increase in the corona power. For example, the corona power at 4.8 kV corona voltage is almost four times as much as when the corona voltage is 4.2 kV. Note that the electric current flowing between the repelling and collecting electrodes, and between the corona and exciting electrodes, is extremely small, the power consumption between these two sets of electrodes is neglected.

3.3.2.4 Experimental Results - Collection Efficiencies versus Repelling Voltages

To study the effects of the repelling voltage on the collection efficiency, the experiments are conducted with the following fixed parameters: 1) the airflow velocity is 2.5 m/s, and 2) the corona voltage is 5 kV. Figure 3.13 shows the experimental and theoretical results between the repelling voltage and the collection efficiency.

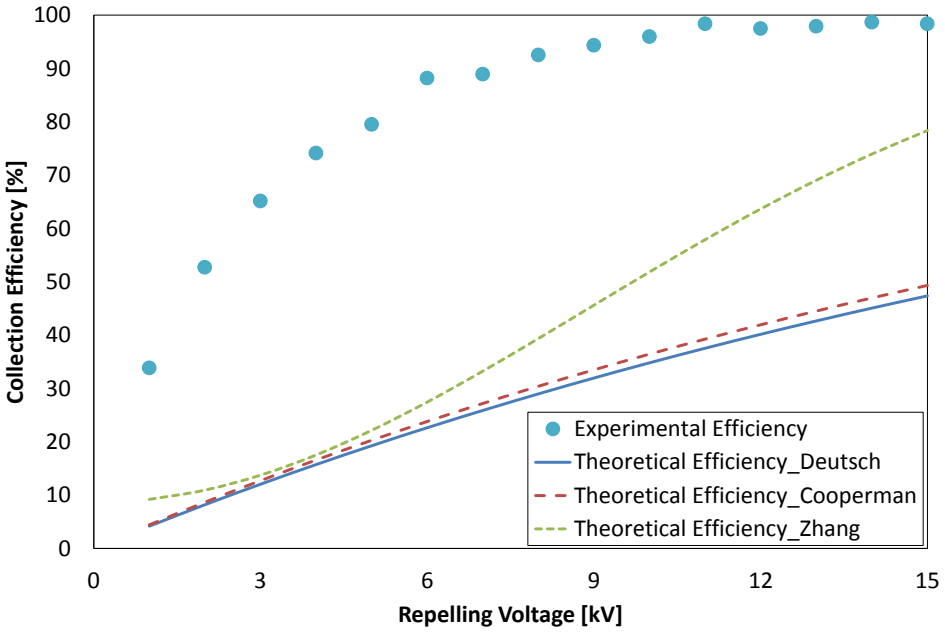

Figure 3.13: The collection efficiencies at different repelling voltages. The particle diameter is 0.3 µm. The airflow velocity is 2.5 m/s. The corona voltage is 5 kV.

Since the repelling electrode does not consume power, the repelling voltage can be as high as possible, as long as there is no spark discharge. In this case, no spark discharge was observed at 18 kV repelling voltage. Furthermore, Figure 3.13 shows that a high repelling

voltage results in a high collection efficiency. The collection efficiency of the ESP under test reaches 98% when the repelling voltage reaches approximately 11 kV. Further increases in the repelling voltage do not significantly improve the collection efficiency, but increases the chances of spark discharge.

3.4 Third Party Test

3.4.1 Test Conditions

Third party test is conducted by Research Triangle Institute (RTI) International, which is a nonprofit organization that provides technical and research services. The test conditions follow the ASHRAE 52.2 standard. The temperature is 75 F, the relative humidity is 44%, the test aerosol type is dry and solid-phase potassium chloride (KCl) that has 4.64 dielectric constant, and each dust loading is five grams. The brand and model of the particle counter used in the measurements is Climet 500 Spectrometer, covering the particle size range from 0.3 µm to 10 µm in 12 particle sizing channels.

3.4.2 Test Results

3.4.2.1 Collection Efficiency

The collection efficiencies are measured at 5 kV corona voltage (14.4 W corona power), 15 kV repelling voltage, and 2.5 m/s airflow velocity. Figure 3.14 shows the collection efficiencies for different particle sizes, along with the predicted collection efficiencies using Deutsch's, Cooperman's, and Zhang's equation of collection efficiency.

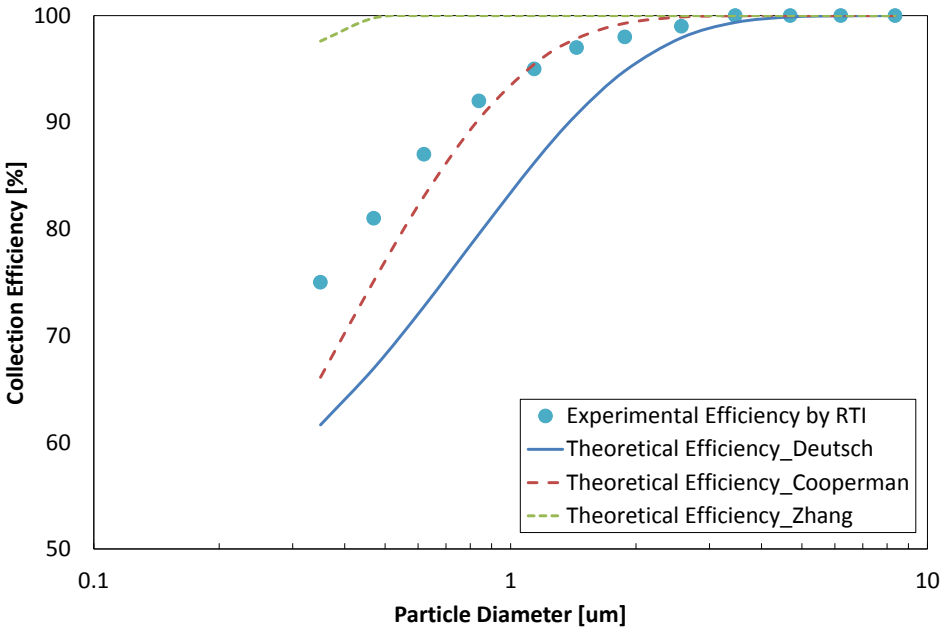

Figure 3.14: The collection efficiencies for different particle sizes. The corona voltage is 5 kV, the repelling voltage is 15 kV, and the airflow velocity is 2.5 m/s.

The experimental data shows a very good agreement with the predictions, especially for large particles. The collection efficiencies for large particles are significantly higher than those for small particles. For those particles smaller than one micron, one of the reasons that the experimental data shows an improvement over the predictions is that the foam helps in capturing fine particles. Note that, for 0.3 µm particles, the collection efficiency measured in-house is much higher than RTI's. This is due to the fact that the results shown in Figure 3.14 are conducted using five grams KCl particles, while the results shown in Figure 3.12 and Figure 3.13 are conducted in a normal laboratory environment which has a much lower particle concentration.

3.4.2.2 Pressure Drop

At 2.5 m/s airflow velocity, the initial pressure drop of the foam-covered ESP under test is 0.003556 mH_2O (34.9 Pa). After five dust loadings, the pressure drop of the foam-covered ESP is 0.003302 mH_2O (32.4 Pa). The pressure drop even decreases a little bit after several dust loadings. This shows that the pressure drop of ESPs does not change much over time or dust loading.

It is worth noting that the pressure drop varies significantly with airflow velocity: higher airflow velocity results in larger pressure drop. Figure 3.15 and Figure 3.16 show the pressure drop in terms of accumulated dust loading and the airflow velocity, respectively.

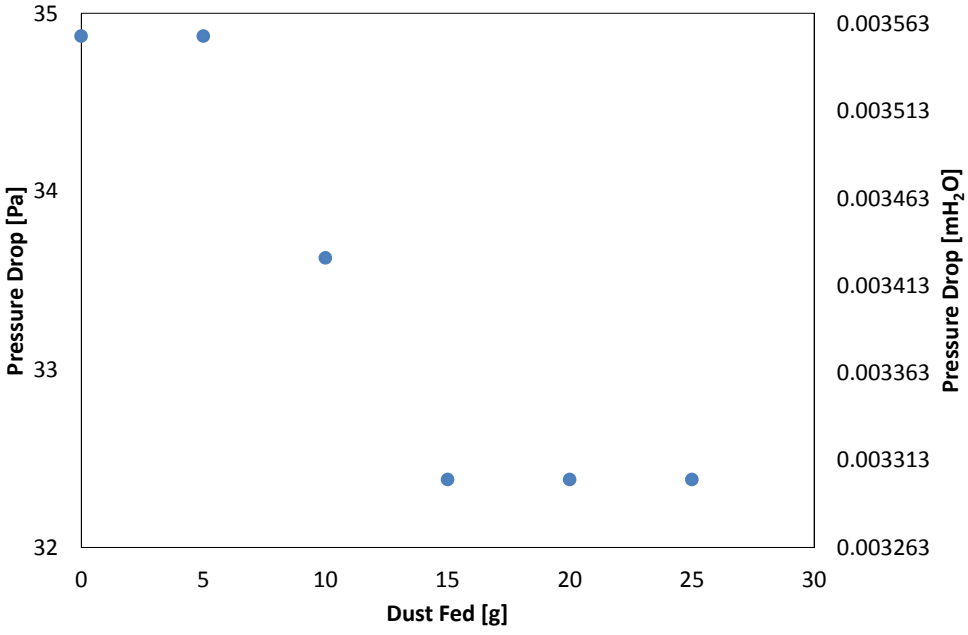

Figure 3.15: The pressure drop at accumulated dust loading. The airflow velocity is 2.5 m/s.

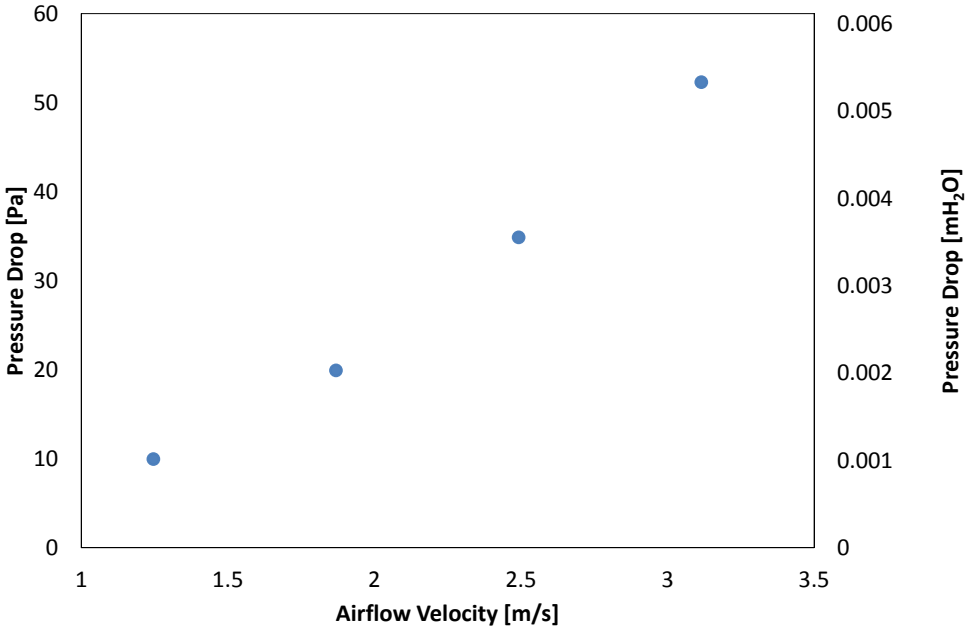

Figure 3.16: The relation between the pressure drop and airflow velocity at a clean condition.

3.4.2.3 Ozone Emission

RTI also conducts a test of ozone emissions. The results indicate that when the corona voltage is 5 kV and the ozone concentration upstream this particular foam-covered ESP prototype is 3 ppb (background), the ozone concentration downstream this particular foam-covered ESP prototype is 20 ppb. However, the ozone concentration increases up to 31 ppb over time, but stays unchanged after that. This ozone concentration falls far behind the regulations set by EPA, which is 75 ppb, and CDC, which is 100 ppb, as described in Chapter 1.

3.5 Parametric Study of Operating Conditions

3.5.1 Design of Experiments

As shown in the previous section, the collection efficiency is directly dependent on the particle migration velocity, which is determined by the electrostatic force and the drag force. The electrostatic force is induced by the electric field exist between the repelling and collecting electrodes, and the drag force is the force due to the movement of the particles in the air stream. Additionally, the particle size also influences the collection efficiency. A not well charged particle is unlikely to be collected by the collecting electrode. Furthermore, it has been demonstrated that the corona and repelling voltages have a significant influence on the collection efficiency.

To conclude, the parameters of interest are the corona voltage (charge level), the repelling voltage (electrostatic force), and the airflow velocity (drag force). Table 3.2 shows the levels for each parameter of interest.

Table 3.2: Parameters of interest and corresponding levels.

Parameter	Level 1	Level 2	Level 3	Level 4	Level 5
Airflow Velocity (m/s)	0.5	1.0	1.5	2.0	2.5
Corona Voltage (kV)	4	4.25	4.5	N/A	N/A
Repelling Voltage (kV)	6	9	12	15	18

3.5.2 Collection Efficiency

Figure 3.17, Figure 3.18, and Figure 3.19 show the contour plots of the collection efficiency, and (3.19), (3.20), and (3.21) give the corresponding quantitative equations, for the particle sizes that are centered around 0.3 µm, 0.5 µm, and 0.7 µm, respectively. Note that the variables shown in (3.19), (3.20), and (3.21) are coded, meaning that the maximum and minimum values are +1 and -1, corresponding to the maximum and minimum levels shown in Table 3.2, respectively.

$$\begin{aligned}\eta_{0.3um} =& 65.05 - 15.45A + 6.30B + 12.67C - 4.81A^2 - 1.51B^2 - 2.78C^2 \\ &+ 5.42AB + 10.49AC - 1.40BC\end{aligned} \tag{3.19}$$

$$\begin{aligned}\eta_{0.5um} =& 70.75 - 11.78A + 6.98B + 12.74C - 6.75A^2 - 1.98B^2 - 3.37C^2 \\ &+ 7.47AB + 11.95AC - 3.49BC\end{aligned} \tag{3.20}$$

$$\begin{aligned}\eta_{0.7um} =& 77.95 - 12.13A + 6.90B + 11.97C - 10.49A^2 - 1.63B^2 - 4.83C^2 \\ &+ 8.16AB + 13.17AC - 4.34BC\end{aligned} \tag{3.21}$$

where A is airflow velocity, B is corona voltage, and C is repelling voltage.

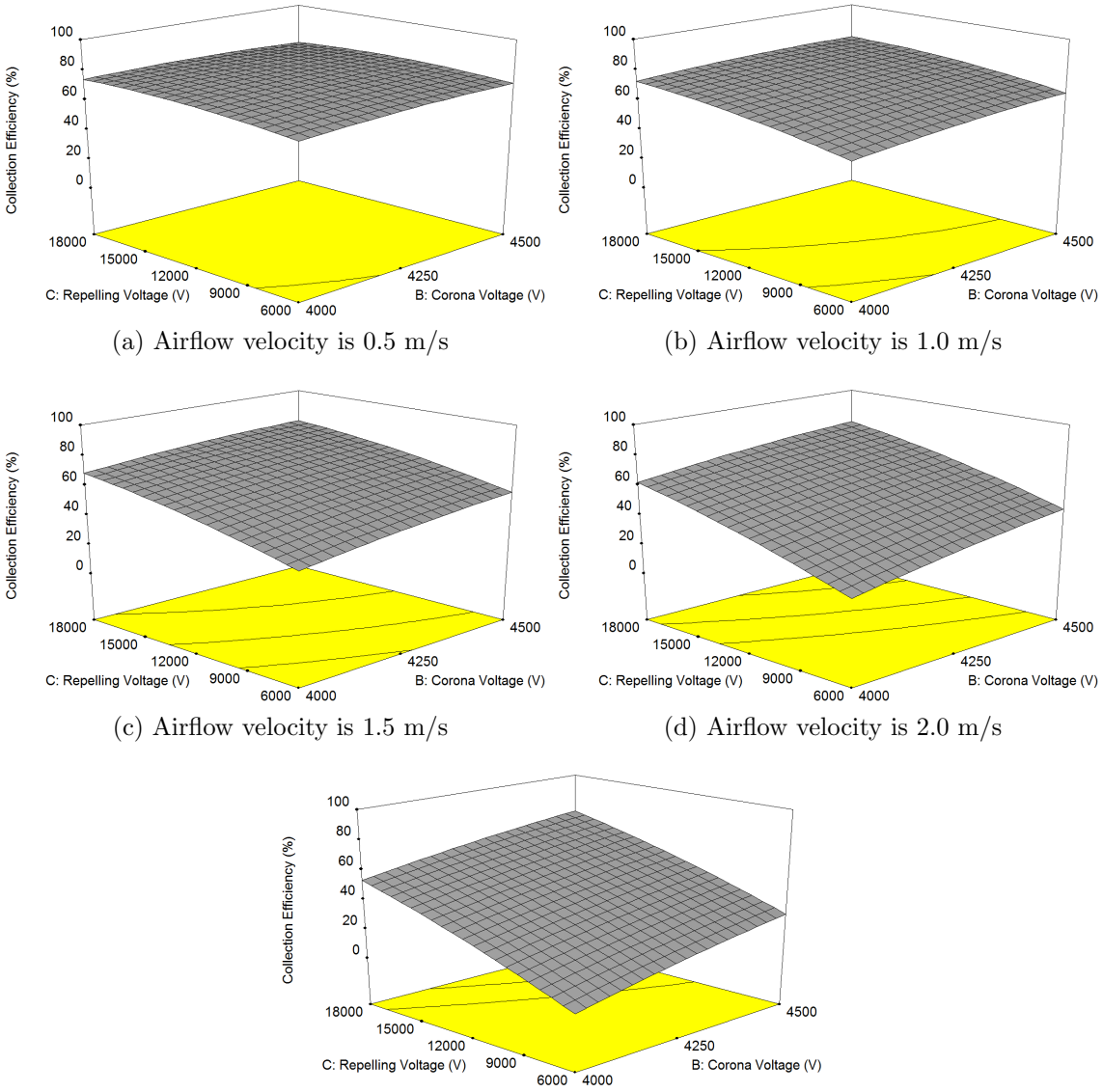

(a) Airflow velocity is 0.5 m/s

(b) Airflow velocity is 1.0 m/s

(c) Airflow velocity is 1.5 m/s

(d) Airflow velocity is 2.0 m/s

(e) Airflow velocity is 2.5 m/s

Figure 3.17: The collection efficiency versus the corona voltage, the repelling voltage, and the airflow velocity. The particle size is 0.3 µm.

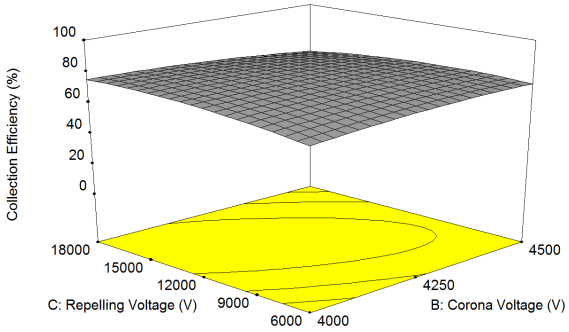

(a) Airflow velocity is 0.5 m/s

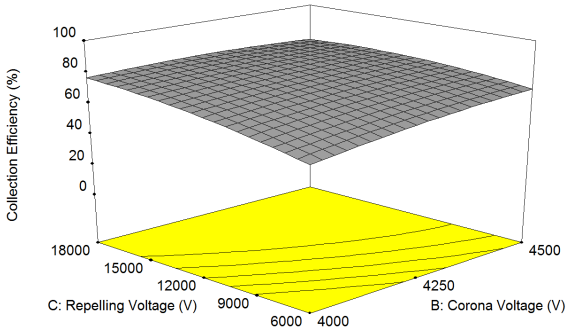

(b) Airflow velocity is 1.0 m/s

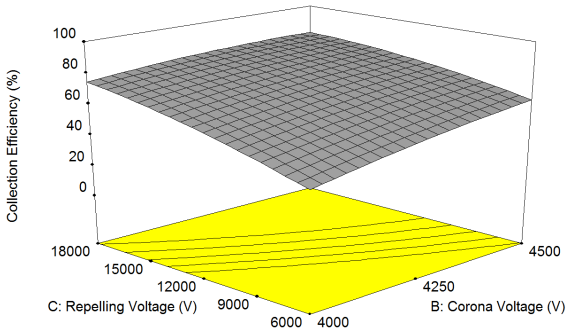

(c) Airflow velocity is 1.5 m/s

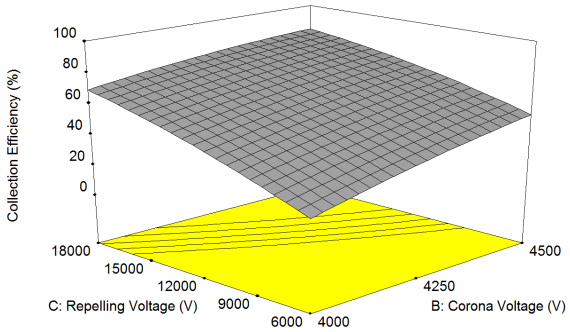

(d) Airflow velocity is 2.0 m/s

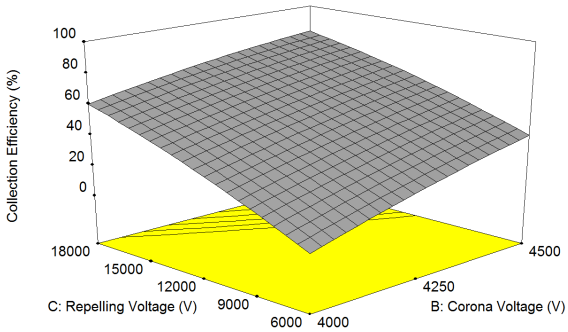

(e) Airflow velocity is 2.5 m/s

Figure 3.18: The collection efficiency versus the corona voltage, the repelling voltage, and the airflow velocity. The particle size is 0.5 µm.

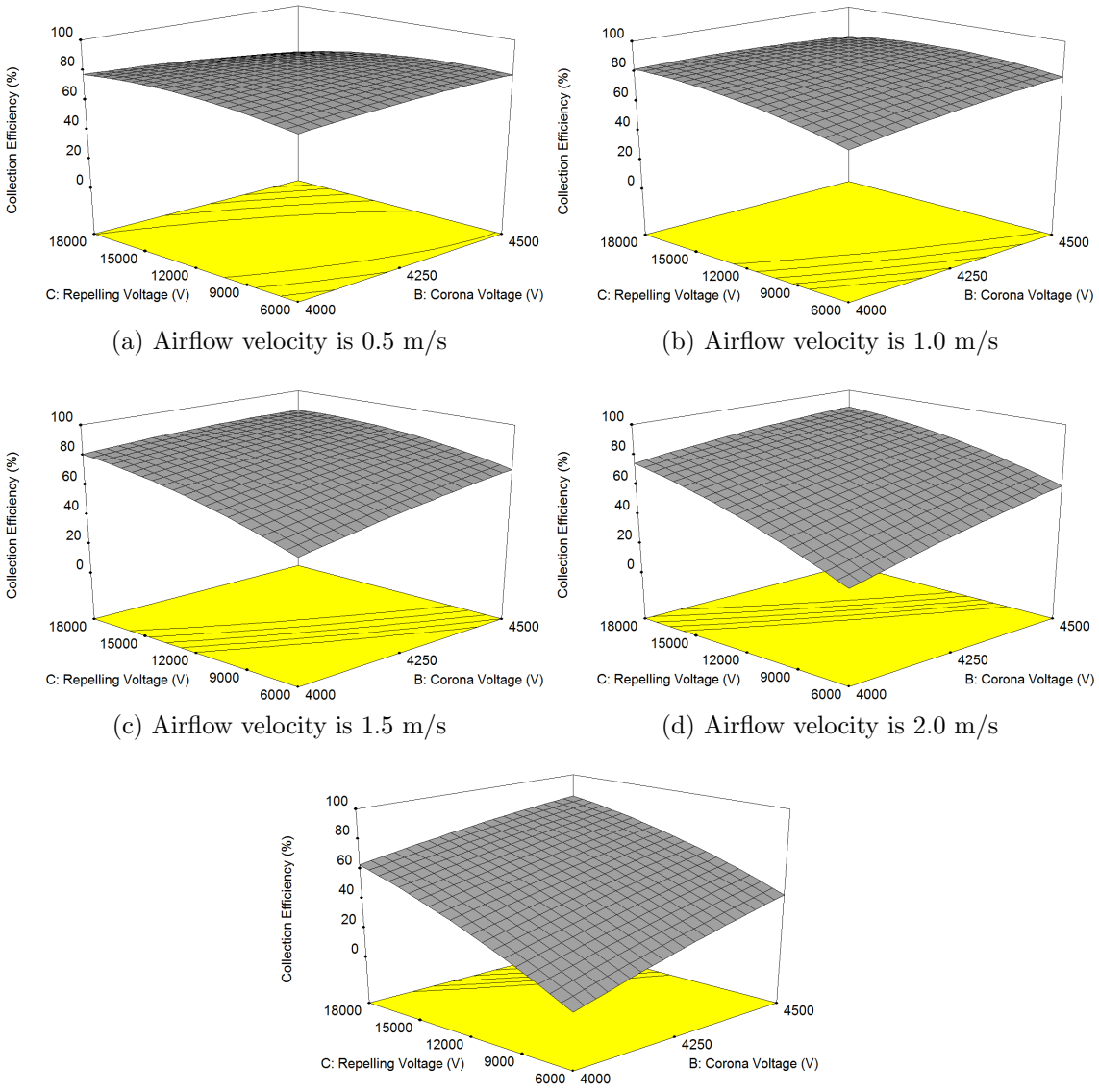

(a) Airflow velocity is 0.5 m/s

(b) Airflow velocity is 1.0 m/s

(c) Airflow velocity is 1.5 m/s

(d) Airflow velocity is 2.0 m/s

(e) Airflow velocity is 2.5 m/s

Figure 3.19: The collection efficiency versus the corona voltage, the repelling voltage, and the airflow velocity. The particle size is 0.7 µm.

The coefficients shown in (3.19), (3.20), and (3.21) are obtained by the regression analysis to the results using the quadratic model. The coefficients of coded variables are proportional to the observed effect (collection efficiency). The airflow velocity dominates the collection

efficiency, where one can see that the coefficient of A is higher than the others. One can use these equations to find a specific collection efficiency by directly substituting the coded values of each parameter of interest to the corresponding equation.

For 0.3 µm particles, as shown in Figure 3.17, the collection efficiency is high when the airflow velocity is low. For example, the collection efficiency shown in Figure 3.17(a) is generally higher than that shown in Figure 3.17(e). It makes sense because the particles settle down closer to the inlet when the airflow velocity is low. On the other hand, when the airflow velocity is low, the corona voltage and the repelling voltage do not affect the collection efficiency as much as they do at high airflow velocities. For example, Figure 3.17(a) is more flat than Figure 3.17(e). Low corona voltages with low repelling voltages result in low collection efficiencies. This is typically true, especially when the airflow velocity is high. Similar trends are observed for large particles, as shown in Figure 3.18 and Figure 3.19.

Through the analysis, higher corona and repelling voltages with lower airflow velocities generally results in higher collection efficiencies. Nevertheless, a satisfactory collection efficiency does not necessarily occur at the extreme corona voltage, extreme repelling voltage, or extreme airflow velocity. In this case, the operating conditions that result in the best collection efficiency are: 1.5 m/s airflow velocity, 4.2 kV corona voltage, and 18 kV repelling voltage. A 1.5 m/s airflow velocity produces high collection efficiency, and no spark discharge was observed. A 4.2 kV corona voltage not only proper for a high collection efficiency, but also for the balance of the corona power. A 18 kV repelling voltage, the highest setting in

this case, is chosen because it does not consume power, and thus, one can apply a voltage as reasonably high as possible to the repelling electrode, as long as no sparkover occurs.

When the airflow velocity decreased and the corona voltage increased, spark discharge occurred more often. This is because there is also an electric field between the corona and exciting electrodes. If the airflow velocity is not high enough, the ionized particles or molecules can follow the electric field between the corona and exciting electrodes instead of the flow field. Thus, those ionized particles or molecules can easily and directly go to the exciting electrodes to form a sparkover. However, as long as the airflow velocity is high enough, sparkover is nearly nonexistent.

3.6 Key Energy Performance

3.6.1 Metric of Energy Performance

An air filter must have a balanced performance of collection efficiency and energy efficiency to meet air quality standards and to satisfy the global demand for energy conservation, respectively. The Darcy's Law states that the performance of a filter media can be expressed by the penetration probability of particles and the pressure drop across the filter media at given flow rates and process conditions [133]. The ratio of the permeability to the pressure drop of the filter is a direct measure for the operating performance of the filter [133]. Equation (3.22) and (3.23) show the key energy performance of air filters [134-136] that was proposed to evaluate the performance of air filters in association with both collection efficiency and energy consumption (in the form of pressure drop). Table 3.3 shows five classifications of

key energy performance [136].

$$kep = \frac{-100 \times \log\left(1 - \eta_{filter}\right)}{\Delta P_{ave} - c} \tag{3.22}$$

$$\Delta P_{ave} = \frac{1}{M} \int_0^M \Delta P_{ave}\left(m\right) dm \tag{3.23}$$

where kep is key energy performance, η_{filter} is the average collection efficiency of the EN779 test with 0.4 µm particles at 0.94 m^3/s, ΔP_{ave} is the average pressure drop across the filter, c is an experimental constant (zero in this case), M is dust loading, and m is a variable of loaded dust.

Table 3.3: Classifications of key energy performance.

KEP	Energy Efficiency Class
$1 \leq kep$	1
$0.8 \leq kep < 1$	2
$0.7 \leq kep < 0.8$	3
$0.6 \leq kep < 0.7$	4
$kep < 0.6$	5

The key energy performance is dependent on the collection efficiencies and pressure drop of the filters. The collection efficiencies of both fiber-based filters and electrostatic precipitators worsen over time. Nonetheless, only the pressure drop of fiber-based filters deteriorates

over time because of the dust accumulation, whereas the pressure drop of electrostatic precipitators is independent from the dust loading as shown in 3.4.2.2. To prevent significant overestimation or underestimation, the average (initial and final) pressure drop for fiber-based filters is used in evaluating the key energy performance. Additionally, instead of the EN779 test, the collection efficiencies of the filters used here are adopted either from the literature or from the manufacturer's data sheets, and this data is based on clean initial conditions. The key energy performance would be different with dirty initial conditions.

3.6.2 Key Energy Performance of Fiber-Based Filters and Electrostatic Precipitators

In this section, the key energy performance of a commercially available fiber-based filter (3M E133, MERV 12, with electret fibers), a commercially available electrostatic precipitator (Aprilaire 5000, with a MERV 10 post-filter), and a foam-covered electrostatic precipitator are compared. At the airflow velocity of 2.5 m/s, the pressure drops across the 3M E133, Aprilaire 5000, and FC-ESP are 220.5 Pa, 54.8 Pa, and 32.4 Pa, respectively. The collection efficiencies for 0.3 µm particles for these three filters are 88.0%, 99.0%, and 99.0% [3], respectively. The key energy performance can then be calculated by using (3.22), and the results are shown in Table 3.4.

Table 3.4: The key energy performance of the 3M E133, Aprilaire 5000, and FC-ESP.

	Collection Efficiency (%)	Pressure Drop (Pa)	Key Energy Performance
3M E133 (Fiber-based)	88	220.5	0.4
Aprilaire 5000 (ESP)	99	54.8	3.6
Foam-covered ESP (ESP)	99	32.4	6.2

Although Aprilaire 5000 uses post-filters to improve collection efficiency, its key energy performance is still higher than that of 3M E133 because Aprilaire 5000 has a much lower pressure drop than 3M E133. Moreover, the key energy performance of FC-ESP is much higher than both other filters. Thus, at a specific airflow velocity and the same level of collection efficiency, using electrostatic precipitators in a filtration system is more energy efficient than using fiber-based filters.

3.6.3 Parametric Study for Key Energy Performance of Foam-Covered Electrostatic Precipitators

Since ESPs are active filters, the collection efficiency varies with factors such as corona voltage and repelling voltage, as shown and discussed in 3.3.2. The key energy performance of ESPs thus varies with such factors. Equation (3.22) shows that only the pressure drop is taken into account, while the actual corona power is not accounted for. However, the corona power does affect the collection efficiency of FC-ESP. So it is interesting to know how the corona voltage (corona power) and the repelling voltage affect the key energy performance

of FC-ESP. The testing conditions are 0.3 µm particle diameter and 2.5 m/s airflow velocity (32.4 Pa pressure drop).

3.6.3.1 Excluding Corona Power of Foam-Covered Electrostatic Precipitator

Excluding the corona power of FC-ESP, Figure 3.20 and Figure 3.21 show the key energy performance of FC-ESP with various corona voltages and repelling voltages, respectively.

Figure 3.20 shows that the key energy performance ranges from two to six. Comparing with the results shown in Table 3.4, FC-ESP still has significant higher key energy performance than 3M E133. As mentioned in 3.3.2.3, most of particles are not well-charged at 4 kV corona voltage, resulting a lower collection efficiency. However, once the collection efficiency is improved at 4.1 kV corona voltage or higher, the key energy performance of FC-ESP turns to be higher than that of Aprilaire 5000.

Similarly, from Figure 3.21, as long as the collection efficiency reaches a certain level, the key energy performance of FC-ESP is higher that of Aprilaire 5000 and way higher than that of 3M E133.

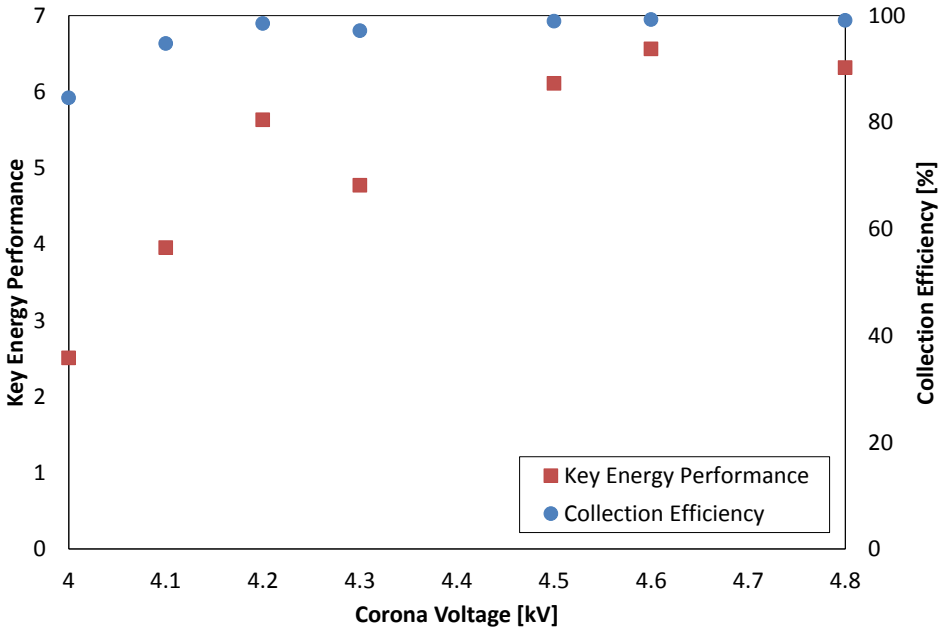

Figure 3.20: The key energy performance of the FC-ESP with different corona voltages. The repelling voltage is 15 kV. The corona power is excluded.

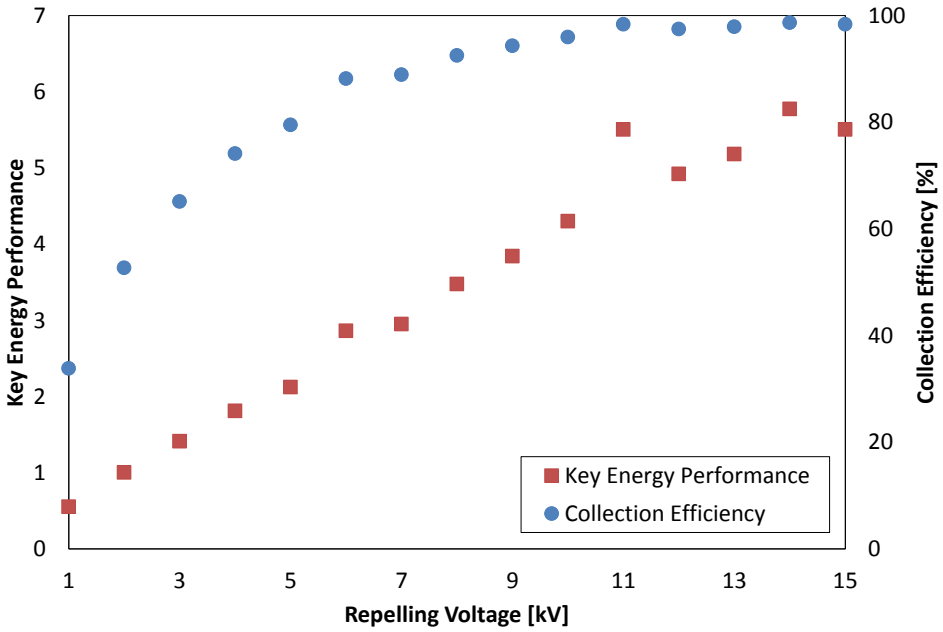

Figure 3.21: The key energy performance of the FC-ESP with different repelling voltages. The corona voltage is 5 kV. The corona power is excluded.

3.6.3.2 Including Corona Power of Foam-Covered Electrostatic Precipitator

Equation (3.22) ignores the actual corona power. This might overestimate the key energy performance for active filters such as ESPs, because active filters do consume power. To eliminate this overestimation, the traditional power-pressure-flow rate equation is used to convert the electric power to the effective pressure drop.

$$\Delta P_{eff} = \frac{W \times \eta_{system}}{Q} \tag{3.24}$$

where ΔP_{eff} is effective system pressure drop, W is system power consumption (corona power plus pump power), Q is volumetric airflow rate, and η_{system} is the energy efficiency of the system.

Assuming a fully power-pressure conversion and assuming the energy efficiency of the system is one, the effective pressure drop can be obtained by electric power over volumetric flow rate. Summing up this effective pressure drop and the "physical" pressure drop (32.4 Pa), Figure 3.22 and Figure 3.23 show the key energy performance of FC-ESP with various corona voltages and repelling voltages, respectively.

Looking at Figure 3.22, it is not a surprise that the key energy performance of FC-ESP hits the highest point at 4.2 kV corona voltage. This is because further increase in corona voltage beyond 4.2 kV does not significantly increase the collection efficiency but corona power, as discussed in 3.3.2.3. The key energy performance shown in Figure 3.22 is lower than those shown in Figure 3.20 because the corona power is taken into account.

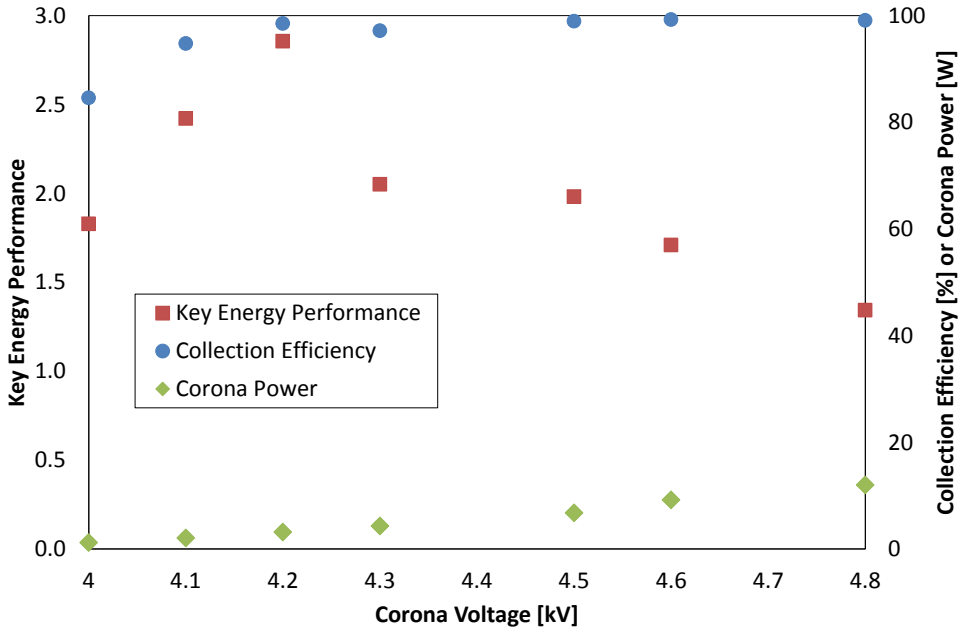

Figure 3.22: The key energy performance of FC-ESP with different corona voltages. The repelling voltage is 15 kV. The corona power of FC-ESP is included.

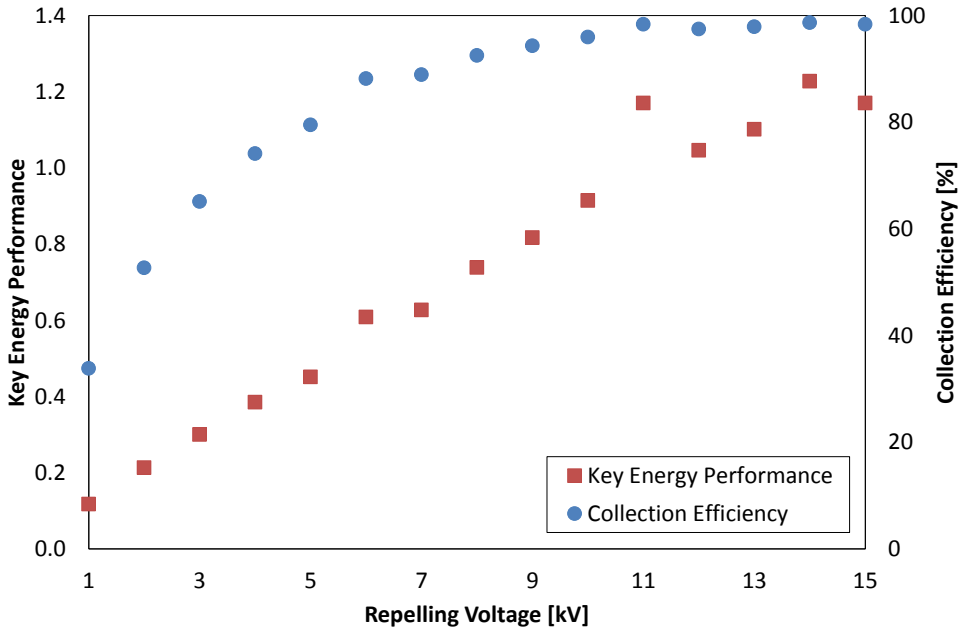

Figure 3.23: The key energy performance of FC-ESP with different repelling voltages. The corona voltage is 5 kV. The corona power of FC-ESP is included.

As for the effect of the repelling voltage, the trend of the key energy performance shown in Figure 3.23 is exactly identical with that shown in Figure 3.21, except the absolute values of the key energy performance shown in Figure 3.23 are lower than those shown in Figure 3.21.

3.7 Energy Savings of Replacing Fiber-Based Filters with Foam-Covered Electrostatic Precipitators

3.7.1 Operational Cost per Airflow

The cost of operating a filtration system varies with several factors, including the cost of filters, the cost of energy and labor, and the operating conditions and environments. The cost per unit of airflow can be expressed as [137],

$$C_{unitflow} = \frac{C_{filter} + C_{labor} + C_{energy}}{L_{filter} \times Q} \tag{3.25}$$

where $C_{unitflow}$ is the cost per unit of airflow, C_{filter} is the cost of filters, C_{labor} is the labor cost of filter installation, C_{energy} is energy cost, L_{filter} is the lifetime of filter, and Q is volumetric airflow rate. The energy cost can be calculated using the product of the brake horsepower, the operation time, and the retail price of electricity, as shown in (3.26) and (3.27) [138].

$$C_{energy} = BHp \times T \times C_{retail} \tag{3.26}$$

$$BHp = \frac{Q}{0.0763} \times \frac{\Delta p}{\eta_{\ system}} \times 0.746 \tag{3.27}$$

where BHp is brake horsepower, T is operation time per year, C_{retail} is the retail price of electricity, Δp is pressure drop, and η_{system} is the efficiency of the system.

3.7.2 Energy Savings in Loew Hall

A real-life example is presented in the next part of this section. The Loew Hall at the University of Washington is a multifunctional building with 5,295 square meters of floor area. The current HVAC system, as shown in Figure 1.1, was designed by using a tubular centrifugal pump to bring air into and out of the system at an airflow rate of 26.5 m^3/s and a pressure drop of 0.1 mH_2O. The system energy efficiency is assumed to be 0.7, and the operation time is assumed to be 3,650 hours a year (10 hours per day).

Currently, there are 35 fiber-based filters (Purolator SERVA-PAK 24x24x22, MERV 13) installed. According to the manual of facility maintenance, the lifetime and costs of these Purolator filters are three years and $50 (labor included), respectively. The initial pressure drop of the Purolator filters is 0.014 mH_2O at 2.5 m/s face velocity. The recommended final pressure drop is 0.038 mH_2O, resulting in a 0.026 mH_2O average pressure drop. Again, because the pressure drop of a fiber-based filter increases with time, to prevent over/under estimation, the average pressure drop is used to evaluate the brake horsepower. Thus, for the current HVAC system in Loew Hall, the pressure drop of the components other than the Purolator filters is 0.074 mH_2O. The pressure drop of the FC-ESP is 0.003 mH_2O, and

assuming it stays unchanged over time. Thus the tubular centrifugal pump only needs to overcome a system pressure drop of 0.077 mH_2O when replacing current Purolator filters with FC-ESPs.

The investment of building a brand new FC-ESP from scratch totals $150 USD. Regarding FC-ESP's maintenance costs, assuming the plate electrodes do not significantly deteriorate over the years, the corona wires and foam are the only two parts that need to be periodically cleaned or replaced. According to the user manual for the Aprilaire 5000, the suggested maintenance period is six months and it offers five years of warranty. Such existing technology allows us to assume a "six month" maintenance frequency and a "five year" working lifetime. For the replacement of a single FC-ESP, the five-year-cost of the corona wire is $1.4 USD/m) and the cost of the foam is $0.4 USD/$m^2$). Therefore, the assumption of the $200 USD unit cost for a FC-ESP with a five year lifetime is fairly reasonable. Table 3.5 shows the comparisons of the energy cost per unit airflow between operating the Purolator fiber-based filters and operating the foam-covered electrostatic precipitators in Loew Hall.

The combined cost of the filters and labor involved in using foam-covered electrostatic precipitators is higher than the cost incurred by using Purolator fiber-based filters. However, operating the foam-covered electrostatic precipitators in Loew Hall saves a significant amount of money in energy cost when compared to operating the Purolator fiber-based filters, due to the nature of low pressure drop across the foam-covered electrostatic precipitators. When the Purolator fiber-based filters are replaced with the foam-covered electrostatic precipitators, the estimated energy cost per unit airflow in the Loew Hall's HVAC system is reduced by

26.5%.

Table 3.5: Comparison of the energy cost per unit airflow using the Purolator fiber-based filters and the foam-covered electrostatic precipitators in Loew Hall.

Item	Fiber-based Filters	Foam-covered ESPs	Notes
System efficiency, η_{system}	0.7	0.7	
System pressure drop, Δp	0.100 mH_2O	0.077 mH_2O	
Airflow rate, Q	26.5 m^3/s	26.5 m^3/s	
Brake horsepower, BHp	37.0 kW	28.5 kW	Eq. (3.27)
Operation time, T	3,650 hrs/year	3,650 hrs/year	
Retail price of electricity, C_{retail}	\$0.0801/kWh	\$0.0801/kWh	WA State
Energy cost, C_{energy}	\$10,831	\$8,340	Eq. (3.26)
Unit cost (labor included)	\$50	\$200	
Cost of filters and labor, $C_{filter} + C_{labor}$	\$1,750	\$7,000	35 filters
Lifetime, L_{filter}	3 years	5 years	
Energy cost per unit airflow, $C_{unitflow}$	\$158	\$116	Eq. (3.25)

3.8 Summary

A prototype ESP with foam-covered collecting electrodes has been successfully built and demonstrated. FC-ESPs also have been experimentally proven to have a collection efficiency of up to 99% in an ordinary laboratory environment.

The corona voltage, the repelling voltage, and the free airflow velocity have significant influence on the collection efficiency of FC-ESPs. In general, high corona voltage and high repelling voltage result in high collection efficiency. However, when the collection efficiency

is around 99%, increasing the corona voltage further increases the corona power, but not the collection efficiency. Despite the repelling electrodes do not consume power, when the collection efficiency is close 99%, increasing the repelling voltage further increases the chances of spark discharge. On the other hand, the highest collection efficiency is not necessarily to be at the most extreme airflow velocities. A moderate airflow velocity is desirable, because an extremely low airflow velocity increases the chance for spark discharge in the charger, whereas a high airflow velocity causes particles to be blown out of the channel without being captured by the collecting electrodes. Three theoretical equations of collection efficiency are used compared with the experimental data, and the results show a good agreement with to each other.

Third party test conducted by RTI also shows that FC-ESPs have exceptional collection efficiencies across a full range of particle sizes under harsh test conditions that follow ASHRAE 52.2 standard. The results suggest that the pressure drop of FC-ESP is affected by only the free airflow velocity, but not dust loading. This fact provides a great evidence that using foam-covered electrostatic precipitators in an HVAC system is more economically beneficial when compared to using fiber-based filters. The concentration of the ozone emission, on the other hand, is below both government and industrial standards.

Regarding the energy efficiency, the results show that electrostatic precipitators have significantly higher key energy performance than fiber-based filters because the pressure drop across electrostatic precipitators is much lower than that across fiber-based filters. When particles are well-charged and repelling voltage is moderately high, the key energy perfor-

mance of the foam-covered electrostatic precipitators is higher than that of its commercial counterparts and way higher than that of the fiber-based filters. A down-to-the-earth example, the HVAC system in Loew Hall at the University of Washington, shows that using FC-ESPs to replace current Purolator (fiber-based) filters saves 26.5% energy supplied to the pumps that are used for circulating air.

Chapter 4

GUIDANCE-PLATE-COVERED ELECTROSTATIC PRECIPITATORS

The idea of trapping particles in secured spaces has been proven to be effective in achieving high collection efficiency for ESPs, as discussed in Chapter 3. To explore other particle-trapping mechanisms, this chapter presents and discusses the guidance-plate-covered (GPC) ESPs. GPC-ESPs use perforated guidance plates to cover the collecting electrodes, and gaps are intentionally left between the guidance plate and the collecting electrode to allow particles to enter through the holes and stay inside the gaps. GPC-ESPs are made of metal entirely and the gaps are able to accommodate a great amount of particles, thus GPC-ESPs are highly applicable in dusty areas without frequent replacement and maintenance.

4.1 Proof-of-Concept Prototype

4.1.1 Design Concept

Figure 4.1 and Figure 4.2 show the schematic of the GPC-ESP and the assembly diagram, respectively. The collecting electrodes are covered with guidance plates that have numbers of patterned holes. Rather than directly attaching the guidance plates to the collecting electrodes, gaps are intentionally left in-between them by using a spacer in the peripherals of the guidance plates.

The holes allow the particles to go through the guidance plates and stay in the gaps between the guidance plates and the collecting electrodes. Because the disturbance level inside these gaps is relatively low compared to that on the bare collecting electrode, the collected particles have lower chances of returning to the environment. Thus, this new type of ESP is highly applicable to areas with high amounts of aerosol particles, such as sandy shorelines, deserts, or diesel engines.

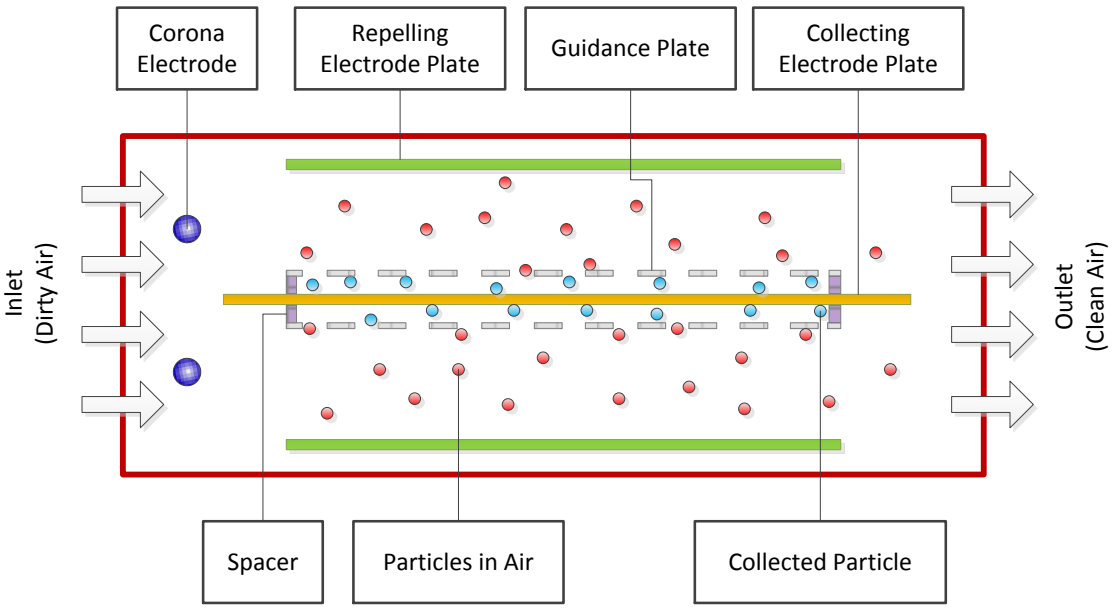

Figure 4.1: The schematic of the GPC-ESP. Not drawn to scale.

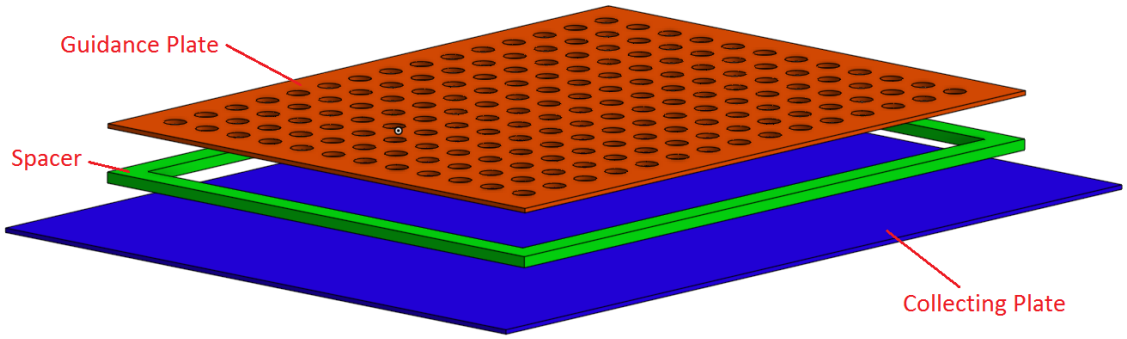

Figure 4.2: The assembly diagram of the GPC-ESP. Not drawn to scale.

4.1.2 Prototype Assembly

As shown in Figure 4.3, the cross-sectional area of the GPC-ESP prototype under test is 202 mm by 98 mm, and the width is 30 mm, excluding the enclosure. The main components of this prototype are,

1) 1 rigid plastic made enclosure

2) 2 Co-based alloy (35N LT) made corona electrodes (wire)

3) 2 aluminum made guidance plates (plate)

4) 1 aluminum made collecting electrodes (plate)

5) 2 aluminum made repelling electrodes (plate)

This is a two-channel prototype, each channel is 15 mm wide, and two corona electrodes are placed in the center of each channel. The collecting electrode is 30 mm longer than the repelling electrode, so that the spark discharge between the collecting electrode and the repelling electrodes is minimized and the pattern of the electric field is modified for higher collection efficiency. Both sides of the collecting electrode are covered with the guidance

plates, which have the same size as the repelling electrodes, by using 2 mm thick spacer in the peripheral of the guidance plates. The guidance plate has patterned holes that are drilled by an ordinary drilling machine. Table 4.1 gives more details about the dimensions of this baseline guidance plate. Figure 4.4 shows the working sample of the baseline guidance plate and Figure 4.5 shows a working prototype of GPC-ESP.

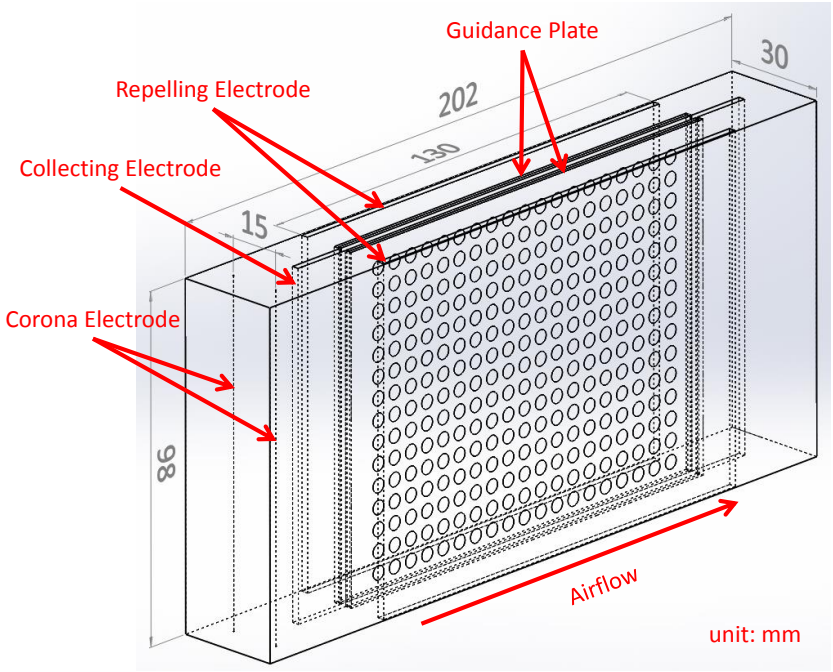

Figure 4.3: Dimensional information of the GPC-ESP under test. Drawn to scale.

The bare electrode (BE) ESP is a special case of GPC-ESP. BE-ESP has exactly the same geometric structure and physical dimensions as the GPC-ESP, except the "guidance plates" of the BE-ESP have no holes at all, as shown in Figure 4.6. The reason for purposely

making the BE-ESP the same as the GPC-ESP is to eliminate the geometric differences that have dramatic influences on the collection efficiency of the ESPs. Note that the guidance plates of the BE-ESP are grounded, and the guidance plates of the GPC-ESP float on the collecting electrode (i.e., no electrical connections at all).

Table 4.1: Physical dimensions of the baseline guidance plate.

Item	Value
Overall Dimension (mm)	130 by 98 by 0.81
Diameter of Holes (mm)	4
Number of Holes	128

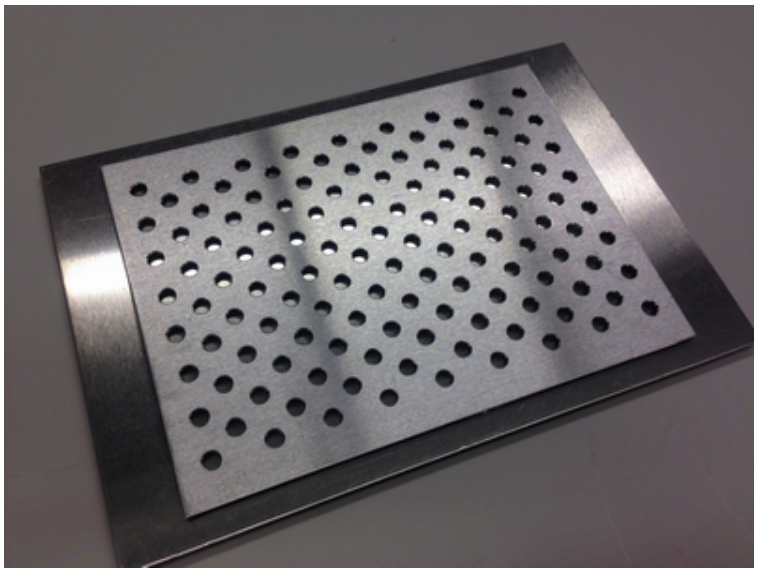

Figure 4.4: Baseline guidance plate.

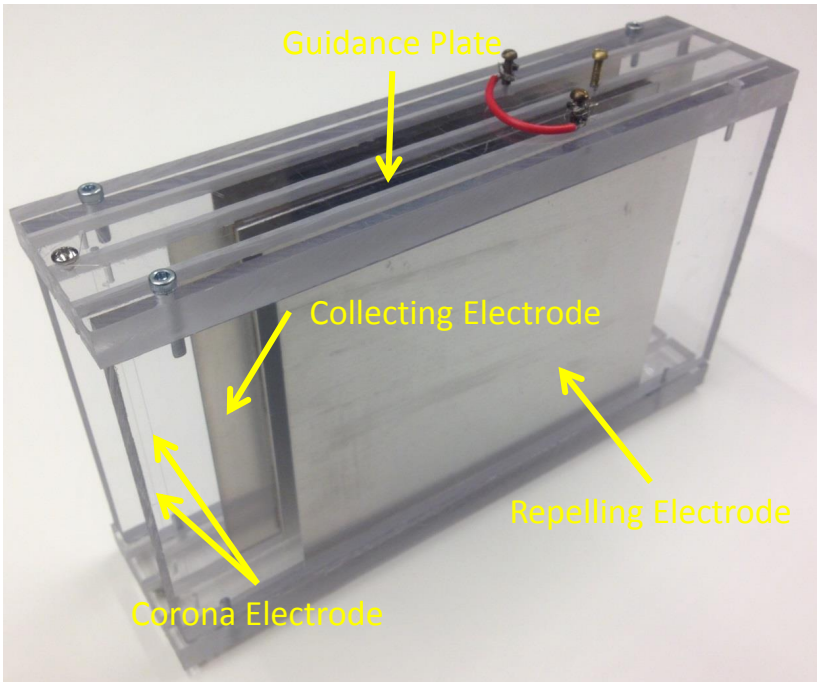

Figure 4.5: A working prototype of GPC- ESP.

Figure 4.6: Bare electrode, a "guidance plate" without any holes.

4.2 Experimental Setup

Figure 4.7 shows the schematic of the experimental setup. Air is drawn into the ESP under test using traditional rotary fans. The free airflow velocity is varied by adjusting the input

power to the fans. A particle counter (Haltech HPC600) is placed right after the ESP to measure the number of particles in the air. The minimum measurable particle size is 0.3 µm, and the particle counting efficiency is 100 ± 10% at 0.45 µm. A high voltage DC power supply (Hipotronics) provides high positive voltage to the corona electrodes, and a separate power supply (Spellman SL150) supplies high positive voltage to the repelling electrodes. The collecting electrode is grounded. Table 4.2 shows the operating parameters of interest, including free airflow velocity, corona voltage, and repelling voltage.

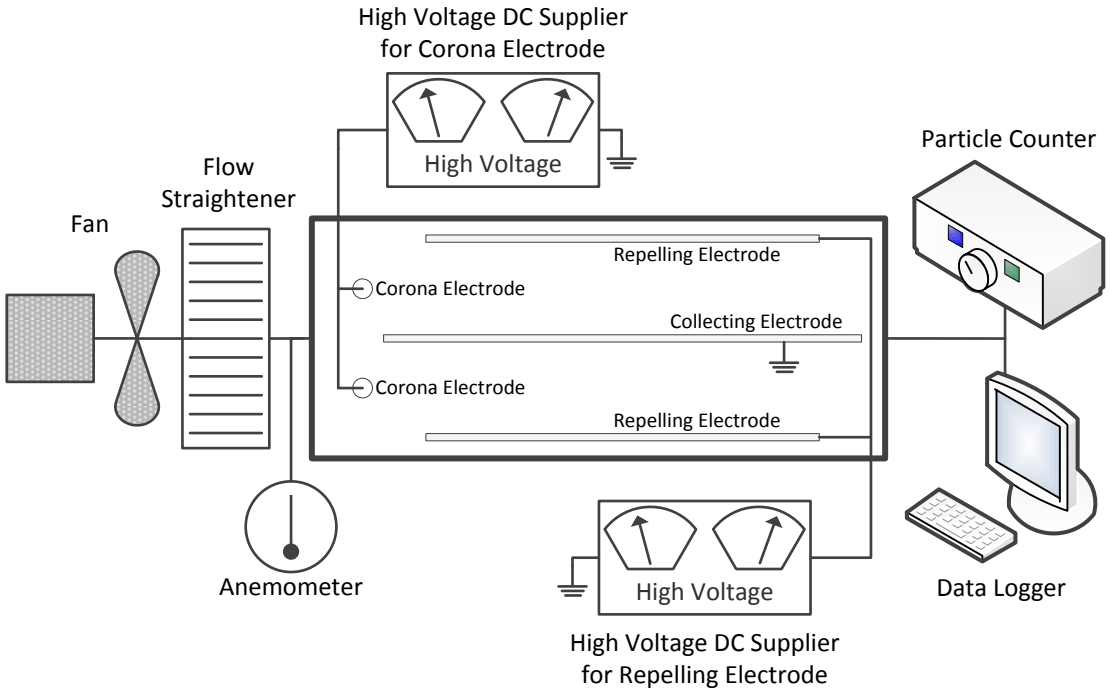

Figure 4.7: A schematic of the experimental setup, including the fans and the ESP under test (BE- or GPC-ESP). Not drawn to scale.

Table 4.2: Parameters and levels of interest.

Free Airflow Velocity (m/s)	Corona Voltage (kV)	Repelling Voltage (kV)
1.0	13.5	4
2.0	15.0	8
3.0	16.5	12

Note that a positive corona is used for the work presented in this dissertation, because the ESPs discussed through this dissertation aim to non-industrial applications. Positive corona produces less ozone [12, 129], operates quieter [40], and has lower corona power than negative corona.

4.3 Numerical Modeling

A two dimensional model of the collector of a GPC-ESP is built by using COMSOL Multiphysics v4.2, a commercial finite element analysis package. A few assumptions are made before performing the simulation. First, the particle concentration is assumed to be sufficiently low to neglect the hydrodynamic and electric interactions between particles and to neglect collisions and clustering [139]. Second, because there are only two corona electrodes in this specific ESP, the free airflow is presumed to be the dominant over the flow field and the ionic wind (also known as secondary flow) that exists in the charger is neglected. Third, particle re-entrainment and particle rebound are excluded in the baseline numerical model. A separate set of simulations is carried out to simulate particle re-entrainment in later this section. Fourth, the corona voltage is 16.5 kV and particles are assumed to be fully charged.

Fifth, the free airflow is assumed to be fully developed at the inlet.

4.3.1 Model Outline and Mesh

The numerical model of the collector of a GPC-ESP is built according to the black dashed rectangle shown in Figure 4.8, while Figure 4.9 gives the detail dimensions. Briefly, the simulation domain is 160 mm by 15 mm, the collecting electrode is 160 mm by 0.81 mm, the repelling electrode is 130 mm by 0.81 mm, the guidance plate is also 130 mm by 0.81 mm, and the gap height is 2 mm. The hole diameter shown in Figure 4.9 is 4 mm, though the hole diameter is one of the parameters of interest.

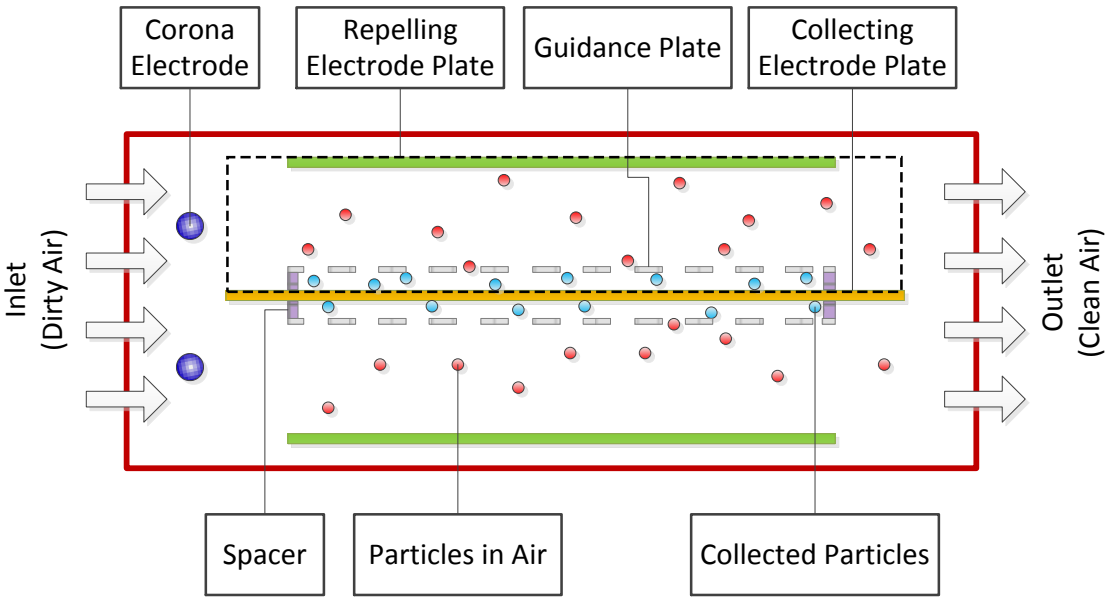

Figure 4.8: A schematic of GPC-ESP. The black dashed rectangle is the simulation domain. Not drawn to scale.

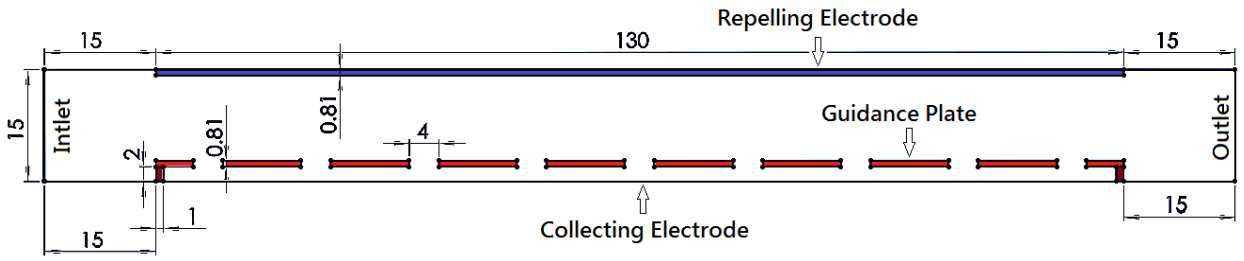

Figure 4.9: Dimensional information of the numerical model (collector only) of the GPC-ESP. Drawn to scale, the unit is mm.

There are about 14000 free-triangular elements and about 4000 boundary-layer elements around all fluid boundaries. Figure 4.10 shows the mesh density. From the element quality histogram and element quality map shown in Figure 4.11 and Figure 4.12 respectively, the minimum element quality is 0.07164 and the average element quality is 0.732 (the best quality is 1). Overall, the meshing quality is high and acceptable. Figure 4.12 shows that the regions that have lower element quality are the fluid boundaries because the aspect ratio of the elements in these regions is generally larger than that of other regions.

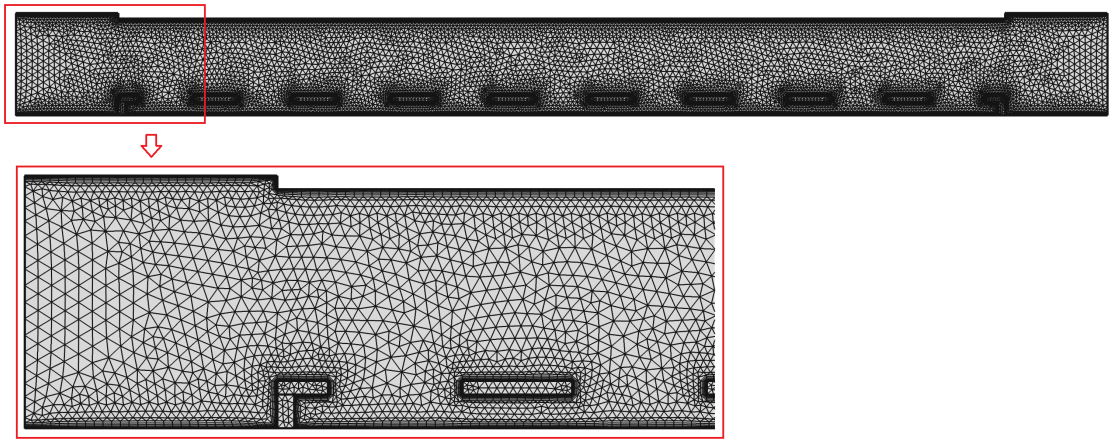

Figure 4.10: Meshing grids and density.

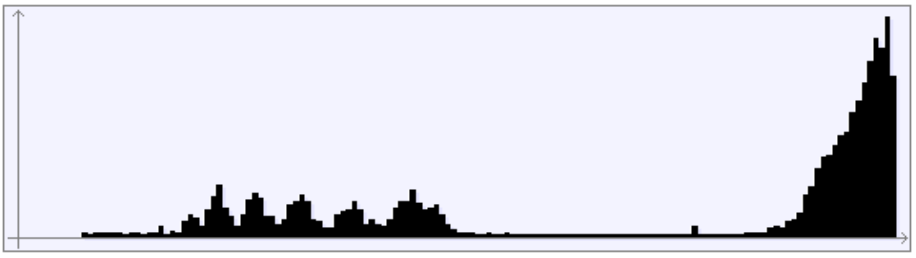

Figure 4.11: Element quality histogram.

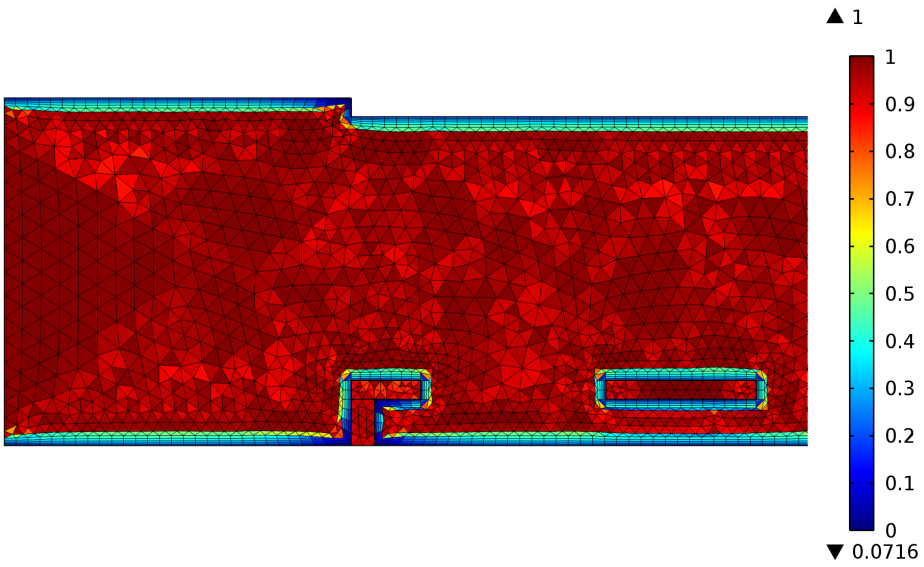

Figure 4.12: Element quality map.

4.3.2 Boundary Conditions

The boundary conditions and all constants, including turbulence model constants, used in the simulation are summarized in Table 4.3 and Table 4.4, respectively. The modules "Turbulent Flow", "Electrostatics", and "Particle Tracing for Fluid Flow" are used in this simulation.

The "Turbulent Flow" module, $k-\varepsilon$ RANS model, is used to simulate the flow velocity and pressure fields. Because of the fully developed assumption, the inlet is applied the free

airflow in the longitudinal direction, whereas the transverse velocity is set to zero. The outlet is set to be zero pressure. All other fluid boundaries are set to be no slip. The turbulent dispersion is excluded because the Reynolds numbers are fairly low and the particle size this dissertation concerns about are small enough so that the particle dispersion is identical with fluid diffusion [140, 141].

Table 4.3: Boundary conditions.

	Flow Field	Electric Field	Particle Transport
Inlet	$U_x = 1$, 2, or 3 m/s $U_y = 0$ m/s	$\partial V/\partial n = 0$	1000 particles
Outlet	No pressure	$\partial V/\partial n = 0$	Freeze
Repelling electrode	No slip	V=4, 8, or 12 kV	Freeze
Guidance plate	No slip	180 V	Freeze
Collecting electrode	No slip	Ground	Freeze

The "Electrostatics" module is used to simulate the electrical potential (voltage) field. High voltage is applied to the repelling electrodes and the collecting electrodes are grounded. Although the guidance plate is made out of metal and is electrically disconnected from the collecting plate, the accumulation of the charged particles results in about 180 volts on the guidance plate, despite the hole diameter and the repelling voltage. Neumann condition is specified at both inlet and outlet.

The "Particle Tracing for Fluid Flow" module is used to describe the particle trajectories

and to derive the collection efficiency by counting the number of particles at the outlet. The particles are subjected to drag forces and electrostatic forces, coming from the results of "Turbulent Flow" and "Electrostatics" modules, respectively. There are 1000 particles released uniformly across the inlet. Particles are assumed to be freeze at all flow walls.

Table 4.4: Constants used in the model.

Constant	Value
Particle diameter	0.3 µm
Particle mass density	2350 kg^1m^{-3}
Air temperature	303 K
Air dynamic viscosity	18.5×10^{-6} $N^1s^1m^{-2}$
Air density	1.18 kg^1m^{-3}
Permittivity of free space	8.85×10^{-12} F^1m^{-1}
Ion mobility	1.33×10^{-4} $m^2V^{-1}s^{-1}$
RMS thermal velocity of ions	240 m^1s^{-1}
Time constant of ion concentration	10^{13} $\#^1m^{-3}s^1$
Boltzmann's constant	1.38×10^{-23} J^1K^{-1}
Turbulent constant C_1	1.44
Turbulent constant C_2	1.92
Turbulent constant C_μ	0.09
Turbulent constant σ_k	1
Turbulent constant σ_ε	1.3
Turbulent constant κ_v	0.41
Turbulent constant B	5.2

4.3.3 Parameters of Interest

Based on the experimental settings, the parameters of interest in this simulation are hole diameter (2 mm, 4 mm, and 8 mm), airflow velocity (1 m/s, 2 m/s, and 3 m/s), and repelling voltage (4 kV, 8 kV, and 12 kV). The hole count is not applicable because this simulation is two-dimensional. In order to discuss the results using dimensionless quantities, Table 4.5 shows the relationships between the Stoke numbers, the electrostatic numbers, the free airflow velocities, and the repelling voltages.

Table 4.5: The Stoke numbers and the electrostatic numbers at corresponding airflow velocities and repelling voltages.

Repelling Voltage	Airflow Velocity		
	1 m/s	2 m/s	3 m/s
4 kV	Stk=0.000067	Stk=0.000130	Stk=0.000200
	Es=0.169	Es=0.085	Es=0.056
8 kV	Stk=0.000067	Stk=0.000130	Stk=0.000200
	Es=0.338	Es=0.169	Es=0.113
12 kV	Stk=0.000067	Stk=0.000130	Stk=0.000200
	Es=0.507	Es=0.254	Es=0.169

4.3.4 Flow Characteristics

Figure 4.13 shows several flow characteristics with different Stoke numbers and hole diameters. First, as long as the hole diameter is given, the patterns of both the mean velocity fields and mean flow streamlines stay identical even though the Stoke numbers are different. However, the magnitude of the velocity varies accordingly with the Stoke numbers. Second, the velocity magnitude in the gaps is very low, as expected, but it does increase when the hole diameter increases. The electrostatic force is higher than the inertial force in the gaps. Third, the recirculation exists in the first one or two holes and gets stronger when the Stoke number and the hole diameter increase. The recirculation region still exists in the following holes, but not as strong as it does in the first one or two holes. Another recirculation region exists immediately after the right spacer, and particles are expected to be collected in this region as well.

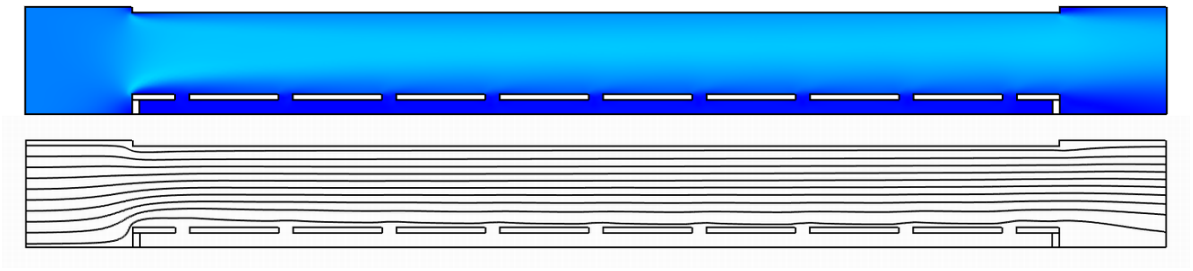

(a) the hole diameter is 2 mm, the Stoke number is 0.67×10^{-4}

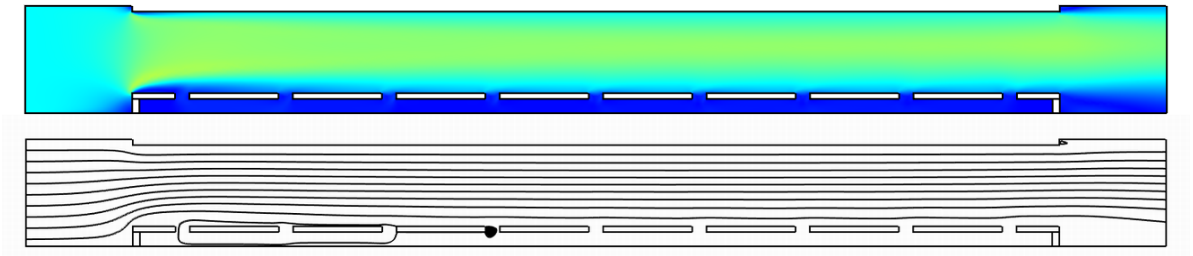

(b) the hole diameter is 2 mm, the Stoke number is 1.30×10^{-4}

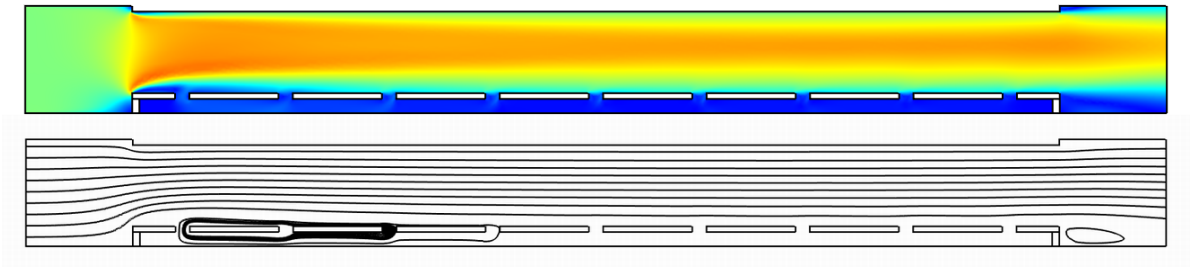

(c) the hole diameter is 2 mm, the Stoke number is 2.00×10^{-4}

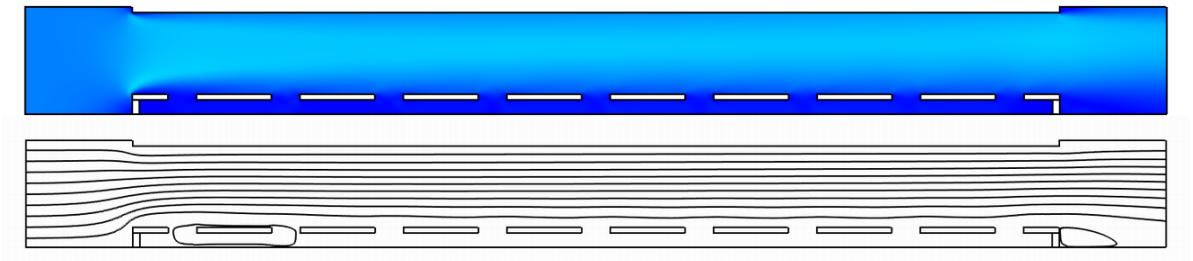

(d) the hole diameter is 4 mm, the Stoke number is 0.67×10^{-4}

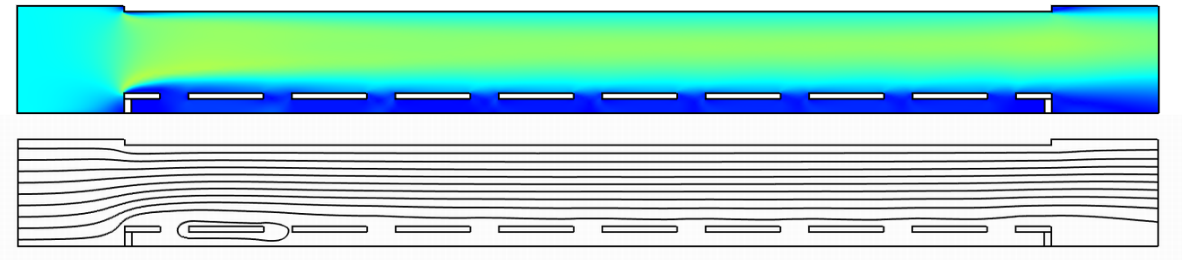

(e) the hole diameter is 4 mm, the Stoke number is 1.30×10^{-4}

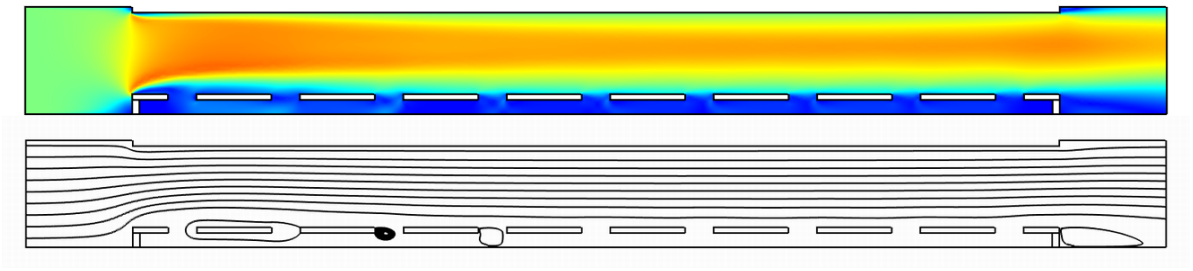

(f) the hole diameter is 4 mm, the Stoke number is 2.00×10^{-4}

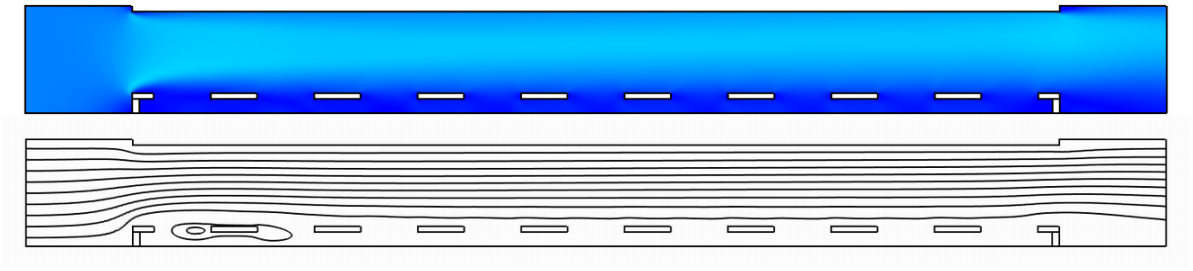

(g) the hole diameter is 8 mm, the Stoke number is 0.67×10^{-4}

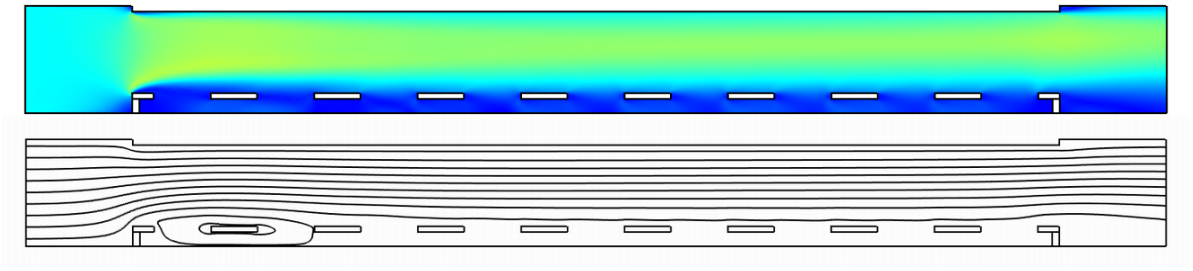

(h) the hole diameter is 8 mm, the Stoke number is 1.30×10^{-4}

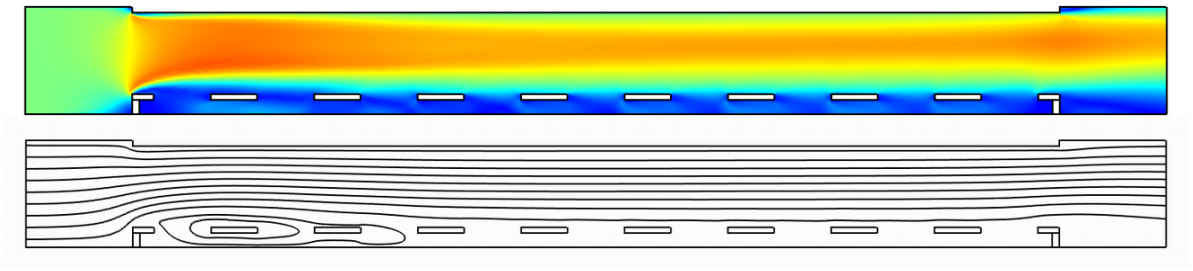

(i) the hole diameter is 8 mm, the Stoke number is 2.00×10^{-4}

Figure 4.13: The mean velocity fields and the corresponding mean streamlines. The unit of the color legend is m/s.

4.3.5 Electrostatic Characteristics

Figure 4.14 shows the electric potential with different hole diameters, while Figure 4.15 shows the electric field with different hole diameters and repelling voltages. The pattern of both the electric potential and electric field change with the hole diameter, but not the repelling voltage. The magnitude of the repelling voltage does change the magnitude of the electric potential and the strength of electric field. When the hole diameter gets larger, the electric field strength in the gaps becomes stronger.

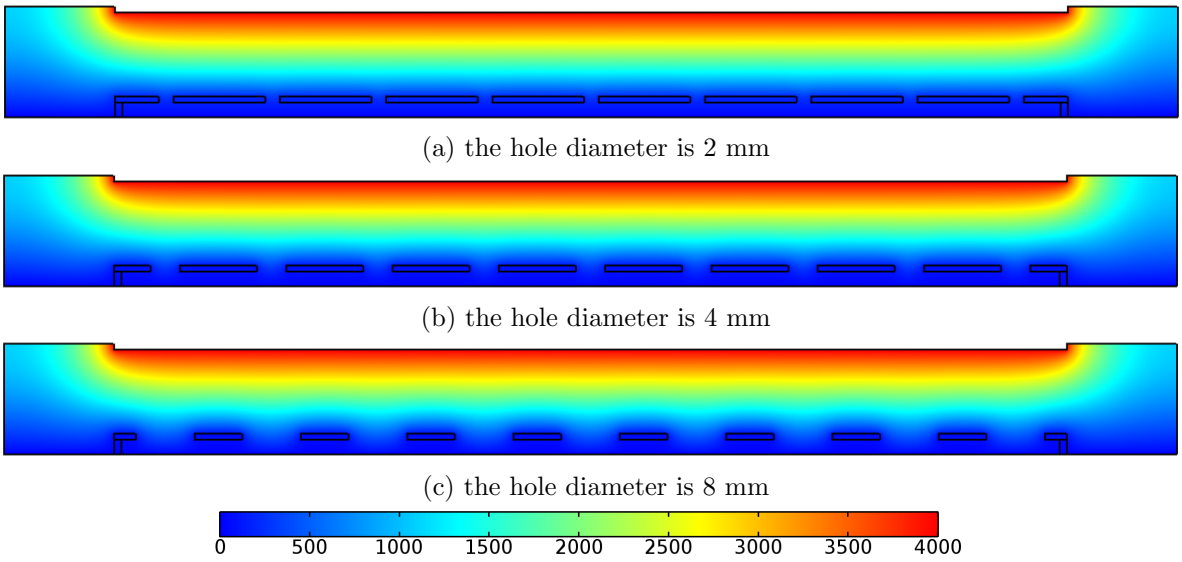

(a) the hole diameter is 2 mm

(b) the hole diameter is 4 mm

(c) the hole diameter is 8 mm

Figure 4.14: The electric potential with different hole diameters. The unit of the color legend is volts.

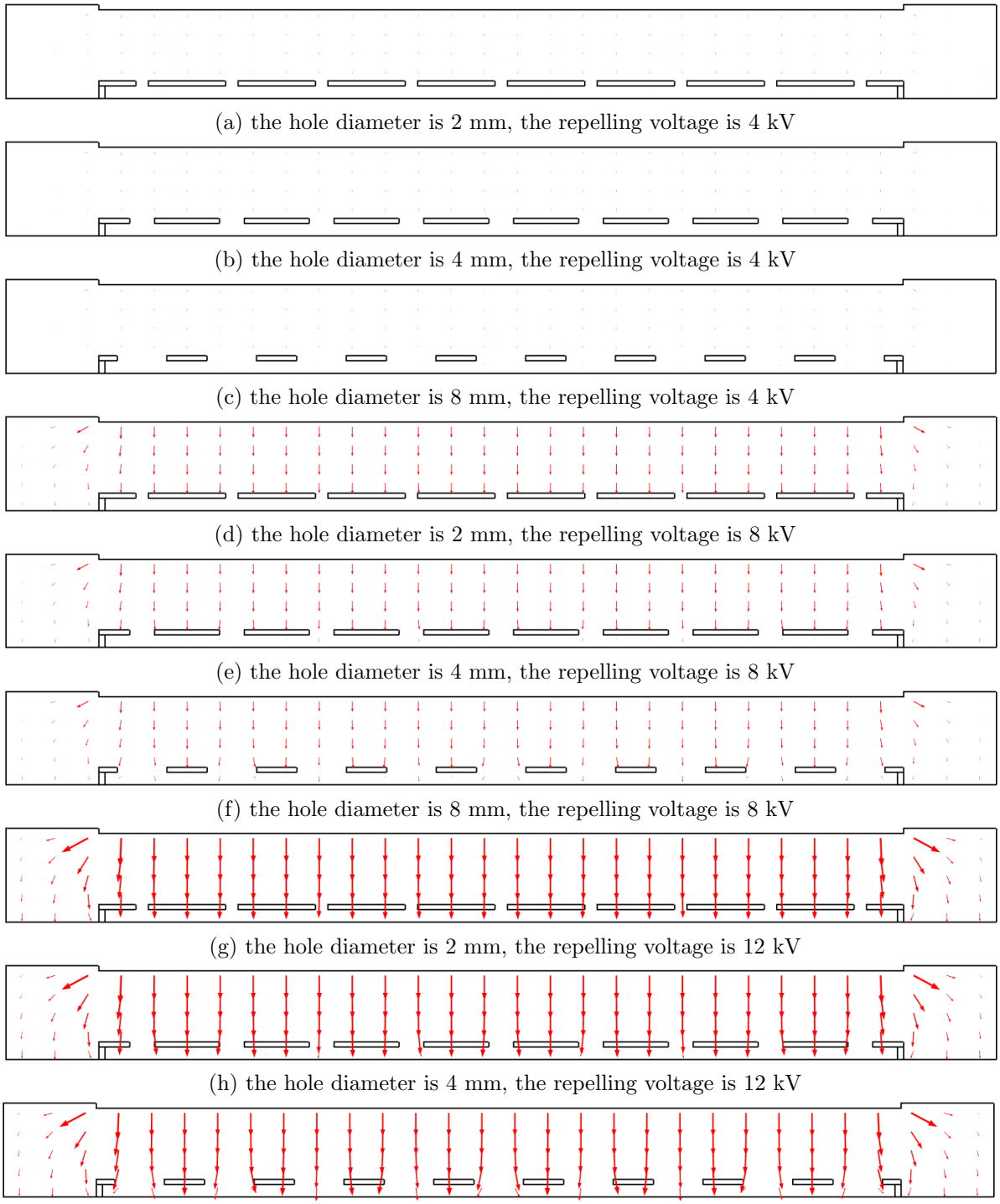

(a) the hole diameter is 2 mm, the repelling voltage is 4 kV

(b) the hole diameter is 4 mm, the repelling voltage is 4 kV

(c) the hole diameter is 8 mm, the repelling voltage is 4 kV

(d) the hole diameter is 2 mm, the repelling voltage is 8 kV

(e) the hole diameter is 4 mm, the repelling voltage is 8 kV

(f) the hole diameter is 8 mm, the repelling voltage is 8 kV

(g) the hole diameter is 2 mm, the repelling voltage is 12 kV

(h) the hole diameter is 4 mm, the repelling voltage is 12 kV

(i) the hole diameter is 8 mm, the repelling voltage is 12 kV

Figure 4.15: The electric field with different hole diameters and repelling voltages. The length of the arrow represents the electric field strength (drawn to scale).

4.3.6 Particle Trajectories

Figure 4.16, Figure 4.17, and Figure 4.18 show the particle trajectories with different electrostatic numbers, Stoke numbers, and hole diameters. The color represents the resultant velocity of the particles.

Because the Stoke number is low, particles easily follow the airflow. Due to flow recirculation, particles that enter the gaps before the third or fourth hole move opposite to the airflow direction, and electrostatic forces cause these particles to settle down on the collecting plate. After the third or fourth hole, particles enter gaps and move forward with the airflow direction because of the lack of the recirculation, and finally deposit on the collecting electrode. Particles are also collected after the guidance plate, as expected, because there is a big recirculation region there. Additionally, when the electrostatic number increases, particles subject to stronger electrostatic forces and are collected farther before the outlet. Furthermore, more and more particles are able to enter the gaps when the hole diameter gets bigger. Note that particles can deposit on the guidance plate as well, so that the guidance plate is energized to more than one hundred volts.

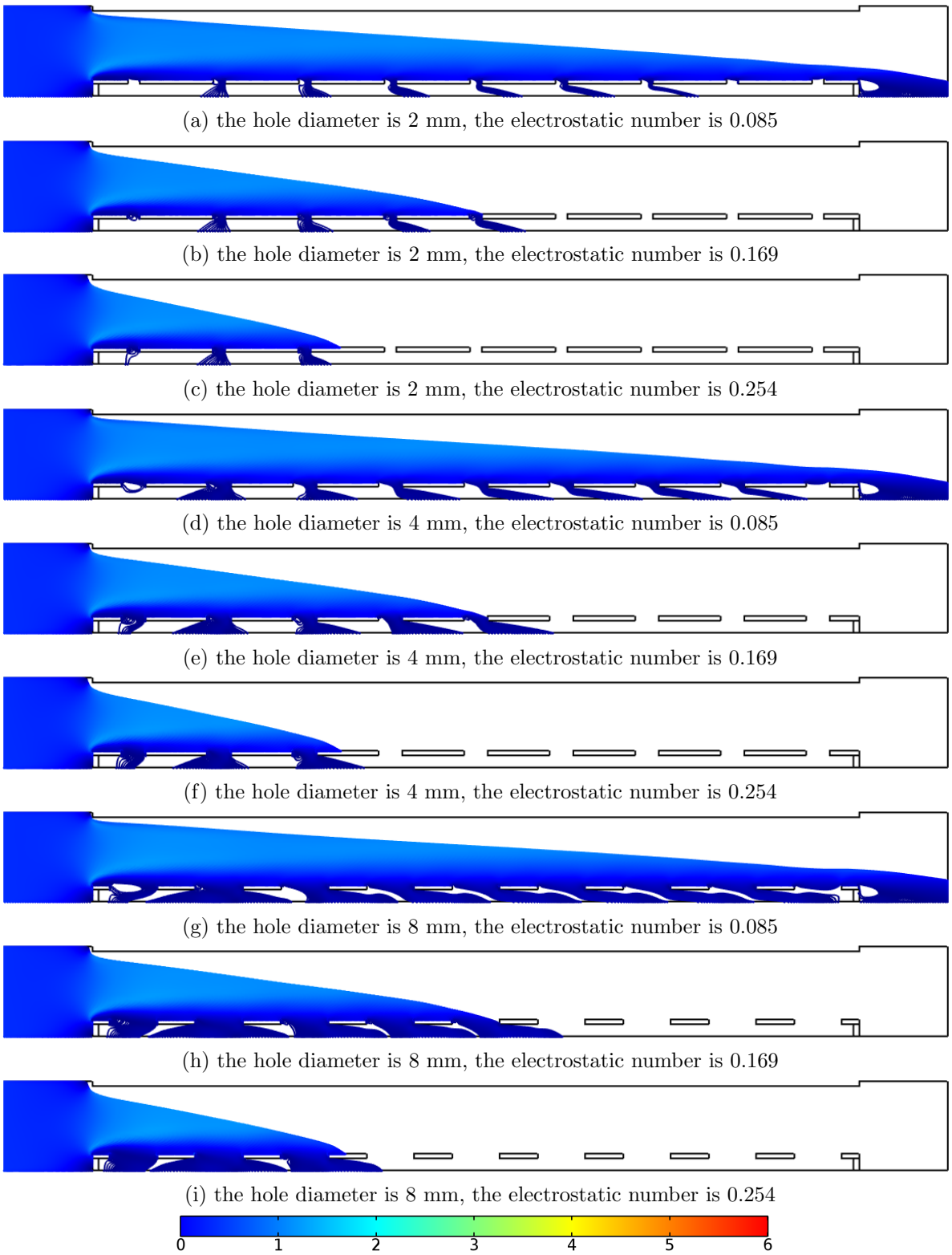

(a) the hole diameter is 2 mm, the electrostatic number is 0.085

(b) the hole diameter is 2 mm, the electrostatic number is 0.169

(c) the hole diameter is 2 mm, the electrostatic number is 0.254

(d) the hole diameter is 4 mm, the electrostatic number is 0.085

(e) the hole diameter is 4 mm, the electrostatic number is 0.169

(f) the hole diameter is 4 mm, the electrostatic number is 0.254

(g) the hole diameter is 8 mm, the electrostatic number is 0.085

(h) the hole diameter is 8 mm, the electrostatic number is 0.169

(i) the hole diameter is 8 mm, the electrostatic number is 0.254

Figure 4.16: The particle trajectories when the Stoke number is 0.67×10^{-4}. The unit of the color legend is m/s.

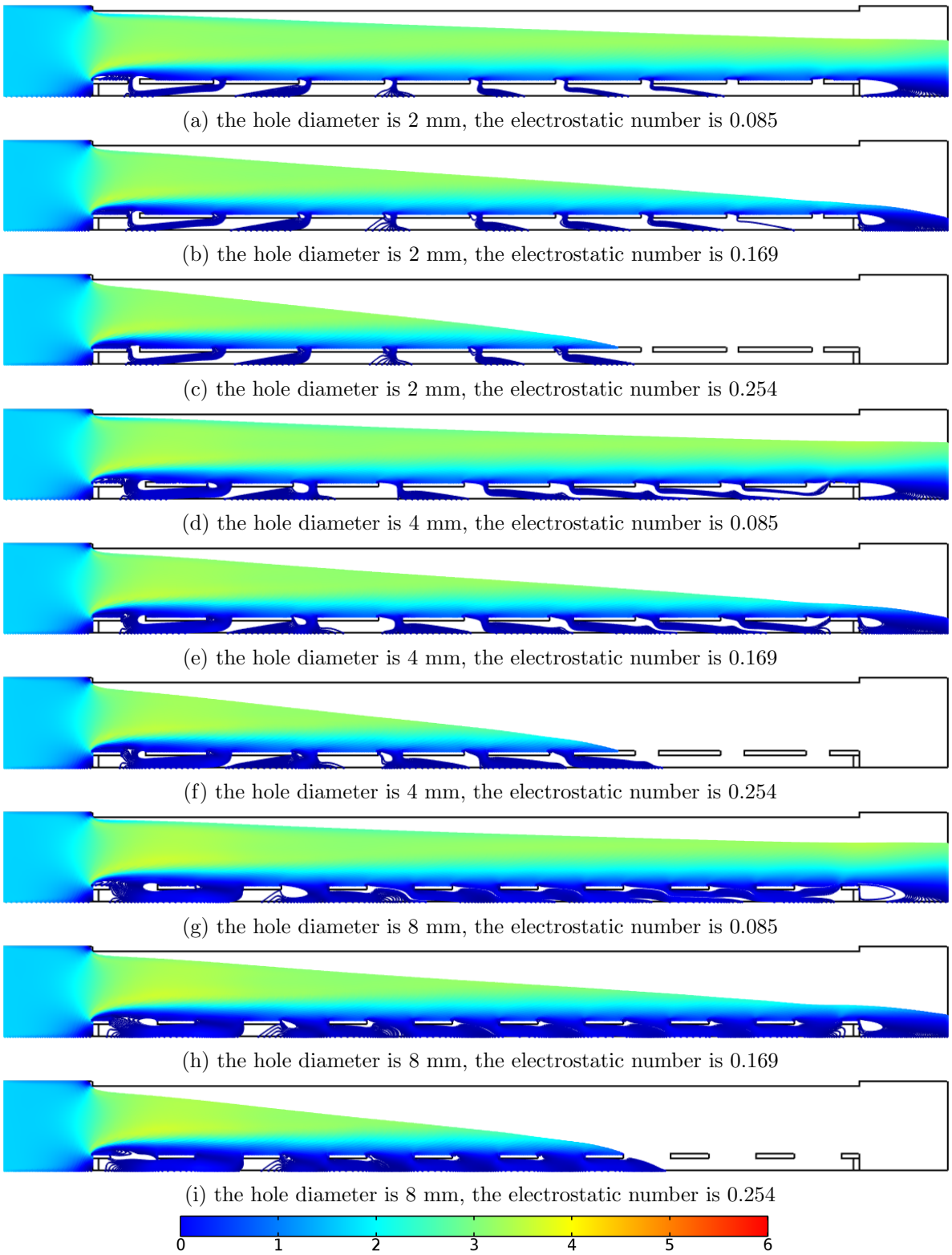

(a) the hole diameter is 2 mm, the electrostatic number is 0.085

(b) the hole diameter is 2 mm, the electrostatic number is 0.169

(c) the hole diameter is 2 mm, the electrostatic number is 0.254

(d) the hole diameter is 4 mm, the electrostatic number is 0.085

(e) the hole diameter is 4 mm, the electrostatic number is 0.169

(f) the hole diameter is 4 mm, the electrostatic number is 0.254

(g) the hole diameter is 8 mm, the electrostatic number is 0.085

(h) the hole diameter is 8 mm, the electrostatic number is 0.169

(i) the hole diameter is 8 mm, the electrostatic number is 0.254

Figure 4.17: The particle trajectories when the Stoke number is 1.30×10^{-4}. The unit of the color legend is m/s.

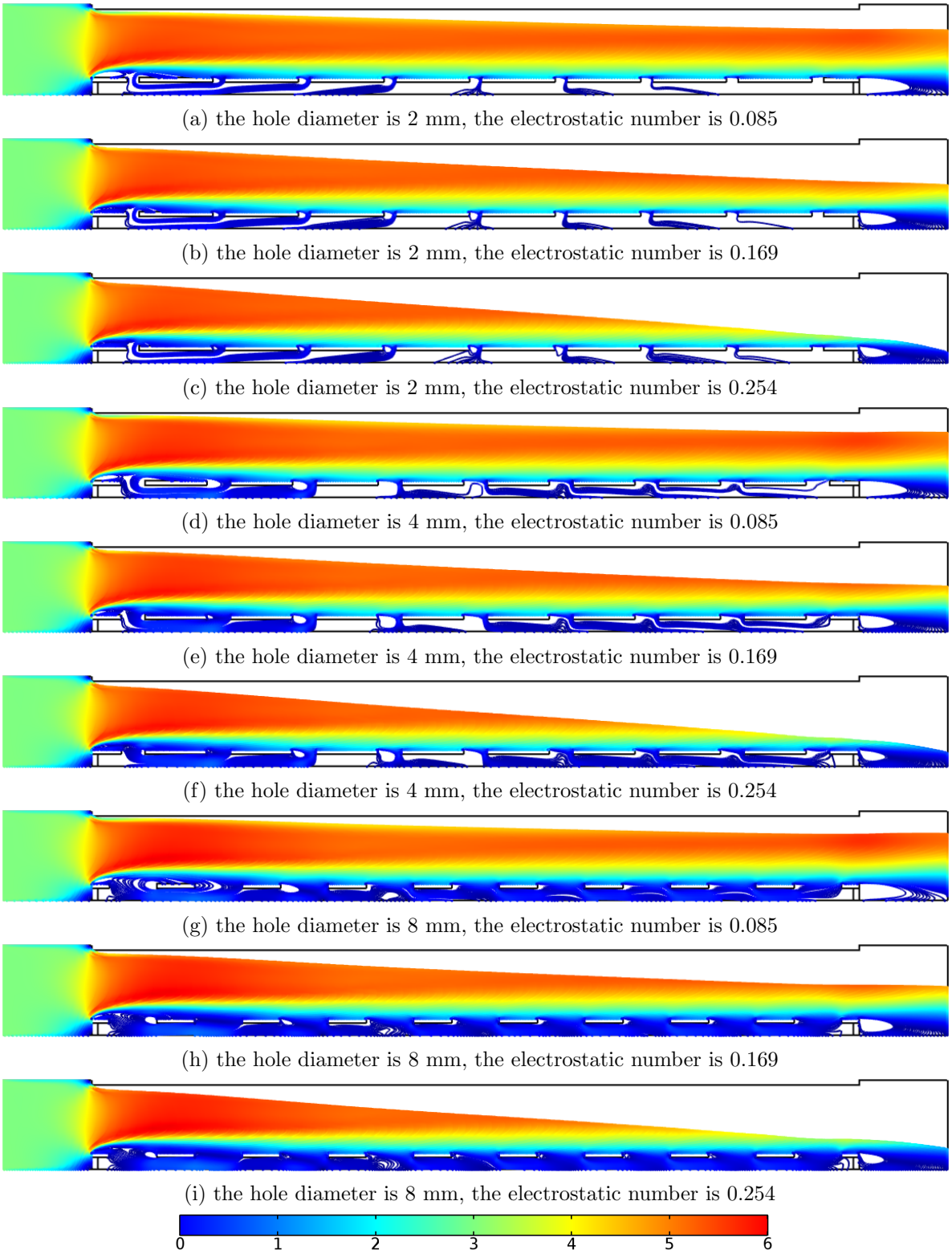

(a) the hole diameter is 2 mm, the electrostatic number is 0.085

(b) the hole diameter is 2 mm, the electrostatic number is 0.169

(c) the hole diameter is 2 mm, the electrostatic number is 0.254

(d) the hole diameter is 4 mm, the electrostatic number is 0.085

(e) the hole diameter is 4 mm, the electrostatic number is 0.169

(f) the hole diameter is 4 mm, the electrostatic number is 0.254

(g) the hole diameter is 8 mm, the electrostatic number is 0.085

(h) the hole diameter is 8 mm, the electrostatic number is 0.169

(i) the hole diameter is 8 mm, the electrostatic number is 0.254

Figure 4.18: The particle trajectories when the Stoke number is 2.00×10^{-4}. The unit of the color legend is m/s.

4.3.7 Particle Re-entrainment

Keeping the wall boundary conditions as "freeze", a separate set of simulations is carried out here to simulate particle re-entrainment. There are 1000 particles released uniformly either from the top surface of the guidance plate or from the collecting electrode. These re-entered particles can be completely discharged because they physically touch a large metal plate (guidance plate or collecting electrode); they can also be recharged by colliding with other charged particles or ions [142, 143]. Thus, this set of simulations simply assumes two charging conditions for these re-entered particles: 1) fully discharged (zero charge), and 2) 25% charged.

Particles that are released from the collecting electrode remain trapped inside the gaps, regardless of the charging status, the airflow velocity, and the hole diameter, because of the low flow velocity inside the gaps. The re-entrainment rate is hence zero.

Figure 4.19 and Figure 4.20 show the particle re-entrainment trajectories and the particle re-entrainment rates when particles are released from the top surface of the guidance plate at fully discharged and 25% charged conditions, respectively. Table 4.6 summarizes the particle re-entrainment rates when particles are released from the top surface of the guidance plate at fully discharged and 25% charged conditions. Most of the particles that are fully discharged do not travel too far from where they are released, while others follow a trajectory to escape the collector. When particles are 25% charged, many of the particles that enter the gaps are recollected, because the induced electrostatic forces drive these partially charged particles toward the collecting electrode.

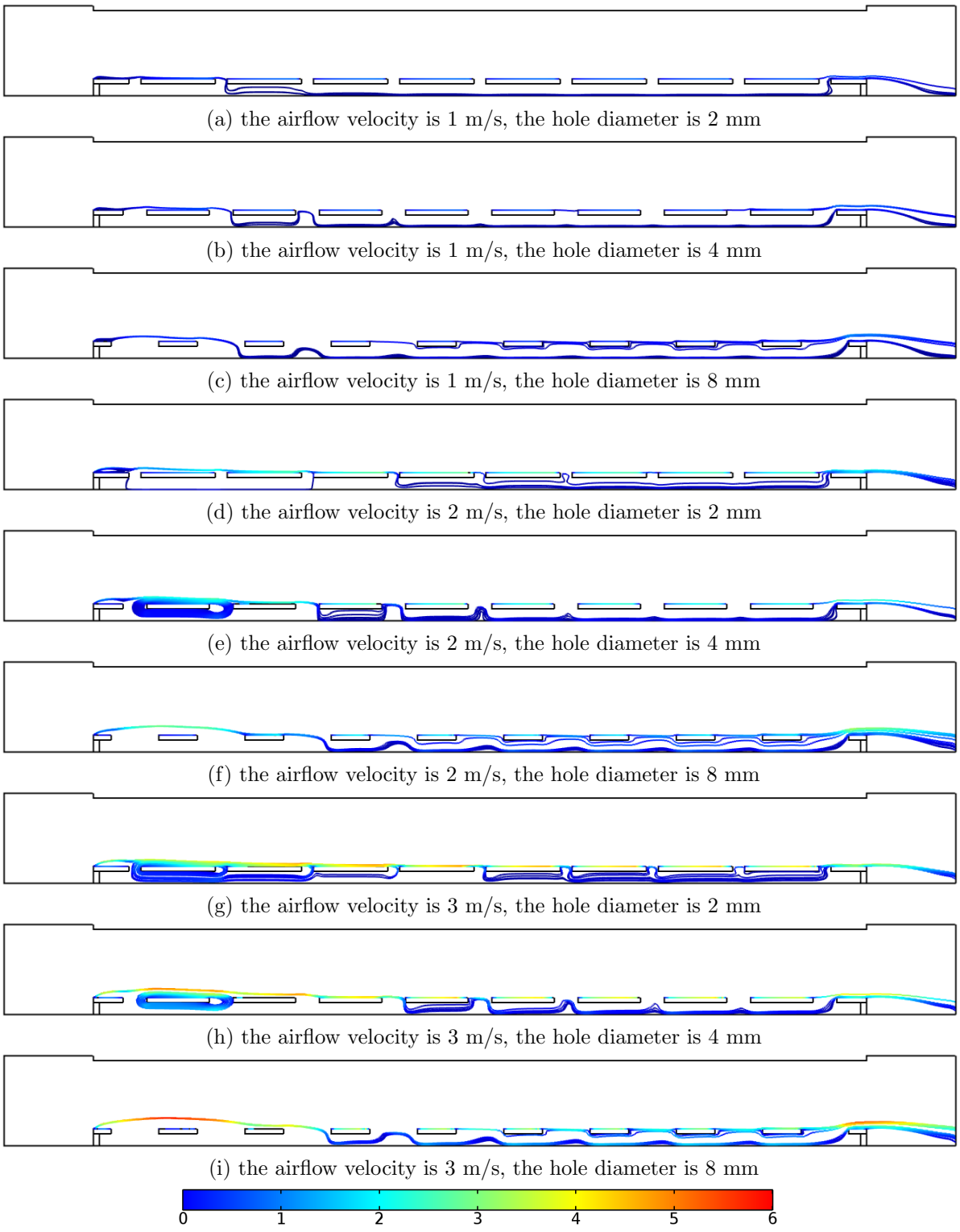

(a) the airflow velocity is 1 m/s, the hole diameter is 2 mm

(b) the airflow velocity is 1 m/s, the hole diameter is 4 mm

(c) the airflow velocity is 1 m/s, the hole diameter is 8 mm

(d) the airflow velocity is 2 m/s, the hole diameter is 2 mm

(e) the airflow velocity is 2 m/s, the hole diameter is 4 mm

(f) the airflow velocity is 2 m/s, the hole diameter is 8 mm

(g) the airflow velocity is 3 m/s, the hole diameter is 2 mm

(h) the airflow velocity is 3 m/s, the hole diameter is 4 mm

(i) the airflow velocity is 3 m/s, the hole diameter is 8 mm

Figure 4.19: The particle re-entrainment trajectories when the particles are fully discharged and are released from the top side of the guidance plate. The repelling voltage is 4 kV. The unit of the color legend is m/s.

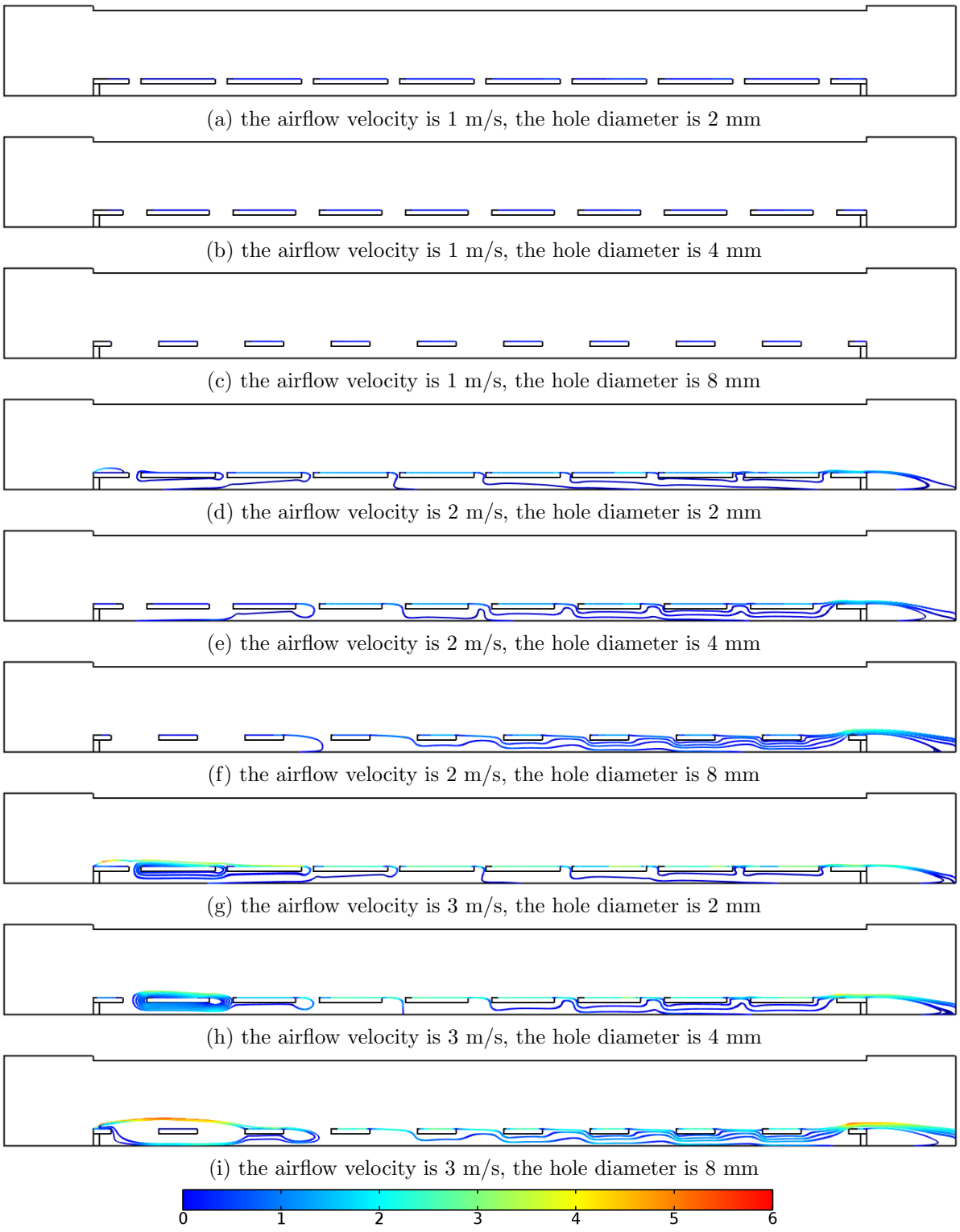

(a) the airflow velocity is 1 m/s, the hole diameter is 2 mm

(b) the airflow velocity is 1 m/s, the hole diameter is 4 mm

(c) the airflow velocity is 1 m/s, the hole diameter is 8 mm

(d) the airflow velocity is 2 m/s, the hole diameter is 2 mm

(e) the airflow velocity is 2 m/s, the hole diameter is 4 mm

(f) the airflow velocity is 2 m/s, the hole diameter is 8 mm

(g) the airflow velocity is 3 m/s, the hole diameter is 2 mm

(h) the airflow velocity is 3 m/s, the hole diameter is 4 mm

(i) the airflow velocity is 3 m/s, the hole diameter is 8 mm

Figure 4.20: The particle re-entrainment trajectories when the particles are 25% charged and are released from the top side of the guidance plate. The repelling voltage is 4 kV. The unit of the color legend is m/s.

Table 4.6: Re-entrainment rates. Particles are released from the top side of the guidance plate. The repelling voltage is 4 kV.

Airflow Velocity (m/s)	Hole Diameter (mm)	Re-entrainment Rate for Fully Discharged Particles (%)	Re-entrainment Rate for 25% Charged Particles (%)
1	2	0.5	0
1	4	0.7	0
1	8	2.2	0
2	2	0.6	0.9
2	4	0.7	1.4
2	8	2.1	0.8
3	2	0.9	3.4
3	4	0.8	4.4
3	8	2.1	8.6

4.4 Experimental Results and Discussion

This section presents the experimental collection efficiencies for the baseline GPC-ESPs. Comparisons between the baseline GPC-ESPs and the BE-ESPs are also demonstrated to provide evidence that this particle-trapping mechanism works in enhancing collection efficiency of ESPs.

4.4.1 Collection Efficiency

Figure 4.21 shows the collection efficiencies of the GPC-ESPs and the BE-ESPs. The collection efficiencies of the GPC-ESPs are always higher than those of the BE-ESPs. The minimum difference of the collection efficiencies between the BE-ESPs and the GPC-ESPs is 2.9%, while the maximum difference is 22.8% and the average difference is 8.9%.

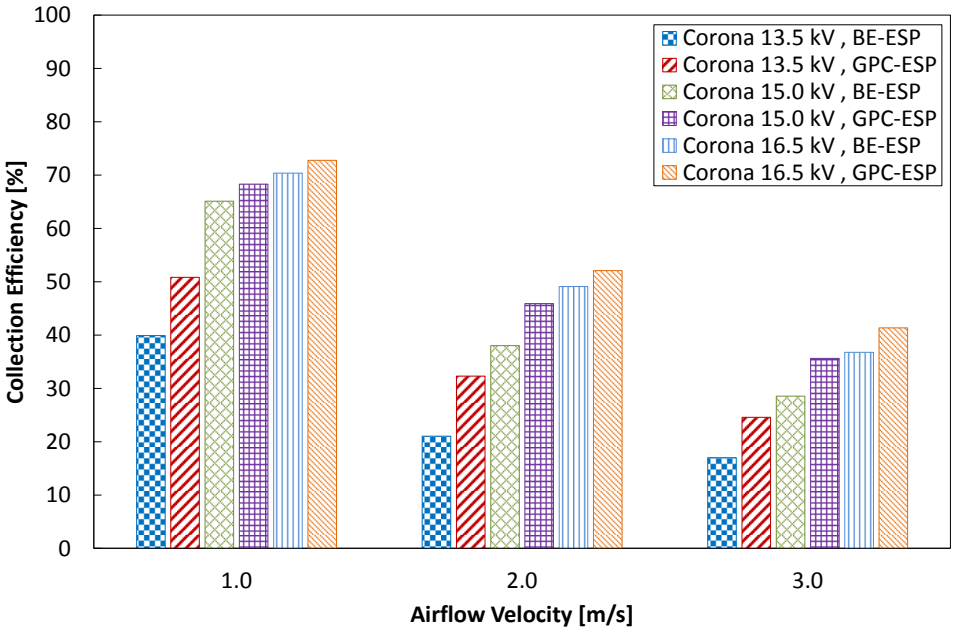

(a) Repelling voltage is 4 kV

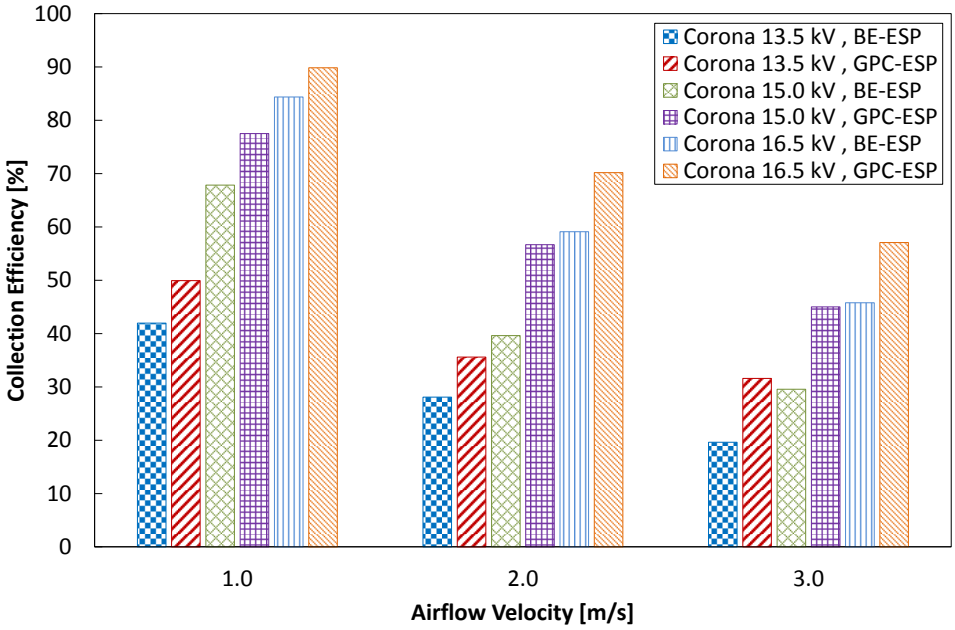

(b) Repelling voltage is 8 kV

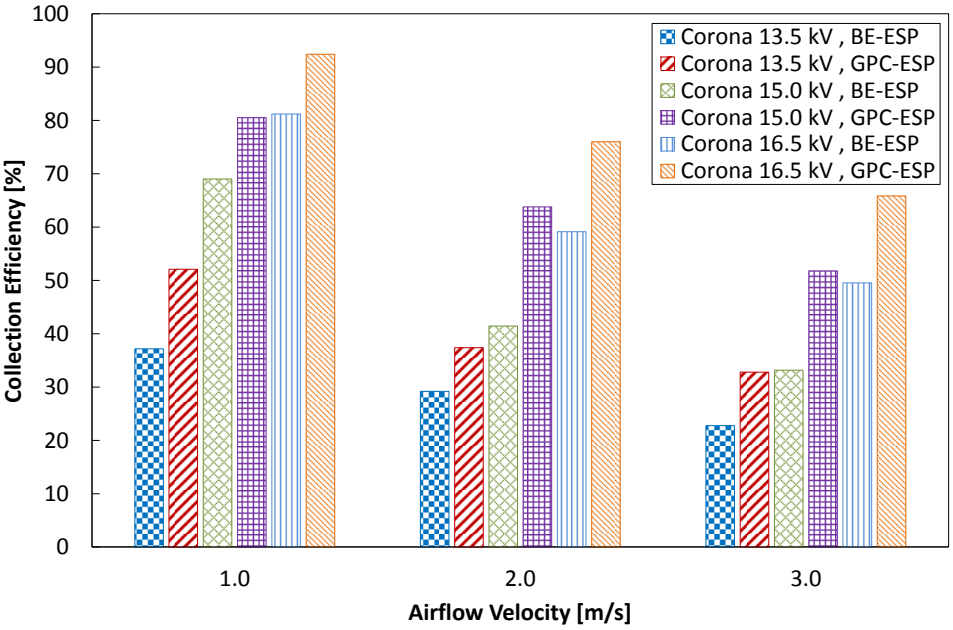

(c) Repelling voltage is 12 kV

Figure 4.21: The collection efficiencies of GPC-ESPs and BE-ESPs. Particle diameter is 0.3 µm.

Higher corona voltage results in higher collection efficiency because the particles are charged better during the ionization processes. When the charged particles are exerted at higher electrostatic forces (which is proportional to the repelling voltage), they move to and settle on the collecting electrodes within the limited channel length [3]. Therefore, a higher repelling voltage helps the ESP increase collection efficiency. On the other hand, the free airflow velocity also influences the collection efficiency. A higher free airflow velocity blows the particles out of the ESP channels before being captured by the collecting electrodes. Thus, a lower free airflow velocity promotes a higher collection efficiency.

4.4.2 Corona Power

Figure 4.22 shows the corona power of the GPC-ESPs and the BE-ESPs. Note that the power consumption of the fans and the repelling electrodes are not accounted for. The power consumption accounts for only the corona electrodes, which is the product of corona current and corona voltage. The amount of corona current depends on several factors, such as the space charge density, the pattern of the electric field, the applied airflow velocity, and the particle concentration. More charges, carried by electrons or ions, go into the corona electrodes, resulting in a higher corona current.

The corona power of the GPC-ESPs is higher than that of the BE-ESPs, which could be caused by the difference in the electric field. Both ESPs under test consume more corona power when the free airflow velocity increases. This is because a higher free airflow velocity brings more particles and molecules through the ionization region within a given time interval.

As a result, more electrons are generated (due to ionization processes) and are attracted to the corona electrode. The corona power also increases when higher corona voltage is applied, because more electrons are generated and are attracted to the corona electrode. Furthermore, when the repelling voltage increases, the corona power decreases. This is because the potential difference between the repelling and corona electrodes decreases, and fewer electrons go to the corona electrode.

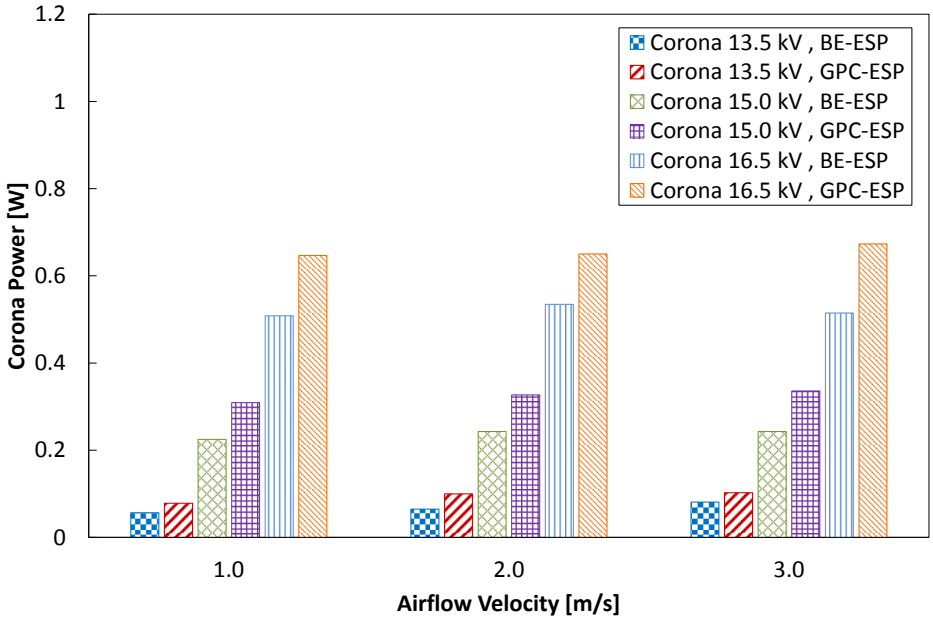

(a) Repelling voltage is 4 kV

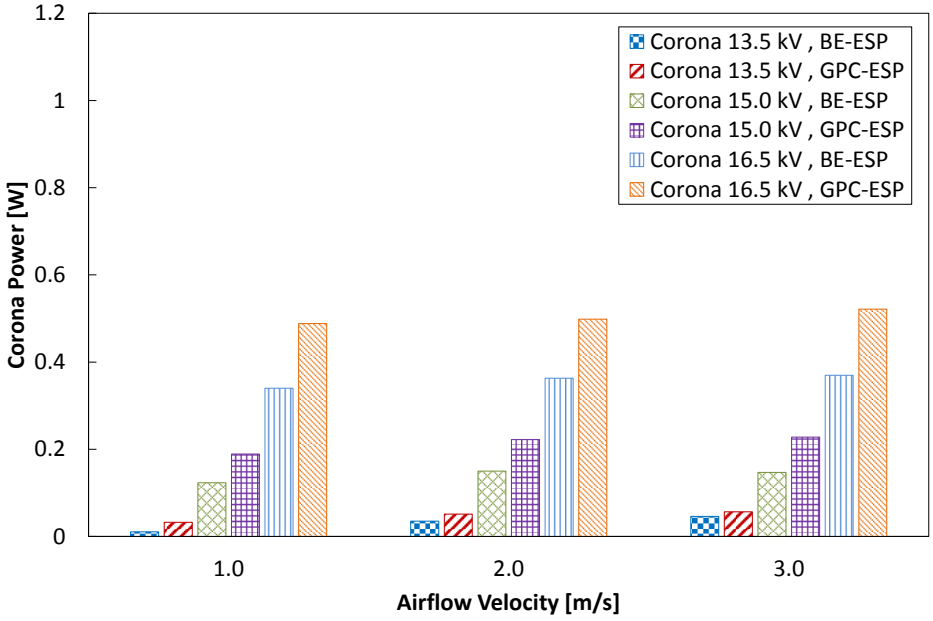

(b) Repelling voltage is 8 kV

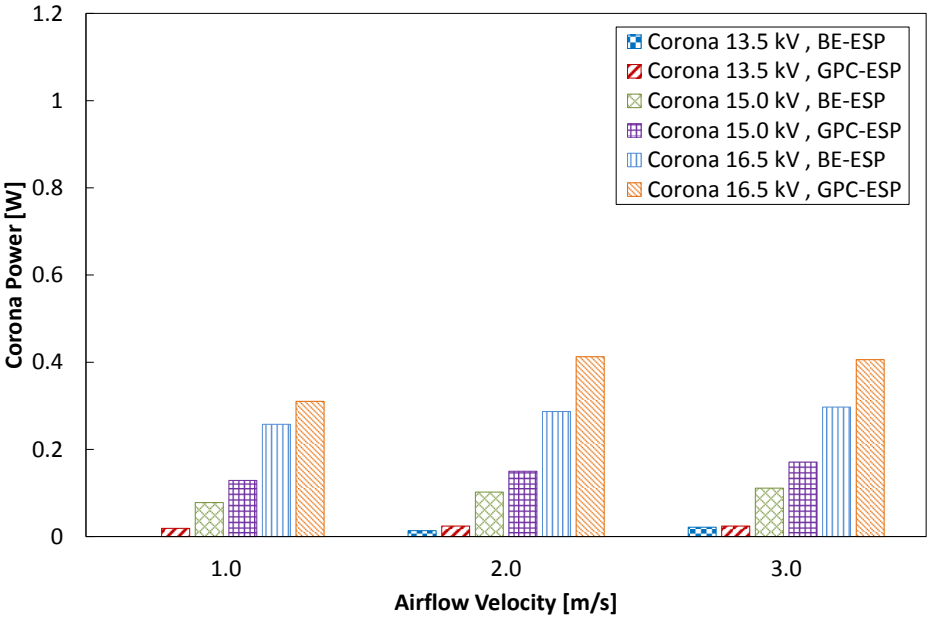

(c) Repelling voltage is 12 kV

Figure 4.22: The corona power of the GPC-ESPs and the BE-ESPs.

4.5 Parametric Study of Hole Parameters in the Guidance Plate

Two parameters of the holes in the guidance plate are studied: diameter and density. Figure 4.23 shows four different patterns of holes in the guidance plate, while Table 4.7 shows the corresponding specifications and the naming rules. The free airflow velocity is fixed at 3.0 m/s and particle diameter is 0.3 µm. Note that GPC4_128 is the baseline shown in the previous section.

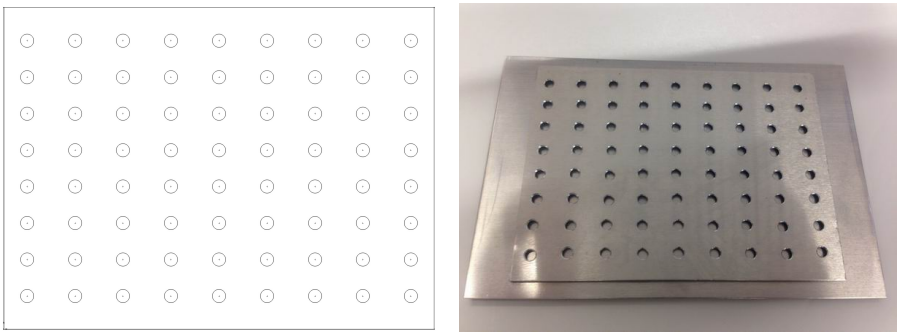

(a) GPC4_72

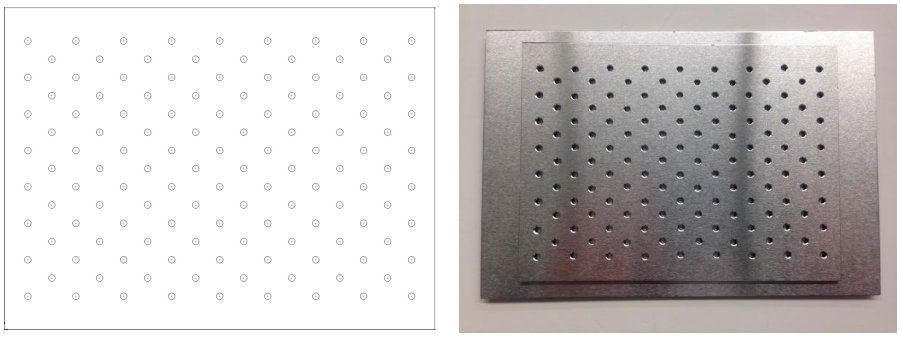

(b) GPC2_128

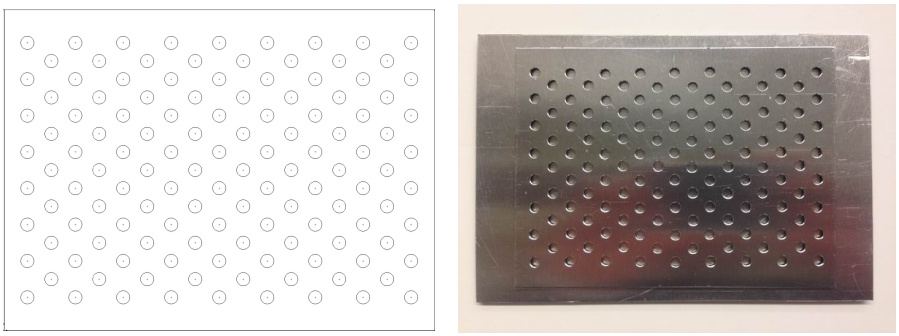

(c) GPC4_128 (baseline)

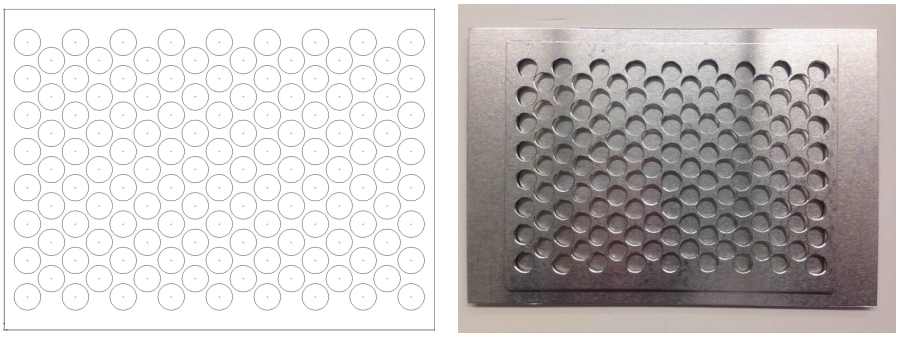

(d) GPC8_128

Figure 4.23: Different patterns of the holes in the guidance plate. The dimension of the guidance plate is 130 mm by 98 mm by 0.81 mm. The CAD drawings are drawn to scale.

Table 4.7: The specifications and the naming rules of the holes in the guidance plate. The "Effective Opening Rate" is defined as the ratio of all the hole areas to the total surface area of the guidance plate.

Condition Name	Diameter of Holes (mm)	Number of Holes	Effective Opening Rate (%)
GPC4_72	4	72	7.1
GPC2_128	2	128	3.2
GPC4_128	4	128	12.6
GPC8_128	8	128	50.5

4.5.1 Collection Efficiency

4.5.1.1 Experimental Results

Figure 4.24 shows the collection efficiencies of the GPC-ESPs with different diameters and densities of holes. The GPC-ESPs have absolutely higher collection efficiencies than the BE-ESPs.

In general, the GPC-ESPs with 4 mm holes have higher collection efficiencies than the GPC-ESPs with 2 mm holes. The GPC-ESPs with 8 mm holes have the lowest collection efficiencies, because they have significantly higher opening rates than other cases (see Table 4.7). In other words, the GPC-ESPs with 8 mm holes lose the ability of "trapping particle", because the disturbances in the gaps between the collecting electrodes and guidance plates are larger than other cases. On the other hand, the GPC-ESPs with denser holes have higher collection efficiencies than those with fewer holes. This is reasonable, because the low density of the holes in the guidance plates results in a lower probability of particles entering the gaps in-between the guidance plates and the collecting electrodes, thus lowering the collection efficiency.

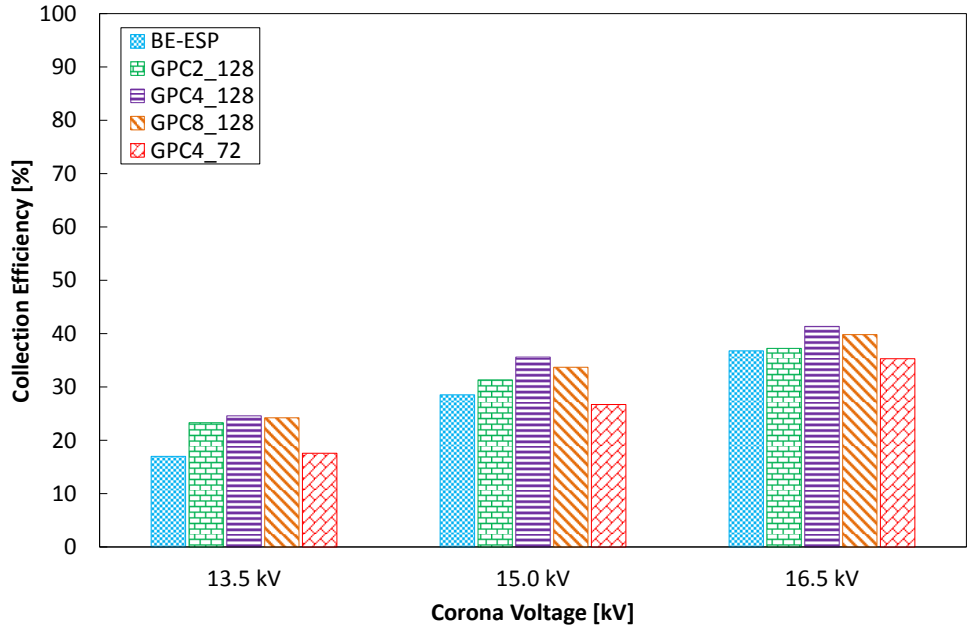

(a) Repelling voltage is 4 kV

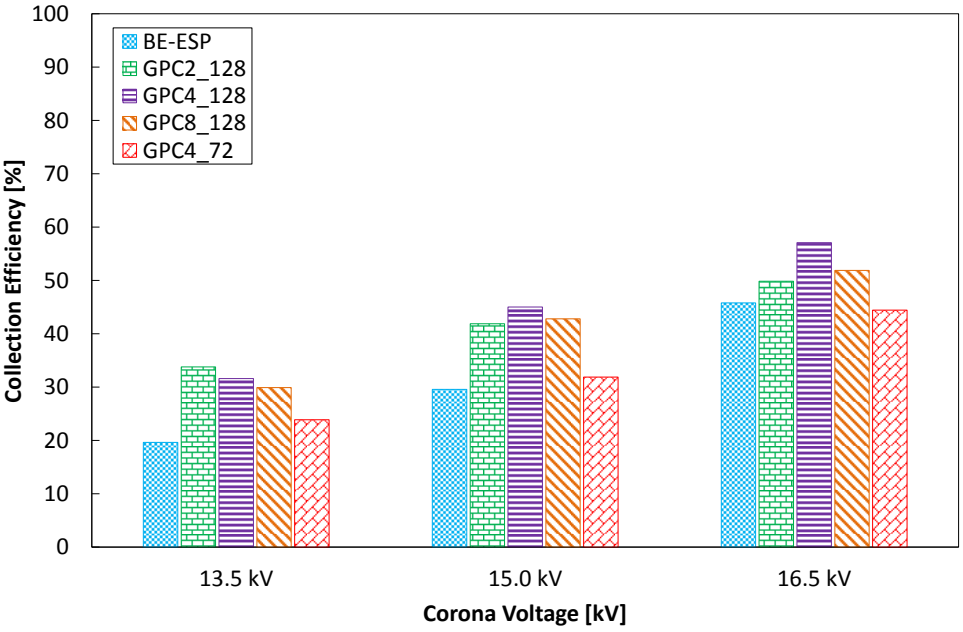

(b) Repelling voltage is 8 kV

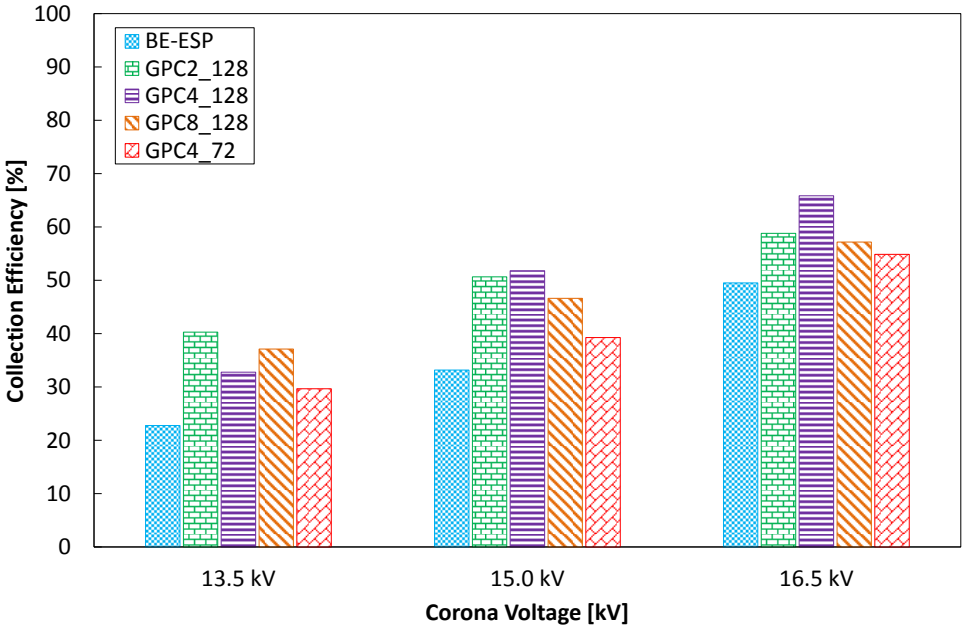

(c) Repelling voltage is 12 kV

Figure 4.24: The collection efficiencies of the GPC-ESPs with different hole diameters. The airflow velocity is 3.0 m/s. Particle diameter is 0.3 µm.

4.5.1.2 Numerical Predictions

For 0.3 µm particles and 16.5 kV corona voltage, Figure 4.25 shows the experimental and predicted collection efficiencies for hole diameters of 2 mm, 4 mm, and 8 mm. The collection efficiencies of the cases with 4 mm hole diameter are higher than those of the cases with 2 mm and 8 mm hole diameter. On the other hand, most of the predicted collection efficiencies are higher than the experimental collection efficiencies. These discrepancies may result from several assumptions made in the numerical model, such as particles are fully charged, particle re-entrainment is excluded, and particles do not rebound on the walls.

Both numerical and experimental results show that a lower Stoke number results in a

higher collection efficiency in. This is because the particles' residence time in the duct is longer when the Stoke number is lower [144]. The collection efficiency increases with the increase in the electrostatic number. The electrostatic number is a fraction of the Deutsch number (also a function of electrostatic force and viscous force) that has a direct influence on the collection efficiency, as shown in (2.16) and (2.22). It is noticeable that, from Figure 4.25, when the electrostatic numbers are 0.169, the predictions stay very close to each other despite a slight difference, but the collection efficiency decreases with the increase in the Stoke number.

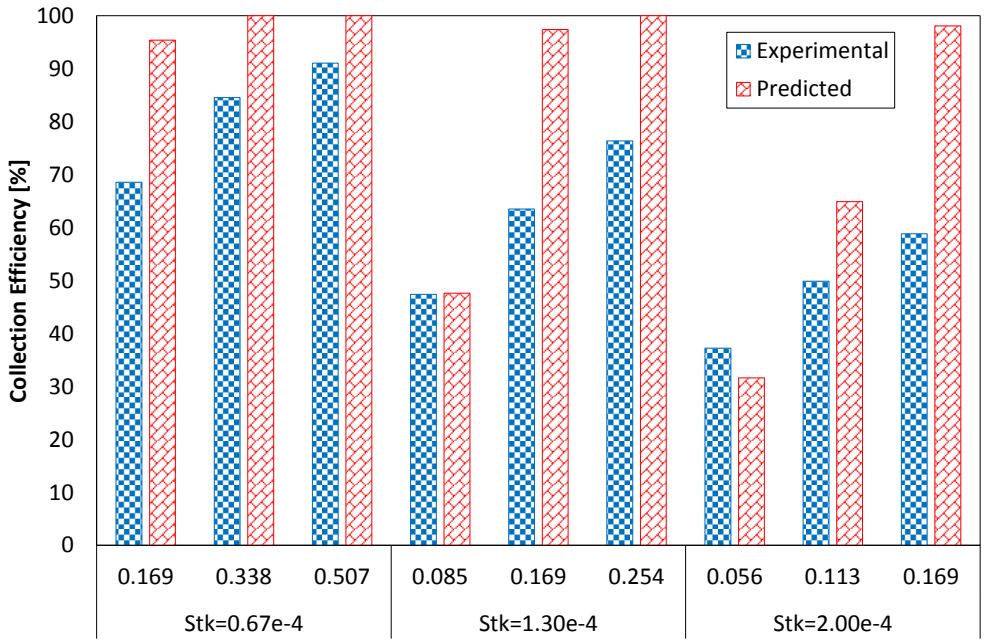

(a) Hole diameter is 2 mm

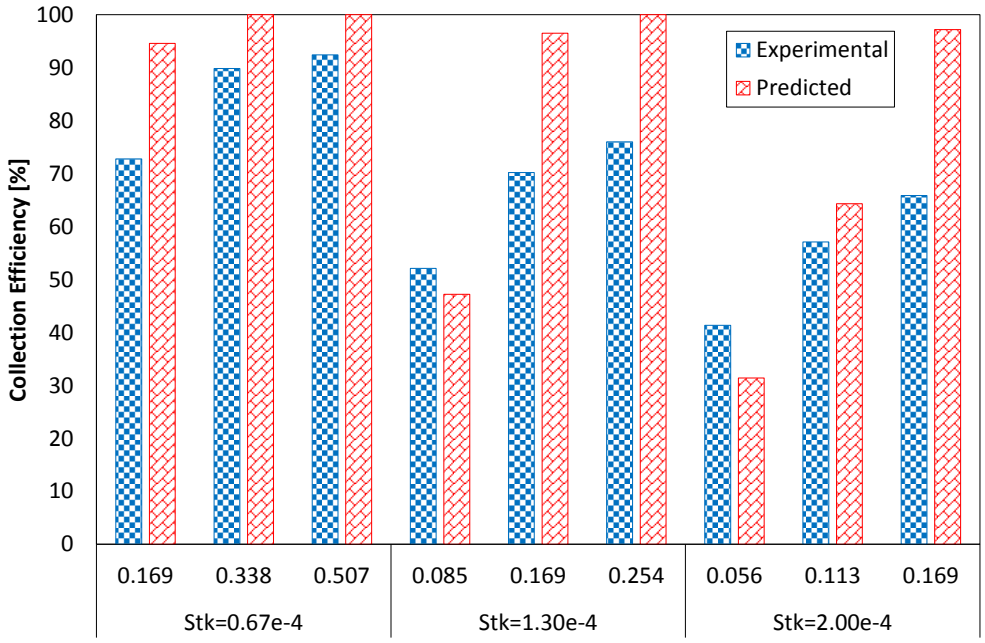

(b) Hole diameter is 4 mm

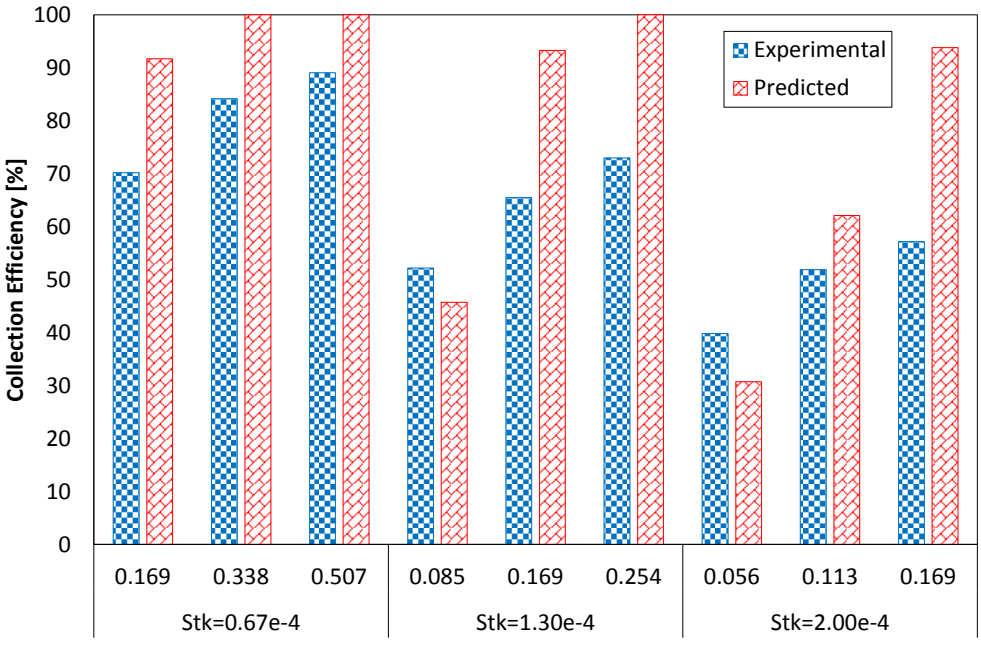

(c) Hole diameter is 8 mm

Figure 4.25: The experimental and numerical results of the collection efficiency. The upper x-axis is the electrostatic number and the lower x-axis is the Stoke number.

4.5.2 Corona Power

Figure 4.26 shows the corona power of the GPC-ESPs with different diameters and densities of holes. The GPC4_128 has higher corona power than others. Nevertheless, when the corona voltage increases, the differences of the corona power between the GPC4_128 and others increase. The corona power of the GPC4_128 is still higher than others. From Figure 4.26(a), the corona power of the GPC4_72 is lower than that of the BE-ESP, because the collection efficiencies of the GPC4_72 are lower than those of the BE-ESP, as shown in Figure 4.24(a). In general, a higher corona power (higher corona voltage) helps the ionization process take place more efficiently, thus enhancing the collection efficiency.

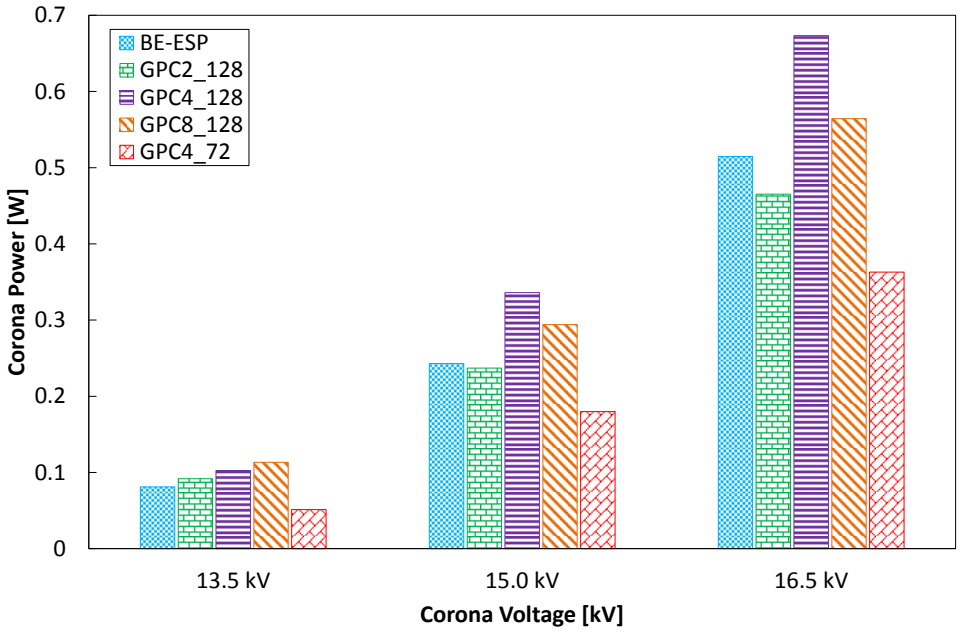

(a) Repelling voltage is 4 kV

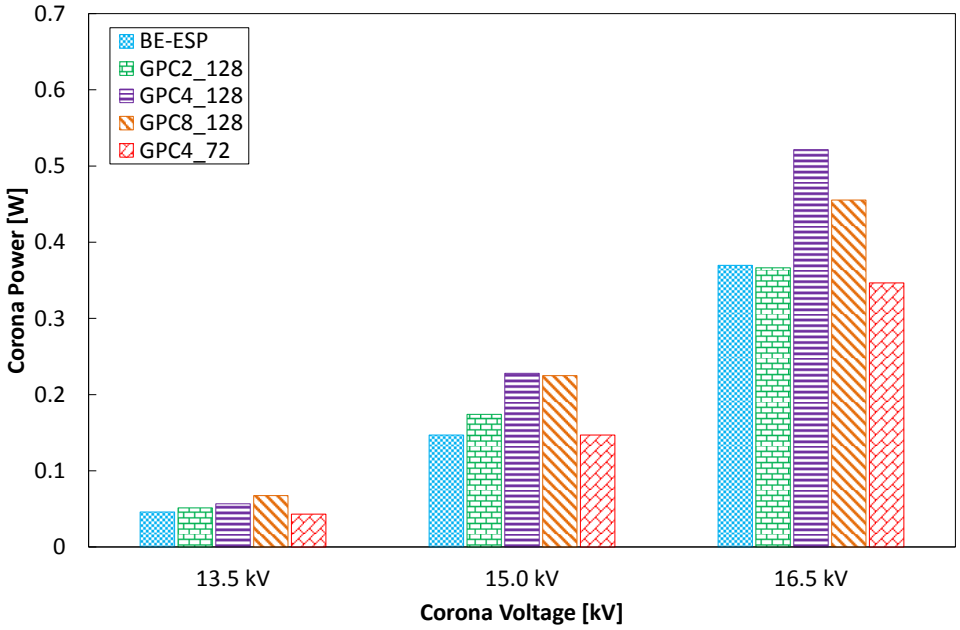

(b) Repelling voltage is 8 kV

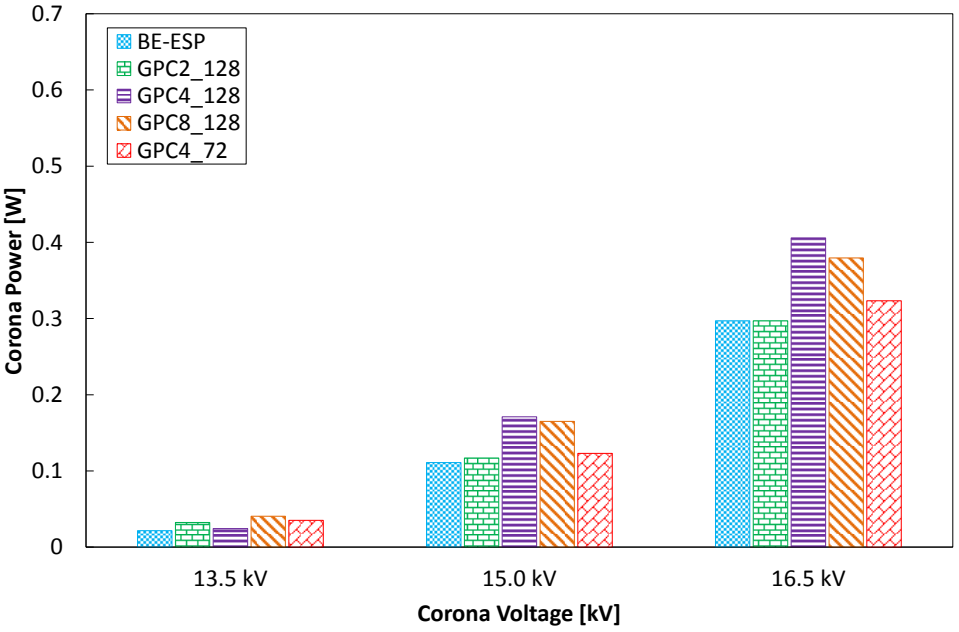

(c) Repelling voltage is 12 kV

Figure 4.26: The corona power of the GPC-ESPs with different hole diameters.

4.5.3 Key Energy Performance

To understand how parameters of interest affect ESPs' key energy performance, this section presents a full factorial experiment for GPC-ESPs that the author developed. Table 4.2 shows the parameters of interest and their corresponding levels.

Since ESPs are active filters that consume (corona) power, it is more practical to study how parameters of interest affect ESPs' key energy performance by taking into account ESPs' corona power. The collection efficiency of ESPs is not just a function of particle size and airflow velocity, it is also strongly dependent on the corona power. The magnitude of the airflow velocity determines the drag force (along the airflow direction) exerted on the particles, whereas the magnitude of the corona power determines the electrostatic force (transverse to the airflow direction) exerted on the particles. Lower drag force and higher electrostatic force exerted on the particles results in a higher collection efficiency. Additionally, the pressure drop of an ESP does not increase over time. Therefore, the system power consumption, the sum of the pump power and the corona power, has a strong relation to the collection efficiency. Once the system power consumption is obtained, the effective pressure drop of an ESP can be estimated using the following equation,

$$\Delta P_{eff} = \frac{W \times \eta_{system}}{Q} \tag{4.1}$$

where ΔP_{eff} is effective system pressure drop, W is system power consumption, Q is volumetric airflow rate, and η_{system} is the energy efficiency of the system (assumed to be 0.7).

Substituting (4.1) into (3.22), (4.2) represents the key energy performance in terms of the collection efficiency of the filter, the energy efficiency of the system, the system power consumption, and the volumetric airflow rate.

$$kep = \frac{-100 \times \log\left(1 - \eta_{filter}\right) \times Q}{W \times \eta_{system}} \tag{4.2}$$

At a given volumetric airflow rate, the key energy performance of the GPC-ESPs can be rated by measuring collection efficiencies [4] and system power consumption. Figure 4.27 shows the resulting key energy performance of the GPC-ESPs by using (4.2), in which all data is relative to the case that has airflow velocity 3.0 m/s, repelling voltage 4 kV, and corona voltage 13.5 kV. Higher repelling voltage and higher corona voltage result in higher key energy performance. This makes sense because higher repelling and corona voltages result in higher collection efficiency. Lower airflow velocity also results in higher key energy performance because the system power consumption decreases and collection efficiency increases.

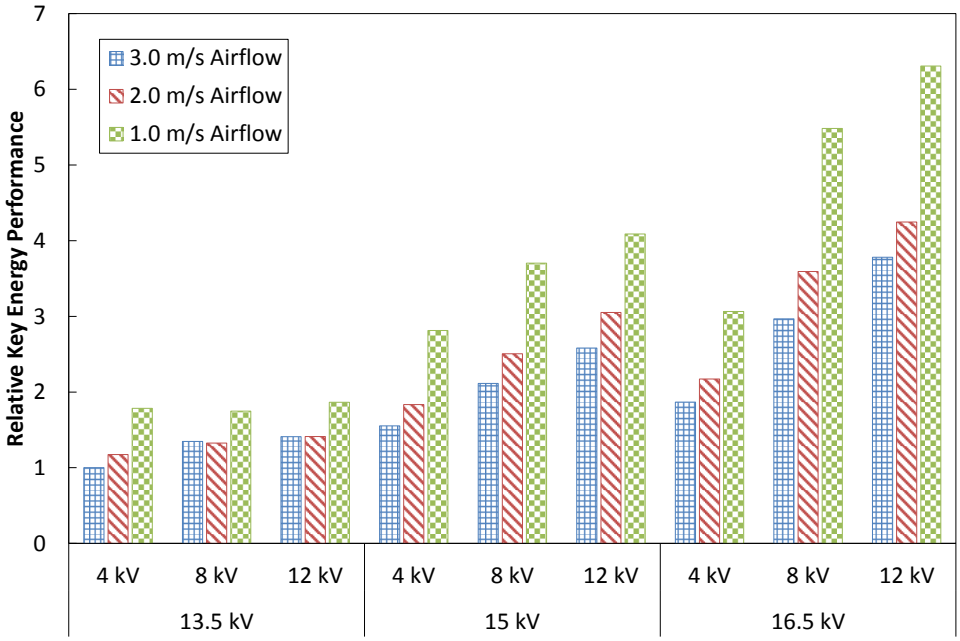

Figure 4.27: The relative key energy performance of the GPC-ESPs. The upper x-axis is the repelling voltage, and the lower x-axis is the corona voltage. The cross-sectional dimension of GPC-ESP is 98 mm by 30 mm. Particle diameter is 0.3 µm.

Figure 4.28 shows the surface contour plots of relative key energy performance of GPC-ESPs in terms of the corona voltage, the repelling voltage, and the airflow velocity, and (4.3) is the matching quantitative equation. The variables shown in (4.3) are coded, meaning that the maximum and minimum values are +1 and -1, corresponding to the maximum and minimum absolute values shown in Table 4.2. The coefficients of coded variables are obtained through regression analysis using the quadratic model, and are proportional to the observed effects (relative key energy performance).

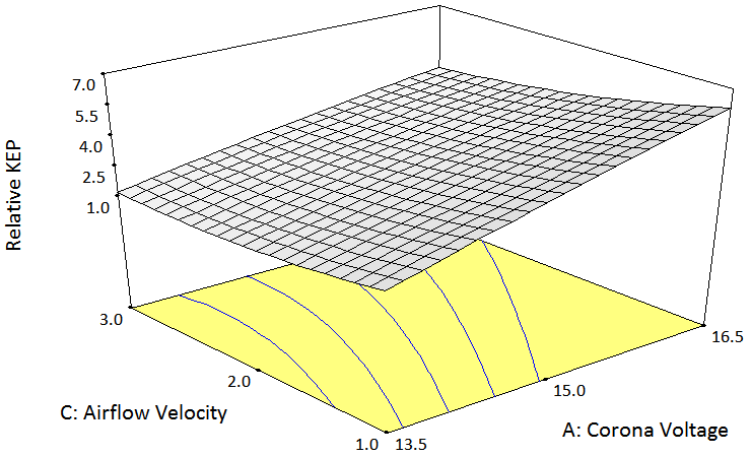

(a) Repelling voltage is 4 kV

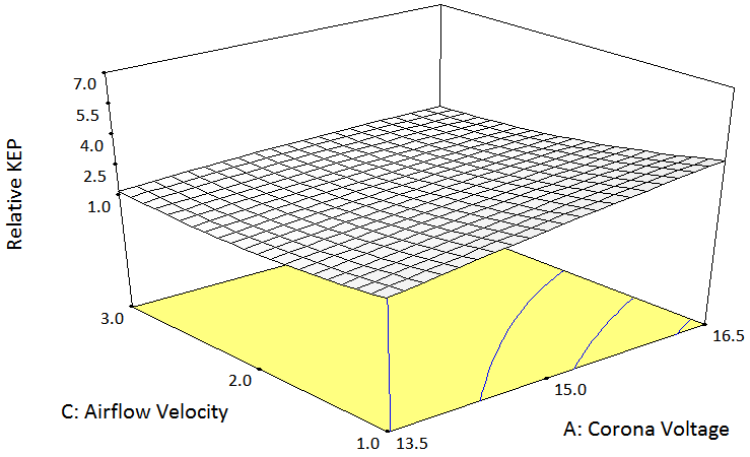

(b) Repelling voltage is 8 kV

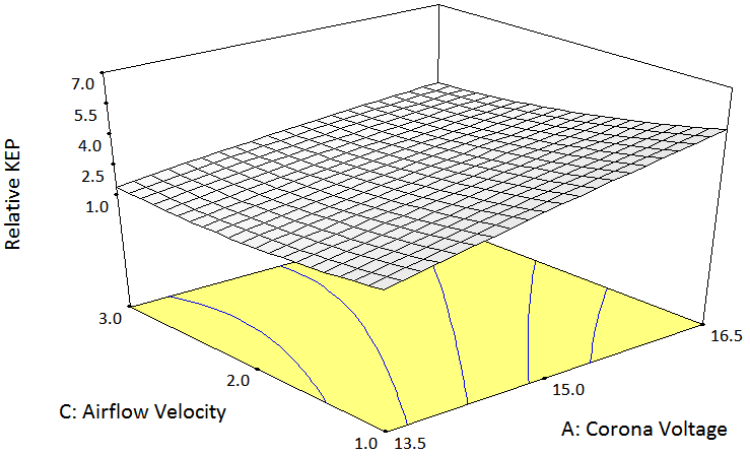

(c) Repelling voltage is 12 kV

Figure 4.28: Contours of relative key energy performance of the GPC-ESPs with different repelling voltages. Particle diameter is 0.3 µm.

$$\begin{aligned} kep =& 2.57 + 1.13A + 0.64B - 0.68C - 0.11A^2 - 0.20B^2 + 0.38C^2 \\ &+ 0.54AB - 0.38AC - 0.10BC \end{aligned} \tag{4.3}$$

where A is corona voltage, B is repelling voltage, and C is free airflow velocity.

Equation (4.3) shows that the corona voltage plays the most important role in determining the key energy performance of ESPs. This fact supports the previous justification that taking system power consumption into account is practical in studying how operating conditions affect the key energy performance of ESPs. The roles of repelling voltage and free airflow velocity are similar in determining key energy performance, while free airflow velocity is slightly important than repelling voltage.

4.6 Summary

This chapter demonstrates the experimental results of GPC-ESPs and BE-ESPs, including collection efficiency and corona power. Although GPC-ESPs consume higher corona power than BE-ESPs, GPC-ESPs have significantly higher collection efficiencies than BE-ESPs, regardless of the operating conditions such as corona voltage, repelling voltage, and free airflow velocity.

For the collection efficiency, a lower airflow velocity, a higher corona voltage, and a higher repelling voltage result in a higher collection efficiency. In other words, a lower Stoke number (the ratio of inertia force to viscous drag force) and a higher electrostatic number (the ratio of electrostatic force to viscous drag force) result in a higher collection

efficiency. Although the electrostatic number is a fraction of the Deutsch number that directly impacts the theoretical collection efficiency, the Stoke number still plays an important role in determining the collection efficiency. Both GPC-ESPs and BE-ESPs have a higher corona power at a higher airflow velocity, a higher corona voltage, and a lower repelling voltage.

The effects of the hole conditions in the guidance plates on the flow and electrical characteristics are also numerically studied. The hole diameter has an influence on the velocity field in the gaps. When the guidance plate has larger hole diameters, the flow recirculation in the first couple holes is stronger, allowing particles to easily enter the gaps through the holes. The electrical characteristics of the GPC-ESPs vary with both repelling voltage and hole diameter. The magnitude of the electric potential field changes mainly with the repelling voltage. The pattern of the electric field change only with the hole diameter. On the other hand, from the experimental results, the hole diameter does affect the collection efficiency. A moderate hole diameter is desired. A considerably large hole diameter loses the ability of trapping particles because of less cover, whereas a considerably small hole diameter allows for only a limited amount of particles to enter the gaps between the guidance plates and the collecting electrodes. Furthermore, from the experiments, GPC-ESPs with high hole density have high collection efficiencies. GPC-ESPs with relatively low hole density have low collection efficiencies, and can be as low as BE-ESPs.

The numerical results show that the guidance plate does suppress particle re-entrainment, no matter where the particles re-enter the environment. Such re-entered particles can be recaptured because of either the flow recirculation or the induced electrostatic forces (when

particles are partially recharged).

Regarding the key energy performance of GPC-ESPs, the parametric studies show that the key energy performance of an ESP increases when the repelling voltage and the corona voltage increase, but decreases when the free airflow velocity increases. This characteristic strongly relates to the collection efficiency and pressure drop. The collection efficiency is proportional to both corona and repelling voltages, but is inversely proportional to the free airflow velocity. The pressure drop of GPC-ESPs, on the other hand, stays unchanged over time. Besides, through the quantitatively analysis, the corona voltage plays the most important role in determining the key energy performance of an ESP.

Chapter 5

CONCLUSIONS AND FUTURE WORK

5.1 Conclusions

This dissertation presents two novel ESPs that have particle-trapping mechanisms used to suppress particle re-entrainment and improve collection efficiency. The lab-scale proof-of-concept prototypes have been built without introducing any fiber-based filters. The collection efficiency and the key energy performance of the prototypes are not only highly competitive but superior to those of traditional filters. This dissertation presents the design concepts, the theories of the collection efficiency and the key energy performance, and the numerical modeling in order to comprehensively characterize the performance of these two novel ESPs. Studies regarding how the parameters of interest affect the performance of ESPs are covered as well, especially focusing on the collection efficiency and the key energy performance.

This dissertation also compares the performance of a HEPA filter (3M E133), a commercially available ESP (Aprilaire 5000), a FC-ESP, and a GPC-ESP, in both collection efficiency and key energy performance perspectives. An example of energy savings, when the fiber-based filters are replaced with the foam-covered ESPs in Loew Hall, is provided and thoroughly discussed in this dissertation. Table 5.1 shows a comparison of important performance indicators and features between four different air filters.

This dissertation attempts to bring ESPs a step closer to non-industrial applications by bringing together and developing a body of knowledge relevant to high-efficiency ESPs: high collection efficiency and low pressure drop. By applying these novel particle-trapping mechanisms to traditional ESPs, this dissertation has successfully demonstrated the improvement of the collection efficiency of ESPs without introducing additional pressure drop.

Table 5.1: Comparisons of different air filters.

	HEPA Filter	Commercial ESP[1]	FC-ESP	GPC-ESP
Particle-Trapping Mechanism	No	No	Yes	Yes
Fine Particle Collection	High	High	High	High
Ultra-Fine Particle Collection	Yes[2]	Yes[2]	N/A	N/A
Particle Re-entrainment	No	Medium	Low	Low
Particle Accommodation	High[3]	High[3]	Medium[4]	High[4]
Pressure Drop	High	Medium	Low	Low
Key Energy Performance	Low	Medium	High	High
Consumable Materials	Yes	Yes	Yes	No
Unit Cost	Low	High	Medium	Medium
High Temperature Applications	No	No	OK	Yes
Ozone Emission	No	Yes	Yes	Yes

[1] Commercial ESP has a post fibrous filter
[2] Large pressure drop would be required
[3] Large pressure drop would be induced
[4] No additional pressure drop would be induced

5.1.1 Foam-Covered Electrostatic Precipitators

The foam-covered ESPs use porous foam to cover the collecting electrodes. Particles are collected in the pores of the foam instead of on the flat surface of the collecting electrodes. Abnormal power outages or disturbances such as passing airflow and vibrations thus have a lower chance to dislodge the collected particles from the collecting electrodes. The electrical conductivity of the foam is weak, and consequently the foam does not significantly degrade the electric field strength in the collector. The foam also prevents the conductive particles from fast discharging. Furthermore, the edges of the collecting and repelling electrodes are covered by foam, reducing the chance of spark discharge between the electrodes.

The in-house experiments and theoretical predictions show that the foam-covered ESP has up to 99% collection efficiency at certain conditions in a normal lab environment. The prototype of foam-covered ESP is also sent to a nonprofit third party, RTI International, for a rigorous and impartial testing that follows ASHRAE standard. The collection efficiencies measured by RTI are satisfactory and agree with the in-house results. The pressure drop of foam-covered ESPs ranges from 10 Pa to 50 Pa, which is proportional to the free airflow velocity but independent from the dust loading. This means that the pressure drop of foam-covered ESPs remains unchanged at a given free airflow velocity regardless of the dust accumulations. Together with the high collection efficiency and low pressure drop, the foam-covered ESPs are concluded to be high-efficiency ESPs. Additionally, the ozone emission of foam-covered ESPs is reported to be lower than government and industrial standards.

Parametric studies are also conducted to show how the parameters of interest affect the

collection efficiency. Both experimental results and theoretical predictions show that the collection efficiency of foam-covered ESPs is proportional to the corona voltage and the repelling voltage, but is inversely proportional to the free airflow velocity. Higher corona voltage charges particles efficiently, while higher repelling voltage causes higher electric field strength between the repelling and collecting electrodes. Lower free airflow velocity, on the other hand, allows particles to stay in the airflow channel for a longer period of time. However, when the free airflow velocity is lower than a certain value, the chances of spark discharge in the charger increase because the corona current increases.

5.1.2 Guidance-Plate-Covered Electrostatic Precipitators

This dissertation also presents guidance-plate-covered ESPs, an alternative particle-trapping mechanism for ESPs. The perforated guidance plates are used to cover the collecting electrodes, but are also intentionally separated from the collecting electrodes by insulated spacers, creating gaps between the guidance plates and the collecting electrodes. Charged particles pass through the holes and settle in these gaps. There are fewer disturbances in the gaps than that on the flat surface of bare collecting electrodes, lowering the chances of particle re-entrainment. This mechanism allows accommodating greater amounts of particles and no consumable materials are used. The performance of guidance-plate-covered ESPs and traditional ESPs (bare collecting electrodes) are thoroughly discussed and compared.

The numerical modeling gives an overview of the flow field, electric field, and collection efficiency for guidance-plate-covered ESPs under different conditions such as free airflow

velocity, repelling voltage, and hole diameter. First, the flow velocity in the gaps between the guidance plate and collecting electrode is low, as expected, allowing particles to be easily captured by the electrostatic forces. The free airflow velocity and hole diameter have significant influence on the flow fields. Second, the electrical characteristics are affected only by both repelling voltage and hole diameter. The magnitude of the electric potential changes with both repelling voltage and hole diameter. The pattern of the electric field changes only with the hole diameter. Third, two dimensionless quantities, the Stoke numbers (the ratio of inertia force to viscous drag force) and the electrostatic numbers (the ratio of electrostatic force to viscous drag force), are used to interpret how they relates to the collection efficiency without discussing single parameters. Although the electrostatic number is a fraction of the Deutsch's number that has a direct influence on the collection, the Stoke number still plays an important role in determining the collection efficiency. A lower Stoke number and a higher electrostatic number result in a higher collection efficiency.

Particle re-entrainment is also numerically demonstrated. When particles dislodge from the collecting electrode, none of particles really re-enter the environment because the flow velocity inside the gaps is very low. When particles dislodge from the top surface of the guidance plate, most of particles enter the gaps and are recollected either by the flow recirculation or by the induced electrostatic forces because they regain some charges.

The experiments show that the collection efficiency of guidance-plate-covered ESPs is significantly higher than that of traditional ESPs regardless of operating conditions. The minimum difference of the collection efficiencies between guidance-plate-covered ESPs and

traditional ESPs is 2.9%, the maximum difference is 22.8%, and the average difference is 8.9%. Parametric studies of hole conditions conclude that a moderate diameter of holes is necessary to achieve a high collection efficiency. A considerably larger hole diameter loses the ability of trapping particles because of less cover. A considerably smaller hole diameter allows for only a limited amount of particles to enter the gaps between the guidance plates and collecting electrodes. Moreover, guidance-plate-covered ESPs with a higher hole density have higher collection efficiencies. Conversely, guidance-plate-covered ESPs with a relatively low hole density have a low collection efficiency, and can be as low as traditional ESPs have. The corona power of guidance-plate-covered ESPs is slightly higher than that of traditional ESPs, possibly because the pattern of electric field and the space charge density around the corona electrodes are altered such that the amounts of the electrons going to the corona electrodes are changed accordingly. The parametric studies show that the corona power increases when the free airflow velocity and the corona voltage increase, and when the repelling voltage decreases.

5.1.3 Key Energy Performance of Electrostatic Precipitators

This dissertation provides an impartial method of evaluating the performance of air filters by the key energy performance, which represents the collection efficiency per pressure drop. The electrostatic precipitators have shown significantly higher key energy performance than fiber-based filters because the pressure drop across electrostatic precipitators is much lower than that across fiber-based filters.

The key energy performance is proportional to the collection efficiency and inversely proportional to the pressure drop, however, these relationships are not linearly dependent to each other. The collection efficiency of ESPs is exponentially saturated with the corona voltage. When the collection efficiency of ESPs approaches a certain high level, further increases in the corona voltage do not improve the collection efficiency, but instead result in a significant increase in the corona power, decreasing the key energy performance of ESPs. Furthermore, through the statistical analysis, the corona voltage plays the most important role in determining the key energy performance of an ESP because the corona voltage is hardly responsible for the collection efficiency.

This dissertation also presents a comparison of the energy cost of using fiber-based filters and electrostatic precipitators in a real-life HVAC system. For the HVAC system in Loew Hall at the University of Washington, replacing the fiber-based filters with the foam-covered electrostatic precipitators saves up to 26.5% energy cost per unit airflow.

5.2 Future Work

This dissertation proves that the newly developed ESPs have a high collection efficiency and a low pressure drop. There are further efforts in research and commercialization fields that can be performed to successfully implement ESPs in a broader array of non-industrial applications.

5.2.1 Research

5.2.1.1 Theory and Modeling of Collection Efficiency

Previous chapters have discussed the theory of collection efficiency behind ESPs, including particle charging and particle kinetics. For the unconventional ESPs this dissertation focuses on, the existing theories of the collection efficiency are insufficiently accurate because of the lack of adequate theoretical models that describe the level of the particle charging and the rate of the particle re-entrainment.

The theory of the collection efficiency of ESPs is constructed based on the particle migration velocity that depends on the particle charging and electric field strength in the collector. For the ultra-fine particles that this dissertation concerns about, both field charging and diffusion charging play critical roles in determining the level of particle charging. Existing models of particle charging are based on the assumption that particles are fully charged, which is not so true in practice. A sophisticated particle charging model is thus required.

On the other hand, particle re-entrainment is also important in evaluating the collection efficiency of ESPs. When the adhesion between the collected particles and collecting electrodes is not strong enough, disturbances like passing airflow or vibrations dislodge those collected particles and make them re-enter the environment, thus lowering the collection efficiency. At a critical condition, particle re-entrainment can take the responsibility for lowering collection efficiency by up to 30% [73-75]. Experiments are the most common way used to determine the rate of particle re-entrainment. However, to date, there is no solid theory

that successfully and precisely predicts the rate of particle re-entrainment. The theory of particle re-entrainment is thus necessary to improve the accuracy of predicting the collection efficiency of ESPs.

5.2.1.2 Effects of Ionic Wind

ESPs are electrohydrodynamics-based air cleaners, and ionic wind is the product of the corona discharge. Depending on the design configuration, the ionic wind could generate "back pressure" to the ESP system, and have the potential to reduce the loading of the pumps that are used to bring air into and out of the system. As discussed in the previous chapters, the quality of the airflow is critical to the collection efficiency, especially for ultra-fine particles, because small particles track the flow field exactly. The existence of the ionic wind has an effect on the flow quality and makes theoretical predictions difficult. At certain conditions, the ionic wind can be neglected, depending on the magnitude of the ionic wind and how the ESP is designed. Figure 5.1 shows the theoretical predictions of the contribution of the ionic wind to an existing airflow velocity created by a rotary fan [6]. Note that the ionic wind generator is in series with the fan.

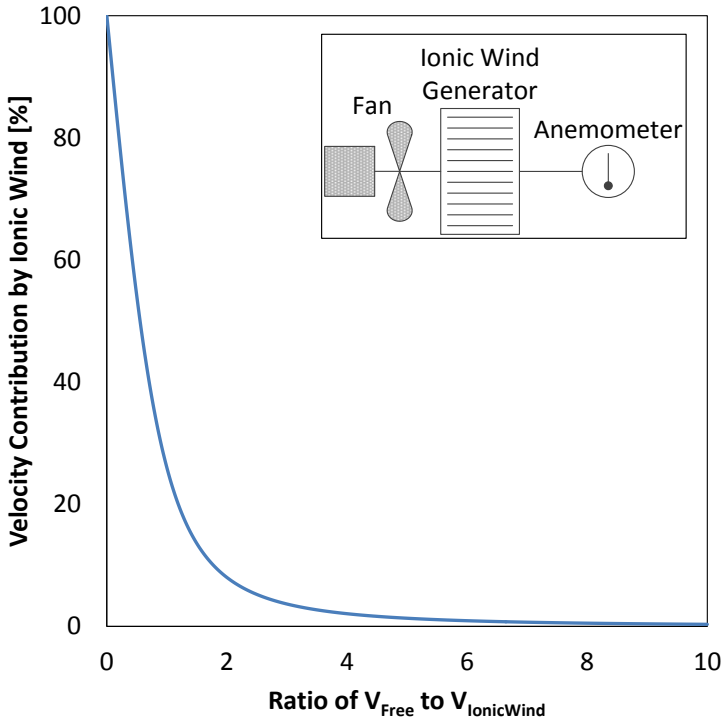

Figure 5.1: The theoretical resultant airflow velocity under different ratio of free air stream velocity to ionic wind velocity. V_{free} and $V_{IonicWind}$ are the free airflow velocity and the ionic wind velocity, respectively.

When the free airflow velocity is zero (i.e., fan is off), the resultant airflow velocity is completely contributed by the ionic wind. However, once there is a free airflow velocity (i.e., fan is on), the contribution of the ionic wind to the resultant airflow begins to decrease significantly. When the ionic wind velocity is identical to the free airflow velocity, the ionic wind contributes only 25% to the resultant velocity. Therefore, for an ESP, when the ratio of the free airflow velocity to the ionic wind velocity is high, the ionic wind is an important factor that may affect both experimental and theoretical work.

5.2.1.3 Other Topics

The potential environmental and health impact of applying ESPs in an HVAC system is the emission of ozone, a byproduct of corona discharge. At high concentrations, ozone is irritable and damaging [57-59]. The mitigation of ozone generation is important to the environment. Although ozone concentration of foam-covered ESPs is lower than governmental and industrial standards, it is still desirable to reduce ozone emission. The amount of ozone emissions is determined by several factors such as environmental conditions, particle properties, the physical properties of corona electrode, and the electrical operation conditions of ESPs [14, 38, 77-79]. One way to reduce ozone emission is to use proper material for the corona electrodes. Alternatively, particular catalysts are also commonly used to neutralize the ozone [80, 81]. Though these two methods are effective, they might be impractical because they are costly and have integration problems.

The degradation of corona electrode, including chemical erosions and contaminated deposits on the electrode surface, could lower the effectiveness of particle charging [84] and lower the collection efficiency. Reliability of the corona electrode and high voltage safety also need to be specially taken care of during the design stage.

5.2.2 Commercialization

5.2.2.1 Field Test

To fully characterize the performance of the newly developed ESPs presented in this dissertation, a field test is necessary in the future. The future plan is to conduct the test in room

212 of the Plant Operation Building at the University of Washington. Figure 5.2 shows the targeted space for the field test. The dimension of the chamber is 508 mm by 622 mm by 978 mm. Currently, there are two MERV 8 inclined back-to-back fiber-based filters installed in the chamber, as shown in Figure 5.3, and the dimension of each single filter is 406 mm by 508 mm by 50 mm. The unit price of each filter is $6. A replacement is required every three months.

The challenges involved in accomplishing the field test include ensuring the safety of all test vehicles, making sure the collection efficiency is high and reliable enough, and ensuring that all electrical connections are completely secured. Additionally, all sensors, including particle counters, fault detectors, and multimeters, should be properly mounted and can be remotely monitored. An emergency clutch that prevents any physical damages or injures should also be installed and specifically located for both on-site and remote researchers. This helps researchers evaluate the collection efficiency, longevity, stability, and reliability of these newly developed ESPs.

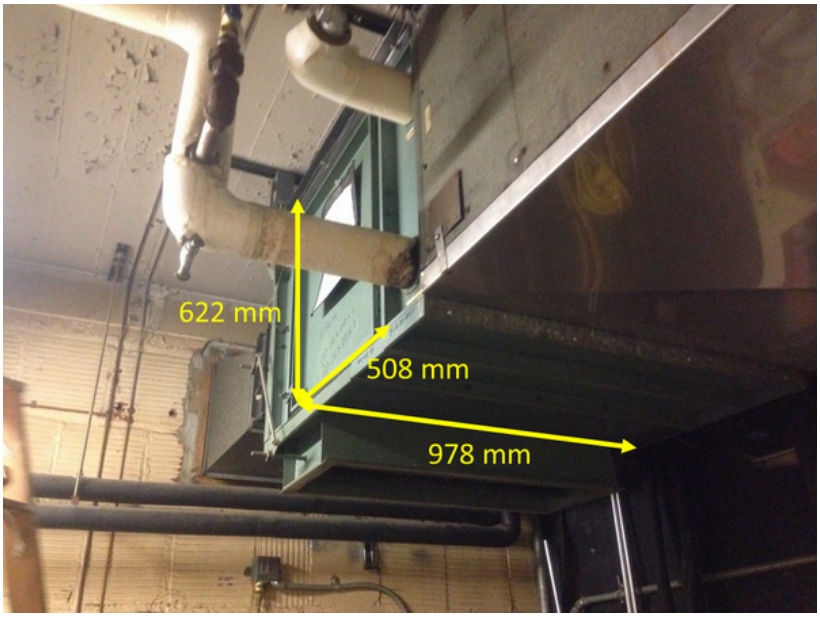

Figure 5.2: Dimension of the chamber that contains air filters.

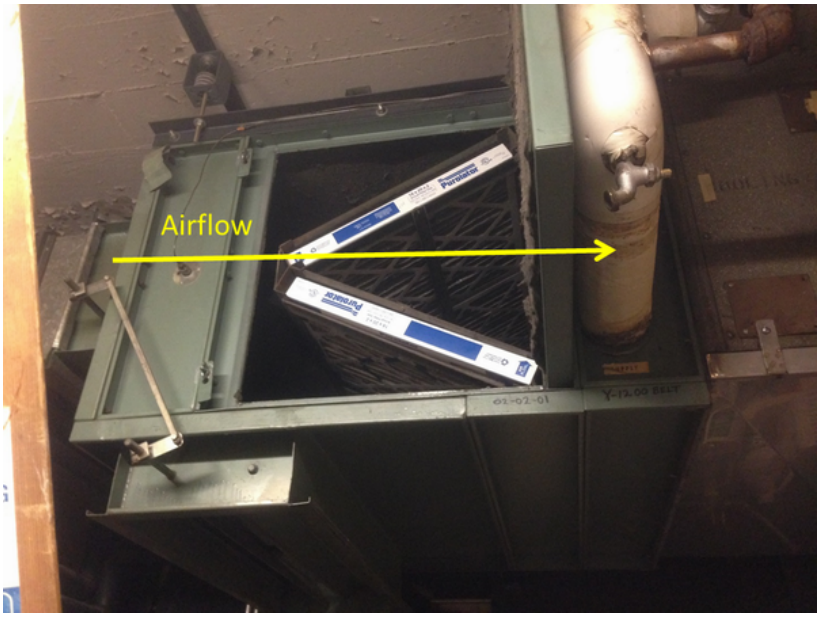

Figure 5.3: Two inclined back-to-back air filters installed in the chamber.

5.2.2.2 Optimization and Automatic Control

The collection efficiency and the pressure drop of ESPs are sensitive to the physical geometry and dimension. In regards to foam-covered ESPs, future work will focus on the properties of foam, such as pore size, porosity, thickness, and electrical conductivity. For guidance-plate-covered ESPs, the diameter of holes and the number of holes will be further optimized across wider range than it has discussed in the earlier chapter. The height of gaps is also a topic awaiting for explorations.

Foam-covered ESPs and guidance-plate-covered ESPs are active air filters. At a given physical geometry and dimension, the collection efficiency of these ESPs is a function of particle size, corona voltage, repelling voltage, and free airflow velocity, while the pressure drop is only dependent on the free airflow velocity. These characteristics provide a wide operating range that could be optimized based on the instantaneous environmental conditions. To maximize the collection capability for a dusty environment, free airflow velocity should be low, while corona and repelling voltages should be high. When the environment is clean, the operating conditions should be the other way around to save energy. This dissertation provides basic guidelines to optimize the collection efficiency and the energy efficiency. Sophisticated algorithms for the automatic control, to obtain the best collection and energy efficiencies, based on the feedbacks of the sensors installed in the environment are required in the process of commercialization.

BIBLIOGRAPHY

[1] I. Krichtafovitch, T. Y. Wen, and A. Mamishev, "Design of an Electronic Air Cleaner with Porous Collecting Electrodes," Proceedings of the 2013 ESA Annual Meeting on Electrostatics, pp. C5-1-8, 2013.

[2] T. Y. Wen, T. T. Shen, H. C. Wang, and A. Mamishev, "Optimization of Wire-Rod Electrostatic Fluid Accelerators," 2013 IEEE 63rd Electronic Components and Technology Conference, pp. 240-246, 2013.

[3] T. Y. Wen, H. C. Wang, I. Krichtafovitch, and A. V. Mamishev, "Novel Electrodes of an Electrostatic Precipitator for Air Filtration," Journal of Electrostatics, vol. 73, pp. 117-124, 2015.

[4] T. Y. Wen, I. Krichtafovitch, and A. V. Mamishev, "Reduction of Aerosol Particulates through the use of an ESP with Guidance-Plate-Covered Collecting Electrodes," Journal of Aerosol Science, vol. 79, pp. 40-47, 2015.

[5] T. Y. Wen, I. Krichtafovitch, and A. V. Mamishev, "The Key Energy Performance of Novel Electrostatic Precipitators," Journal of Building Engineering, vol. 2, pp. 77-84, 2015.

[6] T. Y. Wen, K. Lindgren, and A. V. Mamishev, "Electrostatic fluid accelerator under high-speed free air stream," Journal of Electrostatics, 2015, submitted.

[7] T. Y. Wen, I. Krichtafovitch, and A. V. Mamishev, "Numerical study of electrostatic precipitators with novel particle-trapping mechanism," Journal of Aerosol Science, 2015, submitted.

[8] G. A. Wellenius, M. R. Burger, B. A. Coull, J. Schwartz, H. H. Suh, P. Koutrakis, et al., "Ambient Air Pollution and the Risk of Acute Ischemic Stroke," Archives of Internal Medicine, vol. 172, pp. 229-234, 2012.

[9] M. Lippmann and R. E. Albert, "The effect of particle size on the regional deposition of inhaled aerosols in the human respiratory tract," American Industrial Hygiene Association Journal, vol. 30, pp. 257-275, 1969.

[10] R. D. Brook, S. Rajagopalan, C. A. Pope III, J. R. Brook, A. Bhatnagar, A. V. Diez-Roux, et al., "Particulate Matter Air Pollution and Cardiovascular Disease," Circulation, vol. 121, pp. 2331-2378, 2010.

[11] H. Nouri, N. Zouzou, E. Moreau, L. Dascalescu, and Y. Zebboudj, "Effect of relative humidity on current–voltage characteristics of an electrostatic precipitator," Journal of Electrostatics, vol. 70, pp. 20-24, 2012.

[12] A. Mizuno, "Electrostatic precipitation," IEEE Transactions on Dielectrics and Electrical Insulation, vol. 7, pp. 615-624, 2000.

[13] H. Umemoto, H. Hayashi, K. Takashima, and A. Mizuno, "Electrostatic precipitators for cleaning diesel exhaust," Industry Applications Society Annual Meeting, pp. 1-4, 2008.
[14] N. Cardello, J. Volckens, M. P. Tolocka, R. Wiener, and T. J. Buckley, "Technical Note: Performance of a Personal Electrostatic Precipitator Particle Sampler," Aerosol Science and Technology, vol. 36, pp. 162-165, 2002.
[15] J. S. Chang, "Next generation integrated electrostatic gas cleaning systems," Journal of Electrostatics, vol. 57, pp. 273-291, 2003.
[16] Y. Ehara, R. Nakano, T. Yamamoto, A. Zukeran, T. Inui, and H. Kawakami, "Performance of high velocity electrostatic precipitator for road tunnel," International Journal of Plasma Environmental Science and Technology, vol. 5, pp. 157-160, 2011.
[17] A. Farnoud, Electrostatic removal of diesel particulate matter: ProQuest, 2008.
[18] A. K. Sharma, H. Wallinb, and K. A. Jensen, "High volume electrostatic field-sampler for collection of fine particle bulk samples," Atmospheric Environment, vol. 41, pp. 369-381, 2007.
[19] T. Yamamoto and H. R. Velkoff, "Electrohydrodynamics in an electrostatic precipitator," Journal of Fluid Mechanics, vol. 108, pp. 1-18, 1981.
[20] T. T. Eighmy, J. D. Eusden, J. E. Krzanowski, D. S. Domingo, D. Staempfli, J. R. Martin, et al., "Comprehensive approach toward understanding element speciation and leaching behavior in municipal solid waste incineration electrostatic precipitator ash," Environmental Science and Technology, vol. 29, pp. 629-646, 1995.
[21] K. R. Parker, Applied electrostatic precipitation: Springer, 1996.
[22] W. Peukert and C. Wadenpohl, "Industrial separation of fine particles with difficult dust properties," Powder Technology, vol. 118, pp. 136-148, 2001.
[23] C. R. Mohanty, A. K. Swar, B. C. Meikap, and J. N. Sahu, "Studies on factors influencing fly ash resistivity from electrostatic precipitator with reference to India," Journal of Scientific and Industrial Research, vol. 70, pp. 795-803, 2011.
[24] D. A. Japuntich, "Respiratory Particulate Filtration," Journal of the International Society for Respiratory Protection, vol. 2, pp. 137-169, 1984.
[25] ASHRAE, "Method of Testing General Ventilation Air-Cleaning Devices for Removal Efficiency by Particle Size," ANSI/ASHRAE Addendum b to ANSI/ASHRAE Standard 52.2, 2008.
[26] ASHRAE, "Ventilation for Acceptable Indoor Air Quality," ANSI/ASHRAE Standard 62.1, 2013.
[27] ASME, "Code on Nuclear Air and Gas Treatment," American Society of Mechanical Engineers AG-1-2003, 2003.
[28] M. Jedrusik and A. Swierczok, "The influence of unburned carbon particles on electrostatic precipitator collection efficiency," 13th International Conference on Electrostatics, 2011.
[29] R. Meij and B. Te Winkel, "The emissions and environmental impact of PM10 and trace elements from a modern coal-fired power plant equipped with ESP and wet FGD,"

Fuel Processing Technology, vol. 85, pp. 641-656, 2004.
[30] V. Prabhu, S. Lee, and H. L. Clack, "Electrostatic precipitation of powdered activated carbon and implications for secondary mercury adsorption within electrostatic precipitators," Energy and Fuels, vol. 25, pp. 1010-1016, 2011.
[31] M. Jedrusik, J. B. Gajewski, and A. J. Swierczok, "Effect of the particle diameter and corona electrode geometry on the particle migration velocity in electrostatic precipitators," Journal of Electrostatics, vol. 51-52, pp. 245-251, 2001.
[32] J. Podlinski, J. Dekowski, J. Mizeraczyk, D. Brocilo, K. Urashima, and J. S. Chang, "EHD flow in a wide electrode spacing spike-plate electrostatic precipitator under positive polarity," Journal of Electrostatics, vol. 64, pp. 498-505, 2006.
[33] Y. N. Chun, J. S. Chang, A. A. Berezin, and J. Mizeraczyk, "Numerical modeling of near corona wire electrohydrodynamic flow in a wire-plate electrostatic precipitator," IEEE Transactions on Dielectrics and Electrical Insulation, vol. 14, pp. 119-124, 2007.
[34] E. Moreau and G. Touchard, "Enhancing the mechanical efficiency of electric wind in corona discharges," Journal of Electrostatics, vol. 66, pp. 39-44, 2008.
[35] N. V. P. R. Durga Prasad, T. Lakshminarayana, J. R. K. Narasimham, T. M. Verman, and C. S. R. Krishnam Raju, "Automatic control and management of electrostatic precipitator," IEEE Transactions on Industry Applications, vol. 35, pp. 561-567, 1999.
[36] G. N. Popa, C. Abrudean, S. I. Deaconu, I. Popa, and V. Vaida, "A Case Study of ESP Electrical Characteristics from a Thermal Power Station," IEEE Industry Applications Society Annual Meeting, pp. 1-6, 2009.
[37] I. Kiss and I. Berta, "New concept of ESP modelling based on fuzzy logic," Journal of Electrostatics, vol. 51, pp. 206-211, 2001.
[38] K. Yanallah, F. Pontiga, A. Fernandez-Rueda, A. Castellanos, and A. Belasri, "Ozone generation using negative wire-to-cylinder corona discharge: The influence of anode composition and radius," Annual Report Conference on Electrical Insulation and Dielectric Phenomena, pp. 607-610, 2008.
[39] A. S. Viner, P. A. Lawless, D. S. Ensor, and L. E. Sparks, "Ozone generation in DC-energized electrostatic precipitators," IEEE Transactions on Industry Applications, vol. 28, pp. 504-512, 1992.
[40] J. S. Chang, P. A. Lawless, and T. Yamamoto, "Corona Discharge Processes," IEEE Transactions on Plasma Science, vol. 19, pp. 1152-1166, 1991.
[41] S. Oglesby and G. B. Nichols, Electrostatic precipitation: M. Dekker, 1978.
[42] R. J. Bedmutha, L. Ferrante, C. Briens, F. Berruti, and I. Inculet, "Single and two-stage electrostatic demisters for biomass pyrolysis application," Chemical Engineering and Processing: Process Intensification, vol. 48, pp. 1112-1120, 2009.
[43] G. W. Penney, "Adhesive behavior of dust in electrostatic precipitation," Journal of the Air Pollution Control Association, vol. 25, pp. 113-117, 1975.
[44] G. Y. Lin, C. J. Tsai, S. C. Chen, T. M. Chen, and S. N. Li, "An efficient single-stage wet electrostatic precipitator for fine and nanosized particle control," Aerosol Science

and Technology, vol. 44, pp. 38-45, 2010.
[45] D. J. Bayless, M. K. Alam, R. Radcliff, and J. Caine, "Membrane-based wet electrostatic precipitation," Fuel Processing Technology, vol. 85, pp. 781-798, 2004.
[46] A. Jaworek, W. Balachandran, A. Krupa, J. Kulon, and M. Lackowski, "Wet electroscrubbers for state of the art gas cleaning," Environmental Science and Technology, vol. 40, pp. 6197-6207, 2006.
[47] H. J. Kim, B. Han, Y. J. Kim, K. D. Hwang, W. S. Oh, S. Y. Yoo, et al., "Fine particle removal performance of a two-stage wet electrostatic precipitator using a nonmetallic pre-charger," Journal of the Air and Waste Management Association, vol. 61, pp. 1334-1343, 2011.
[48] L. C. Lynnworth, R. Cohen, J. L. Rose, J. O. Kim, and E. R. Furlong, "Vortex shedder fluid flow sensor," IEEESensors Journal, vol. 6, pp. 1488-1496, 2006.
[49] H. J. White, Industrial electrostatic precipitation: Addison-Wesley, 1963.
[50] http://www.hamon.com/en/air-quality-systems/products/dust-emission-control/dry-wet-esp-s/.
[51] S. Masuda and J. D. Moon, "Electrostatic precipitation of carbon soot from diesel engine exhaust," IEEE Transactions onIndustry Applications, vol. 6, pp. 1104-1111, 1983.
[52] UnderwritersLaboratories, "Standard 867 for Electrostatic Air Cleaners," ANSI/UL 867, 2007.
[53] F. W. Peek, Dielectric Phenomena in High Voltage Engineering: McGraw-Hill, 1929.
[54] Y. Yoshioka, "Recent developments in plasma De-NOx and PM (particulate matter) removal technologies from diesel exhaust gases," International Journal of Plasma Environmental Science and Technology, vol. 1, pp. 1-13, 2007.
[55] A. Jaworek, M. Jedrusik, A. Swierczok, T. Czech, A. T. Sobczyk, and M. Lackowski, "Biomass co-firing. New challenge for electrostatic precipitators," International Journal of Plasma Environmental Science and Technology, vol. 5, pp. 161-167, 2011.
[56] S. Kanazawa, T. Ohkubo, Y. Nomoto, T. Adachi, and J. S. Chang, "Simultaneous measurements of wire electrode surface contamination and corona discharge characteristics in an air-cleaning electrostatic precipitator," IEEE Transactions onIndustry Applications, vol. 33, pp. 279-285, 1997.
[57] C. J. Weschler, "Ozone in indoor environments: concentration and chemistry," Indoor Air, vol. 10, pp. 269-288, 2000.
[58] J. A. Bernstein, N. Alexis, H. Bacchus, I. L. Bernstein, P. Fritz, E. Horner, et al., "The health effects of nonindustrial indoor air pollution," Journal of Allergy and Clinical Immunology, vol. 121, pp. 585-591, 2008.
[59] R. B. Devlin, W. F. McDonnell, R. Mann, S. Becker, D. E. House, D. Schreinemachers, et al., "Exposure of humans to ambient levels of ozone for 6.6 hours causes cellular and biochemical changes in the lung," American Journal of Respiratory Cell and Molecular Biology, vol. 4, pp. 72-81, 1991.
[60] C. Jakober and T. Phillips, "Evaluation of Ozone Emissions From Portable Indoor Air

Cleaners: Electrostatic Precipitators and Ionizers," California Environmental Protection Agency, 2008.

[61] EPA, "National Ambient Air Quality Standards for Ozone," Environmental Protection Agency, vol. 73, pp. 16436-16514, 2008.

[62] D. M. Drechsler, C. Garcia, H. Tran, A. Mehadi, M. Nystrom, R. Propper, et al., "Review of the California Ambient Air Quality Standard For Ozone," California Environmental Protection Agency, 2005.

[63] FDA, "Code of Federal Regulations Title 21," Food and Drug Administration, vol. 8, 2013.

[64] CDC, "NIOSH Pocket Guide to Chemical Hazards," DHHS (NIOSH) Publication No. 2005-149, 2007.

[65] M. Alonso, M. I. Martin, and F. J. Alguacil, "The measurement of charging efficiencies and losses of aerosol nanoparticles in a corona charger," Journal of Electrostatics, vol. 64, pp. 203-214, 2006.

[66] D. R. Chen and D. Y. H. Pui, "A high efficiency, high throughput unipolar aerosol charger for nanoparticles," Journal of Nanoparticle Research, vol. 1, pp. 115-126, 1999.

[67] W. C. Hinds, Aerosol Technology: Properties, Behavior, and Measurement of Airborne Particles, 2 ed.: Wiley-Interscience, 1999.

[68] S. H. Kim and K. W. Lee, "Experimental study of electrostatic precipitator performance and comparison with existing theoretical prediction models," Journal of Electrostatics, vol. 48, pp. 3-25, 1999.

[69] T. Ferge, J. Maguhn, H. Felber, and R. Zimmermann, "Particle Collection Efficiency and Particle Re-entrainment of an Electrostatic Precipitator in a Sewage Sludge Incineration Plant," Environmental Science and Technology, vol. 38, pp. 1545-1553, 2004.

[70] A. Zukeran, Y. Ikeda, Y. Ehara, M. Matsuyama, T. Ito, T. Takahashi, et al., "Two-stage-type electrostatic precipitator re-entrainment phenomena under diesel flue gases," IEEE Transactions onIndustry Applications, vol. 35, pp. 346-351, 1999.

[71] T. Yamamoto, M. Mieno, K. Shibata, and K. Sakai, "Studies of rapping reentrainment from electrostatic precipitators," Proceeding of 7th Intertional Conference on Electrostatic Precipitation, pp. 163-170, 1998.

[72] X. Zhang, L. Wang, and K. Zhu, "Particle tracking and particle-wall collision in a wire-plate electrostatic precipitator," Journal of Electrostatics, vol. 63, pp. 1057-1071, 2005.

[73] A. Jaworek, A. Krupa, and T. Czech, "Modern electrostatic devices and methods for exhaust gas cleaning: A brief review," Journal of Electrostatics, vol. 65, pp. 133-155, 2007.

[74] J. R. Melcher, K. S. Sachar, and E. P. Warren, "Overview of electrostatic devices for control of submicrometer particles," Proceedings of the IEEE, vol. 65, pp. 1659-1669, 1977.

[75] Y. Zhuang, Y. J. Kim, T. G. Lee, and P. Biswas, "Experimental and theoretical studies of ultra-fine particle behavior in electrostatic precipitators," Journal of Electrostatics, vol. 48, pp. 245-260, 2000.

[76] H. S. Nelson, S. R. Hirsch, J. L. Ohman Jr, T. A. E. Platts-Mills, C. E. Reed, and W. R. Solomon, "Recommendations for the use of residential air-cleaning devices in the treatment of allergic respiratory diseases," Journal of Allergy and Clinical Immunology, vol. 82, pp. 661-669, 1988.

[77] S. H. Huang and C. C. Chen, "Loading characteristics of a miniature wire-plate electrostatic precipitator," Aerosol Science and Technology, vol. 37, pp. 109-121, 2003.

[78] K. J. Boelter and J. H. Davidson, "Ozone generation by indoor, electrostatic air cleaners," Aerosol Science and Technology, vol. 27, pp. 689-708, 1997.

[79] C. F. Gallo and G. S. P. Castle, "Parametric study of ozone generation by coronas," IEEE Transactions onIndustry Applications, vol. IA-14, pp. 84-86, 1978.

[80] J. N. Armor, "Environmental catalysis," Applied Catalysis B: Environmental, vol. 1, pp. 221-256, 1992.

[81] H. H. Kim, "Nonthermal Plasma Processing for Air-Pollution Control: A Historical Review, Current Issues, and Future Prospects," Plasma Processes and Polymers, vol. 1, pp. 91-110, 2004.

[82] R. S. Islamov and Y. A. Krishtafovich, "A peculiarity of silver-based corona wire heating on ozone generation," Journal of Electrostatics, vol. 69, pp. 236-239, 2011.

[83] T. Ohkubo, S. Hamasaki, Y. Nomoto, J. S. Chang, and T. Adachi, "The effect of corona wire heating on the downstream ozone concentration profiles in an air-cleaning wire-duct electrostatic precipitator," IEEE Transactions on Industry Applications, vol. 26, pp. 542-549, 1990.

[84] N. E. Jewell-Larsen, E. Tran, I. A. Krichtafovitch, and A. V. Mamishev, "Design and optimization of electrostatic fluid accelerators," IEEE Transactions on Dielectrics and Electrical Insulation, vol. 13, pp. 191-203, 2006.

[85] W. Deutsch, "Bewegung und Ladung der Elektrizittstrger im Zylinderkondensator," Annalen der Physik, vol. 373, pp. 335-344, 1922.

[86] G. Leonard, M. Mitchner, and S. A. Self, "Particle transport in electrostatic precipitators," Atmospheric Environment, vol. 14, pp. 1289-1299, 1980.

[87] P. Cooperman, "A new theory of precipitator efficiency," Atmospheric Environment (1967), vol. 5, pp. 541-551, 1971.

[88] X. Zhang, L. Wang, and K. Zhu, "An analysis of a wire-plate electrostatic precipitator," Journal of Aerosol Science, vol. 33, pp. 1595-1600, 2002.

[89] G. W. Hewitt, "The charging of small particles for electrostatic precipitation," Transactions of the American Institute of Electrical Engineers, vol. 76, pp. 300-306, 1957.

[90] W. B. Smith and J. R. McDonald, "Calculation of the charging rate of fine particles by unipolar ions," Journal of the Air Pollution Control Association, vol. 25, pp. 168-172, 1975.

[91] W. B. Smith and J. R. McDonald, "Development of a theory for the charging of particles

by unipolar ions," Journal of Aerosol Science, vol. 7, pp. 151-166, 1976.
[92] A. Bologa, H. R. Paur, H. Seifert, T. Wascher, and K. Woletz, "Novel wet electrostatic precipitator for collection of fine aerosol," Journal of Electrostatics, vol. 67, pp. 150-153, 2009.
[93] A. M. Bologa, H. R. Paur, H. Seifert, and T. Wascher, "Pilot-plant testing of a novel electrostatic collector for submicrometer particles," IEEE Transactions on Industry Applications, vol. 41, pp. 882-890, 2005.
[94] D. J. Bayless, H. Pasic, M. K. Alam, L. Shi, B. Haynes, J. Cochran, et al., "Use of membrane collectors in electrostatic precipitators," Journal of the Air and Waste Management Association, vol. 51, pp. 1401-1407, 2001.
[95] D. J. Bayless, L. Shi, G. Kremer, B. J. Stuart, J. Reynolds, and J. Caine, "Membrane-based wet electrostatic precipitation," Journal of the Air and Waste Management Association, vol. 55, pp. 784-791, 2005.
[96] T. Misaka, A. Akasaka, H. Yabuta, T. Oura, T. Hirano, M. Yamazaki, et al., "Recent applications of moving electrode type electrostatic precipitator," 7th International Conference on Electrostatic Precipitation, pp. 20-25, 1998.
[97] T. Misaka, T. Oura, and M. Yamazaki, "Improvement of reliability for moving electrode type electrostatic precipitator," 10th International Conference on Electrostatic Precipitation, 2006.
[98] T. Misaka and Y. Mochizuki, "Recent application and running cost of moving electrode type electrostatic precipitator," 11th International Conference on Electrostatic Precipitation, pp. 518-522, 2009.
[99] H. Ando, N. Shiromaru, and Y. Mochizuki, "Recent Technology of Moving Electrode Electrostatic Precipitator," International Journal of Plasma Environmental Science and Technology, vol. 5, pp. 130-134, 2011.
[100] S. Chen and X. Chen, "Electrostatic lentoid precipitator and its performance," 7th International Conference on Electrostatic Precipitation, 1998.
[101] Y. Lin and W. Liu, "Development of Chinese Electrostatic Precipitator Technology," 11th International Conference on Electrostatic Precipitation, 2010.
[102] T. Yamamoto, T. Abe, T. Mimura, N. Otsuka, Y. Ito, Y. Ehara, et al., "Electrohydrodynamically assisted electrostatic precipitator for the collection of low-resistivity dust," IEEE Transactions on Industry Applications, vol. 45, pp. 2178-2184, 2009.
[103] F. Hauksbee, "Physico-Mechanical Experiments on Various Subjects," pp. 46-47, 1709.
[104] B. Wilson, "Treatise on Electricity," pp. 140-141, 1750.
[105] T. Cavallo, A complete treatise of electricity in theory and practice; with original experiments. London: Edward and Charles Dilly, 1777.
[106] M. Faraday, Experimental Researches in Electricity: Philosophical Transactions, 1839.
[107] A. P. Chattock, "On the velocity and mass of the ions in the electric wind in air," Philosophical Magazine Series 5, vol. 48, pp. 401-420, 1899.
[108] A. Castellanos, A. Ramos, A. Gonzalez, N. G. Green, and H. Morgan, "Electrohydrodynamics and dielectrophoresis in microsystems: scaling laws," Journal of Physics D:

Applied Physics, vol. 36, pp. 2584-2597, 2003.
[109] v. R. Helmholtz, Ann. Physik, vol. 32, pp. 1-19, 1887.
[110] O. J. Lodge, "On the Sudden Acquisition of Conducting-Power by a Series of Discrete Metallic Particles," Proceeding of the Physical Society of London, p. 461, 1893.
[111] G. S. P. Castle, "Industrial applications of electrostatics: the past, present and future," Journal of Electrostatics, vol. 51-52, pp. 1-7, 2001.
[112] D. K. Louie, Handbook of Sulphuric Acid Manufacturing. Ontario, Canada: DKL Engineering, Inc., 2005.
[113] H. D. Goodfellow and E. Tahti, Industrial Ventilation Design Guidebook: Academic Press, 2001.
[114] A. Buekens, "Electrostatic Precipitators," Pollution Control Technologies, vol. 1.
[115] G. E. Moore, "Cramming more components onto integrated circuits," Electronics, vol. 38, 1965.
[116] G. E. Moore, "Progress in digital integrated electronics," IEDM Technical Digest, vol. 11, 1975.
[117] R. A. Moss and J. Grey, "Heat Transfer Augmentation by Steady and Alternating Electric Field," Proceeding of Heat Transfer and Fluid Mechanics Institute, pp. 210-235, 1966.
[118] F. Yang, N. E. Jewell-Larsen, D. L. Brown, D. A. Parker, K. A. Pendergrass, I. A. Krichtafovitch, et al., "Corona Driven Air Propulsion for Cooling of Electronics," International Symposium on High Voltage Engineering, 2003.
[119] N. E. Jewell-Larsen, H. Ran, Y. Zhang, M. Schwiebert, K. A. Honer, and A. V. Mamishev, "Electrohydrodynamic (EHD) Cooled Laptop," 25th Semiconductor Thermal Measurement and Management Symposium, pp. 261-266, 2009.
[120] T. T. Brown, "A Method of and an Apparatus or Machine for Producing Force or Motion," US Patent 2,949,550, 1928.
[121] M. Martinez-Sanchez and J. E. Pollard, "Spacecraft electric propulsion - an overview," Journal of Propulsion and Power, vol. 14, pp. 688-699, 1998.
[122] L. Pekker and M. Young, "Model of ideal electrohydrodynamic thruster," Journal of Propulsion and Power, vol. 27, pp. 786-792, 2011.
[123] T. T. Brown, "Electrokinetic apparatus," ed, 1960.
[124] E. A. Christenson and P. S. Moller, "Ion-neutral propulsion in atmospheric media," AIAA Journal, vol. 5, pp. 1768-1773, 1967.
[125] H. S. Poon, M. K. K. Lam, M. Chow, and W. J. Li, "Noiseless and vibration-free ionic propulsion technology for indoor surveillance blimps," IEEE International Conference onRobotics and Automation, pp. 2891-2896, 2009.
[126] M. J. Stepaniak, F. V. Graas, and M. U. De Haag, "Design of an electric propulsion system for a quadrotor unmanned aerial vehicle," Journal of Aircraft, vol. 46, pp. 1050-1058, 2009.
[127] D. M. Goebel and I. Katz, Fundamentals of electric propulsion: ion and Hall thrusters vol. 1: John Wiley and Sons, 2008.

[128] N. A. Kaptsov, "Elektricheskie Yavvleniya Gazakh i Vakuume," 1947.
[129] K. Nashimoto, "The effects of electrode materials on O3 and NOx emissions by corona discharging," Journal of Imaging Science, vol. 32, pp. 205-210, 1988.
[130] J. S. E. Townsend, Electricity in gases: Clarendon Press, 1915.
[131] F. M. White, Fluid Mechanics, 7 ed.: McGraw-Hill, 2011.
[132] G. L. Leonard, M. Mitchner, and S. A. Self, "Experimental study of the effect of turbulent diffusion on precipitator efficiency," Journal of Aerosol Science, vol. 13, pp. 271-284, 1982.
[133] T. Lucke and H. Fissan, "The prediction of filtration performance of high efficiency gas filter elements," Chemical Engineering Science, vol. 51, pp. 1199-1208, 1996.
[134] M. Mayer, T. Caesar, and J. Klaus, "Energy efficiency classification of air filters," Proceeding of 10th World Filtration Congress, vol. 3, pp. 313-317, 2008.
[135] J. F. Montgomerya, S. I. Green, S. N. Rogak, and K. Bartlett, "Predicting the energy use and operation cost of HVAC air filters," Energy and Buildings, vol. 47, pp. 643-650, 2012.
[136] C. Sun and D. Woodman, "Delivering Sustainability Promise to HVAC Air Filtration - Part I: Classification of Energy Efficiency for Air Filters," ASHRAE Transactions, vol. 115, 2009.
[137] W. J. Fisk, D. Faulkner, J. Palonen, and O. Seppanen, "Performance and costs of particle air filtration technologies," Indoor Air, vol. 12, pp. 223-234, 2002.
[138] C. Strock and R. L. Koral, Handbook of Air Conditioning Heating and Ventilating. New York: The Industrial Press, 1965.
[139] Q. Lancereau, J. M. Roux, and J. L. Achard, "Influence of secondary flows on the collection efficiency of a cylindrical electrostatic precipitator," Journal of Aerosol Science, vol. 63, pp. 146-160, 2013.
[140] V. C. Liu, "Turbulent dispersion of dynamic particles," Journal of Meteorology, vol. 13, pp. 399-405, 1956.
[141] D. A. Drew, "A turbulent dispersion model for particles or bubbles," Journal of Engineering Mathematics, vol. 41, pp. 259-274, 2001.
[142] J. K. Lee, J. H. Ku, J. E. Lee, S. H. Kim, Y. C. Ahn, J. H. Shin, et al., "An experimental study of electrostatic precipitator plate rapping and re-entrainment," Proceedings of ICESP II, 1998.
[143] A. A. Economopoulou and R. M. Harrison, "Methodology for Performance Evaluation of Dust Control Systems with an Application to Electrostatic Precipitators," Aerosol Science and Technology, vol. 42, pp. 842-853, 2008.
[144] J. H. Vincent and A. S. M. MacLennan, "Aerodynamic considerations in electrostatic precipitation," Journal of Electrostatics, vol. 8, pp. 325-342, 1980.

Appendix A

NONDIMENSIONALIZED GOVERNING EQUATIONS OF ELECTROHYDRODYNAMICS

To nondimensionalize the governing equations of electrohydrodynamic shown in 2.3.4, the asterisk denotes the nondimensional quantities, and bold fonts are used for vectors or tensors.

$$V^* = \frac{V}{V_0} \tag{A.1}$$

$$\mathbf{U}^* = \frac{\mathbf{U}}{U_0} \tag{A.2}$$

$$x^* = \frac{x}{L_0} \tag{A.3}$$

$$y^* = \frac{y}{L_0} \tag{A.4}$$

$$q^* = \frac{q}{q_0} \tag{A.5}$$

$$p^* = \frac{p}{p_0} \tag{A.6}$$

where V_0, U_0, L_0, q_0, and p_0 are the characteristic entities for electric potential, velocity, length, charge density, and pressure, respectively. For the gradient of potential,

$$\begin{cases} \dfrac{\partial V}{\partial x} = \dfrac{\partial V}{\partial x^*}\dfrac{\partial x^*}{\partial x} = \dfrac{V_0 \partial V^*}{\partial x^*}\dfrac{\partial x^*}{\partial x} = \dfrac{V_0}{L_0}\dfrac{\partial V^*}{\partial x^*} \\ \dfrac{\partial V}{\partial y} = \dfrac{\partial V}{\partial y^*}\dfrac{\partial y^*}{\partial y} = \dfrac{V_0 \partial V^*}{\partial y^*}\dfrac{\partial y^*}{\partial y} = \dfrac{V_0}{L_0}\dfrac{\partial V^*}{\partial y^*} \end{cases} \tag{A.7}$$

$$\nabla V = \frac{V_0}{L_0}\nabla V^* \tag{A.8}$$

similarly, for velocity, charge density, and pressure,

$$\nabla \mathbf{U} = \frac{U_0}{L_0}\nabla \mathbf{U}^* \tag{A.9}$$

$$\nabla q = \frac{q_0}{L_0}\nabla q^* \tag{A.10}$$

$$\nabla p = \frac{p_0}{L_0}\nabla p^* \tag{A.11}$$

For the divergence of gradient for potential,

$$\begin{cases} \dfrac{\partial^2 V}{\partial x^2} = \dfrac{\partial}{\partial x}\dfrac{\partial V}{\partial x} = \dfrac{V_0}{L_0}\dfrac{\partial}{\partial x}\dfrac{\partial V^*}{\partial x^*} = \dfrac{V_0}{L_0}\dfrac{\partial V^*}{\partial x^*}\dfrac{\partial}{\partial x^*}\dfrac{\partial x^*}{\partial x} = \dfrac{V_0}{L_0^2}\dfrac{\partial^2 V^*}{\partial x^{*2}} \\ \dfrac{\partial^2 V}{\partial y^2} = \dfrac{\partial}{\partial y}\dfrac{\partial V}{\partial y} = \dfrac{V_0}{L_0}\dfrac{\partial}{\partial y}\dfrac{\partial V^*}{\partial y^*} = \dfrac{V_0}{L_0}\dfrac{\partial V^*}{\partial y^*}\dfrac{\partial}{\partial y^*}\dfrac{\partial y^*}{\partial y} = \dfrac{V_0}{L_0^2}\dfrac{\partial^2 V^*}{\partial y^{*2}} \end{cases} \tag{A.12}$$

$$\nabla^2 V = \frac{V_0}{L_0^2}\nabla^2 V^* \tag{A.13}$$

similarly, for velocity,

$$\nabla^2 \mathbf{U} = \frac{U_0}{L_0^2}\nabla^2 \mathbf{U}^* \tag{A.14}$$

Thus, rewrite the Poisson's equation,

$$\nabla^2 V = -\frac{q}{\varepsilon_0} \tag{A.15}$$

$$\frac{V_0}{L_0^2}\nabla^2 V^* = -\frac{q_0}{\varepsilon_0} q^* \tag{A.16}$$

$$\nabla^2 V^* = -\frac{q_0 L_0^2}{\varepsilon_0 V_0} q^* \tag{A.17}$$

once $q_0 = \dfrac{\varepsilon_0 V_0}{L_0^2}$, the Poisson's equation becomes nondimensional form as

$$\nabla^2 V^* = -q^* \tag{A.18}$$

For the charge transport equation,

$$-\nabla \cdot (\mu_E \nabla V q + D \nabla q) + \mathbf{U} \cdot \nabla q = 0 \tag{A.19}$$

$$-\frac{1}{L_0}\nabla \cdot \left(\mu_E \frac{V_0}{L_0}\nabla V^* q_0 q^* + D\frac{q_0}{L_0}\nabla q^*\right) + U_0 \mathbf{U}^* \cdot \frac{q_0}{L_0}\nabla q^* = 0 \tag{A.20}$$

$$-\nabla \cdot \left(\nabla V^* q^* + \frac{D}{\mu_E V_0}\nabla q^*\right) + \frac{L_0 U_0}{\mu_E V_0}\mathbf{U}^* \cdot \nabla q^* = 0 \tag{A.21}$$

$$-\nabla \cdot \left(\nabla V^* q^* + \frac{1}{Pe_E}\nabla q^*\right) + Re_E \mathbf{U}^* \cdot \nabla q^* = 0 \tag{A.22}$$

where the electric Peclet number, $Pe_E = \dfrac{\mu_E V_0}{D}$, and the electric Reynold's number $Re_E = \dfrac{L_0 U_0}{\mu_E V_0}$.

For the Navier-Stoke's equations in dimensionless form,

$$\rho \mathbf{U} \cdot \nabla \mathbf{U} = -\nabla p + \mu \nabla^2 \mathbf{U} - q \nabla V \tag{A.23}$$

$$\rho U_0 \mathbf{U}^* \cdot \frac{U_0}{L_0}\nabla \mathbf{U}^* = -\frac{p_0}{L_0}\nabla p^* + \mu \frac{U_0}{L_0^2}\nabla^2 \mathbf{U}^* - q_0 q^* \frac{V_0}{L_0}\nabla V^* \tag{A.24}$$

$$\mathbf{U}^* \cdot \nabla \mathbf{U}^* = -\frac{p_0}{\rho U_0^2}\nabla p^* + \frac{\mu}{\rho L_0 U_0}\nabla^2 \mathbf{U}^* - \frac{q_0 V_0}{\rho U_0^2} q^* \nabla V^* \tag{A.25}$$

In order to have coefficient in first term of right hand side of (A.25) as one, letting $p_0 = \rho U_0^2$. By substituting $q_0 = \dfrac{\varepsilon_0 V_0}{L_0^2}$,

$$\mathbf{U}^* \cdot \nabla \mathbf{U}^* = -\nabla p^* + \frac{1}{Re}\left(\nabla^2 \mathbf{U}^* - St_E q^* \nabla V^*\right) \tag{A.26}$$

where the Reynold's number, $Re = \dfrac{\rho L_0 U_0}{\mu}$, and the electric Stoke number, $St_E = \dfrac{\varepsilon_0 V_0^2}{\mu L_0 U_0}$. The continuity equation of flow in dimensionless form is,

$$\nabla \cdot \mathbf{U} = \frac{U_0}{L_0} \nabla \cdot \mathbf{U}^* = 0 \tag{A.27}$$

$$\nabla \cdot \mathbf{U}^* = 0 \tag{A.28}$$

Appendix B

NOMENCLATURE

$A_{boundary}$: cross sectional area of airflow boundary layer

$A_{channel}$: cross sectional area of airflow channel

A_c: surface area of collecting electrode

ΔA_c: increment of collecting area

b: ion mobility

BHp: brake horsepower

c: constant

C: particle concentration

ΔC: concentration of removed particle

C_c: Cunningham slip correction factor

C_{energy}: energy cost

C_{filter}: cost of filters

C_{in}: particle concentration at inlet

C_{labor}: labor cost of filter installation

C_μ: constant

C_{out}: particle concentration at outlet

C_{retail}: retail price of electricity

$C_{unitflow}$: cost per unit of airflow

δ_{ij}: Kronecker delta

$\Delta\delta$: thickness of boundary layer (in a specific time interval)

d_p: particle diameter

D: diffusivity coefficient of ions

D_1: particle diffusion coefficient in direction of airflow (longitudinal)

D_2: particle diffusion coefficient perpendicular to airflow (transverse)

D_t: turbulent diffusivity

D_B: Brownian diffusivity

ε: dissipation rate

ε_0: permittivity of free space

ε_p: relative permittivity of particles

e: elementary charge

E: electric field strength in the charger

E_0: breakdown electric strength of air

E_c: characteristic electric field strength

E_{cr}: electric field strength in the charger

Es: electrostatic number

$\mathbf{E}$: electric field

η: collection efficiency

$\eta_{cooperman}$: Cooperman's collection efficiency

$\eta_{deutsch}$: Deutsch's collection efficiency

η_{filter}: average collection efficiency of the EN779 test with 0.4 µm particles at 0.94 m^3/s

η_{system}: energy efficiency of the system

η_{zhang}: Zhang's collection efficiency

f: friction factor

$\mathbf{f}$: body force

h: width of the airflow channel

$\mathbf{J}$: current density

k: turbulent kinetic energy

kep: key energy performance

K: Boltzmann constant

$\overline{\lambda}$: mean free path of gas molecules

ΔL: a distance

L_0: characteristic entities for length

L_c: characteristic length

L_{filter}: lifetime of filter

μ: fluid dynamic viscosity

μ_E: ion mobility

μ_t: eddy viscosity

m: variable of loaded dust

m_p: particle mass

M: dust loading

ν: kinematic viscosity

N_0: ion concentration

$N_{background}$: number of background particles

N_{outlet}: number of particles at outlet

p: fluid pressure

Δp: pressure drop

p_0: characteristic entities for pressure

P: circumference of airflow channel

ΔP_{ave}: average pressure drop across the filter

ΔP_{eff}: effective system pressure drop

Pe_E: electric Peclet number

q: charge density

q_0: characteristic entities for charge density

q_c: characteristic particle charge

q_d: diffusion charging as a function of time

q_f: field charging as a function of time t

q_p: total particle charge

Q: volumetric airflow rate

ρ: fluid density

ρ_p: particle density

r: radial distance from the curvature center of corona wire

r_p: particle radius

Re: Reynold's number

Re_E: electric Reynold's number

R_i: radius of ionization region

R_w: wire radius

Stk: Stoke number

St_E: electric Stoke number

θ: constant

Δt: time interval

T: operation time per year

u_i: fluid velocity

$\overline{u_i'}$: fluid fluctuation velocity

U_0: characteristic entities for velocity

U_c: characteristic fluid velocity

U_τ: friction velocity

$\mathbf{U}$: velocity field of fluid

$\mathbf{U_p}$: velocity field of particle

v: free airflow velocity

v_{rms}: root-mean-square thermal velocity of ions

V: electric potential

V_0: characteristic entities for electric potential

V_i: electric potential at ionization boundary

V_w: electric potential at corona wire surface

w: particle migration velocity

W: system power consumption

VITA

Tsrong-Yi Wen joined the Department of Mechanical Engineering at the University of Washington Seattle in 2010. His research interests are the fundamentals and the applications of electrohydrodynamics, including high-efficiency electrostatic precipitators and electrostatic fluid accelerators. Prior to joining the University of Washington, he worked in the IC design industry from 2006 to 2010. His industrial expertise includes thermomechanical analysis of electronic packaging, thermal management of portable consumer electronics, and semiconductor manufacturing. He received his master of science degree in applied mechanics from the National Taiwan University in 2005 and bachelor of science degree in mechanical engineering from the National Cheng-Kung University in 2003.

He welcomes your comments to `tywen@u.washington.edu`